

The Development of Lightweight Cementitious Cellular Composites(LCCCs)

Zixia Wu

The development of Lightweight Cementitious Cellular Composites (LCCCs)

By

Zixia Wu

in partial fulfilment of the requirements for the degree of Master of Science in Civil Engineering-
Building Engineering at the Delft University of Technology

to be defended publicly on Thursday, May 6th, 2021, at 11:30

Student number:4848578

Email:andreawulove@gmail.com

Thesis committee:

Dr. B. (Branko) Šavija	TU Delft, Materials, Mechanics, Management & Design (3Md) Faculty of Civil Engineering and Geosciences
Prof.dr.ir. E. (Erik) Schlangen	TU Delft, Materials, Mechanics, Management & Design (3Md) Faculty of Civil Engineering and Geosciences
Dr.ir. H.R. (Roel) Schipper	TU Delft, Materials, Mechanics, Management & Design (3Md) Faculty of Civil Engineering and Geosciences
Msc. Y. (Yading) Xu	TU Delft, Materials, Mechanics, Management & Design (3Md) Faculty of Civil Engineering and Geosciences

An electronic version of this thesis is available at <http://repository.tudelft.nl/>.



Preface

About a year ago, I knocked on Yading 's office door with the curiosity and longing for 3D concrete printing technology and asked him some fascinating topics in this field. He shared with me the auxetic cellular cementitious composites that he has designed which is manufactured with the aid of 3D printing technology and discussed with me his ideas. Since then, I got warm welcomed to the cementitious material design field by Yading , Dr. Šavija, Dr.Schipper and Prof. Schlangen.

As the ending mark of my student career at the Delft University of Technology, master thesis is part of the requirement to obtain the Master of Science Degree in civil engineering. First, I would like to express my deepest gratitude to all my committee members for steering me through the research, every criticism and suggestion provided in meetings and emails motivates me to step forward to be better. I would like to thank Prof. Schlangen who offered me such a valuable opportunity for working in the materials and environment section, provided helps and professional suggestions no matter when I got stuck in the research. My heartfelt thankfulness to Dr. Šavija. Thank you for always inspiring me with new ideas and praising me when I have made progress in the work. I have learned a lot from you not only academic knowledge, but also the way of thinking and the passions toward the work. I would also like to thank Dr.Schipper for the constructive feedback in the research and warmhearted help in my study progress. A big thank you for Yading, for the patience in answering all my questions and responsibility of constant reviewing my progress, reminding me the details during the experiments , and encouraging me when I feel disappointed for my progress.

As a building engineering student, from beginning , I was not familiar with the experimental test procedure in the lab and very grateful for the help from Maiko. Also, I would like to thank Zhi, Yidong ,Shan and other colleagues for inspiring me and gave supportive suggestions during the daily conversations.

At last, I would like to thank my family and friends who gave me such unselfish support and uncountable love especially during this Covid-19 pandemic period, which motivated me to conquer challenges and keep positive in my life.

Zixia

Delft, April 2021

Abstract

In order to alleviate the burden of energy consumption, thermal insulation materials are widely adopted in residential and commercial buildings aiming at optimizing the energy efficiency of the heating and cooling systems, so that the excessive electricity consumption for maintaining comfortable indoor temperature can be saved and the corresponding carbon emission reduced. However, traditional thermal insulation materials are suffering from different adverse effect such as low mechanical strength, the risk of generating toxicity and high cost of producing and manufacturing. Therefore, the possibility of construction materials with good thermal insulation properties is an imperative driving force for researchers to develop novel materials possessing low thermal conductivity while maintaining reasonable mechanical strength.

This research focuses on developing architected lightweight cementitious cellular composites (LCCCs) for potential thermal insulation purposes. Specifically, Voronoi cellular structures with different randomness are adopted and used as cellular structure of the LCCCs. The mechanical properties of the developed LCCCs are investigated by experimental and numerical methods. With the help of 3D printing technique, LCCCs are prepared with two mixtures: a reference mortar, denoted as REF and mortar incorporating microencapsulated phase change materials (mPCMs), denoted as PCM14.

Mechanical properties of developed structures are first investigated. The compressive behaviour of the LCCCs is investigated at the age of 28 days. In general, the LCCCs show anisotropic compressive behaviour in two loading directions: the compressive strength and stiffness of the LCCCs in the out-of-plane direction is substantially higher than that of the in-plane direction. Comparing to conventional foam concrete with the same density, the out-of-plane compressive strength of the LCCCs is higher than commonly reported cases in literature. Due to the high porosity of the cellular structures, the compressive strength of the LCCCs is significantly reduced comparing to the corresponding constituent materials, as expected. In addition, this strength reduction of the LCCCs made with PCM14 is substantially lower than the that of the REF samples. Interestingly, the relative stiffness (measured stiffness of the LCCCs normalized by their porosity) of the mPCMs incorporated LCCCs is even higher than the constituent material E-modulus. Furthermore, the critical role of air voids on the compressive behaviour of the LCCCs is identified.

The thermal conductivity of the LCCCs is investigated by numerical models using commercial software Abaqus and ANSYS. It is found that the thermal conductivity of the LCCCs is comparable with the conventional foam concrete of the same density. The geometry heterogeneity of the LCCCs has a minor effect on determining the thermal conductivity of the LCCCs. Moreover, increasing porosity or reducing thermal bridge on the heat transfer direction can dramatically improve the thermal insulation performance of the LCCCs. It is found that the natural convection of the air within the cellular pores and the radiation has less notable effect on the thermal conductivity of specimen. Comparing to the REF, PCM14 has enhanced thermal insulation performance.

In the end, using extrusion-based 3D concrete printing technique, the LCCCs with mPCMs has been successfully printed as an implement of manufacturing LCCCs as a construction-scale brick.

In general, the developed LCCs have high porosity gives good insulation properties as well as good compressive strength. This gives them great potential to be used as novel lightweight thermal insulation materials for construction.

Key words: cementitious materials; architected cellular materials; phase change materials; 3D printing

Content

Preface	II
Abstract	III
1 Introduction	1
1.1 Introduction and Background	2
1.2 Research scope and objectives	7
1.3 Thesis organization and outline	8
2 Literature review	10
2.1 Classification and engineering applications of architected honeycomb cellular materials	11
2.2 Developing architected cellular cementitious material using three-dimensional printing technology (3DPT).....	14
2.3 Use of phase change materials (PCMs) for improving thermal performance in cementitious materials	20
2.3.1 The material properties of PCMs	21
2.3.2 Incorporating approach of PCMs into cementitious materials	21
2.3.3 Fresh, mechanical, and thermal properties of mPCMs incorporated cementitious materials	22
2.4 Summary	24
3 Fabrication of Lightweight cementitious cellular composites (LCCCs).....	25
3.1 Geometry description	26
3.2 Mix design for preparing the reference and PCMs incorporated cementitious mortar	27
3.3 Slump flow test	28
3.4 Specimen preparation.....	29
4 Experimental tests.....	32
4.1 Uniaxial compression test	33
4.2 Thermal properties test using transient plane source (TPS) method	35
5 Numerical simulations.....	38
5.1 Concrete Damage Plasticity (CDP) Model.....	39

5.2 Model calibration	39
5.3 Simulation of the cellular specimens.....	42
5.4 Steady-state heat analysis.....	45
5.5 Natural convection in the pore structure	47
6 Mechanical properties	51
6.1 Out-of-plane compressive behaviour	52
6.2 In-plane compressive behaviour.....	61
7 Thermal properties	66
7.1 Relationship between thermal conductivity and geometry randomness	67
7.2 Relationship between the thermal conductivity and porosity.....	71
7.3 The effect of convection and radiation on the thermal conductivity	75
7.4 The effect of mPCM on thermal conductivity.....	77
8 3D printing of LCCCs.....	79
8.1 Mix design.....	80
8.2 The general printer information, printing settings and printing procedure	80
8.3 The mixing and printing procedure	82
9 Conclusion and recommendations.....	84
9.1 The conclusion of compressive behaviour of LCCCs	85
9.2 The conclusion of thermal performance of LCCCs	85
9.3 The general conclusion of research.....	86
9.4 Discussion	86
9.4.1 The compressive properties	86
9.4.2 The thermal properties.....	87
9.4.3 Printing procedure.....	87
9.5 Recommendations.....	88
Bibliography.....	90
Appendix A.....	95
Appendix B.....	102
Appendix C	105
Appendix D.....	108

1

Introduction

This chapter provides an introduction of this thesis, clarifying the general motivation of research. After providing the background related to the research content, a summary of research scope and objectives is given. Finally, the organization as well as the outline of thesis are provided.

1.1 Introduction and Background

In recent decades, we have witnessed a dramatic increase of energy consumption over the world. Many studies show that, due to the explosive growth of population and the proliferating demand of housing, the proportion of building energy consumption in total global energy demands has been increasing, and this trend will continue for next couple of decades. The building energy demand mainly consists of heating and cooling which is necessary to satisfy the need of occupants' living comfort [1-3]. Even though great effort has been put on developing renewable energy sources such as solar energy and wind power, it is inevitable that the coal, natural gas, and petroleum products are primary sources of energy for heating, and electricity in both commercial and residential buildings. Therefore, heating and electricity generation in building account for a large proportion of global greenhouse gas (GHG) emission.

The European Union is a pioneer of developing low carbon emission solution. According to the target of Intended Nationally Determined Contribution (INDC) in view of the Paris Conference of Parties (COP21), which is submitted by European Union to the United Nations Framework Convention in 2015, the domestic greenhouse emission as well as domestic energy consumption should fulfil 20% reduction in comparison with 1990 in 2020, and 49% reduction in 2030 [2]. Based on the investigation of Nederlandse Organisatie voor Toegepast Natuurwetenschappelijk Onderzoek (TNO) (see Figure 1-1), service and households that make up the building environment, account for 35% of final energy consumption in the Netherlands in 2019, which is the biggest part compared with other sectors.[4] As an important member state, the Netherlands sets the goal of saving energy on average annually 1.5% from 2014 to 2020 [5]. Faced with this challenge, many member states of EU have adopted a series of measures including increasing the use of renewable energy sources, improving the energy efficiency of buildings by replacing the aging infrastructures and equipment and investing in insulation materials for building, improving thus the thermal integrity and reducing the energy losses.

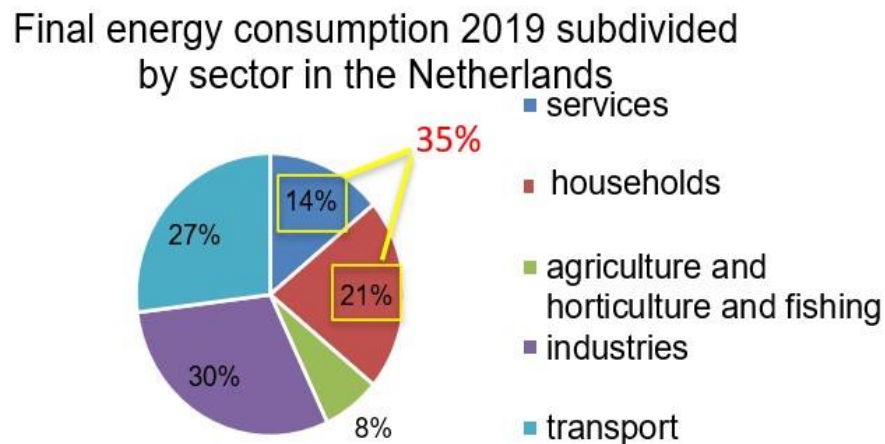


Figure 1-1 The final energy consumption 2019 subdivided by sector in the Netherlands, data adopted from TNO EnergieTransitie (2020)

Thermal insulation materials are applicable in residential and commercial buildings as means for reducing energy losses. Basim [2] identified several advantages of applying these materials in both low rise and high-rise buildings located in densely populated areas. Firstly, the thermal insulation materials facilitate the energy efficiency inside the buildings because they possess the high thermal resistance. By applying the thermal insulation materials, the heat/cold will be kept in the building and consequently less energy will be required for cooling in the summer and warming in the winter. Furthermore, the running cost of electricity consumption for maintaining the indoor temperature is efficiently decreased as a result of using of thermal insulation. On the other hand, the electricity consumption reduction is positively reflected on the reduction of environmental impact and the greenhouse gas emission.

A great number of polymer products have been developed as preferable insulation materials in many building applications, benefiting from their high thermal insulation performance, light weight and relatively low cost. The polymer products such as polyurethane (PUR) foam and expanded polystyrene (EPS) foam are formed by a series of chemical reactions during which pores filled with expanded gases are generated, leading to low density (15 to 45kg/m³) and low thermal conductivity (0.022 to 0.4 W/m.K). However, due to the poor mechanical properties of the polymer itself, reinforcement agent such as natural and synthetic fibres are often needed. Moreover, there are health concerns related to the use of these products because PUR and EPS are combustible and generate a large quantity of poisonous gases when on fire [6-9].

Another promising thermal insulation material is vacuum insulation panel (VIP), which consists of an open porous core and an air-heat tight envelope. It is shown in the Figure 1-2 that VIP is mainly composed of pressed silica core and multilayer envelope. The core is vacuumed, and the envelope should be kept scatheless for upholding the thermal insulation properties. The cost used for manufacturing and maintaining the VIP is considerably higher than that of other insulation materials. Besides the vacuum insulation panel, aerogel represents the state-of-art insulation material which consists of dried silica gel with high porosity and extremely low thermal conductivity (between 0.013-0.014 W/m. K). Taking advantage of the high transmittance of visible light of silica aerogels, the monolith translucent aerogel insulation panels which is broadly applied on the ceiling or curtain wall for the purpose of acquiring daylight in new buildings have been brought into the vogue (see Figure 1-3). Nevertheless, the substantial production and installation cost of aerogel panels is still a heavy burden for the building industry.

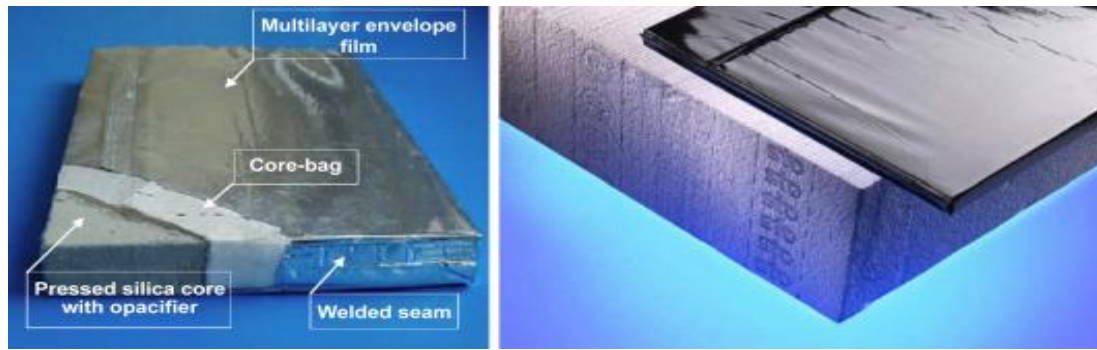


Figure 1-2 The demonstration of main structure consisting of vacuum insulation panel (left)[10] and the comparison of the thickness between VIP and traditional polymer panel(right) [11]



Figure 1-3 The utilization of monolith translucent aerogel insulation panels on the ceiling and facade as the high thermal insulation solution for the daylight purpose [11].

In order to mitigate the adverse effects mentioned above from which that current thermal insulation materials are suffering, namely low mechanical strength, the risk of generating toxicity and high cost of producing and manufacturing, exploring the possibility of construction materials with good thermal insulation properties is an imperative driving force for the researchers to design novel materials possessing low thermal conductivity and maintaining reasonable mechanical strength. As the most used construction materials, cementitious materials are investigated in many studies. Foam concrete is one of the commonly reported lightweight cementitious materials. With the pre-foam or mixed foam is blended into the mortar, high porosity is introduced to the foam concrete which usually has density ranging from 400 to 1800 kg/m³, low thermal conductivity (0.1-0.7 W/m.K), high flowability and self-compacting, making it considered as a good choice for manufacturing cavity filling, pre-cast panel and thermal and acoustic insulation material [12-14]. However, the using of foam agent also has an inevitable drawbacks such as producing large amount of damaged bubbles which compromises the amount of included air, leading to the quality decrease of foam concrete [12]. Although, the pre-form method can create foam by using the compressed air and adding the bubbles

into mortar to form cell structure, which guarantees the efficient foam generation and foam quality, it is more expensive compared with the mixing method.

Similarly, some researchers focus on adding lightweight ingredient which also introduce high porosity in concrete and modify the thermal properties. Ruiz-Herrero et.al [15] tried to decrease the thermal conductivity of concrete by including 5% of plastic waste aggregate, Panesar et.al [16] proved that adding wasted cork into the mortar can improve the thermal performance. These methods indeed help recycling the wastes in concrete as the replacement of sand or other fine aggregate therefore alleviating the burden of landfilling or other environmental impact (for instance burning the unbiodegradable wasted plastic), however the classification of suitable waste has not been standardized yet and how the potential involved harmful chemistry (especially for plastic waste) concerns human health is still unclear [17, 18].

Apart from the introduction of foaming agent to form the closed pores or integrate cellular aggregate into the mortar, engineers have a growing propensity on designing architected cellular cementitious material inspired by honeycombs, lattice structures, and other designs which can provide reasonable stiffness and strength accompanied by low mass and high porosity [19]. With the help of experimental and numerical analysis, many studies have attempted to integrate the Voronoi structure with metal and polymer materials to form cellular composites. By optimizing the pore size, porosity, cell wall thickness, and distribution of metal and polymer Voronoi shaped cellular composites, different extent of enhancement on energy absorption ability [20, 21], thermal performance [22, 23] and strength-to-weight ratio have been achieved [24]. While this concept has been widely explored in such materials, there has been very limited development of cementitious materials with Voronoi structures. Consequently, while their potential applications are promising, the knowledge of the physical and mechanical properties of cementitious materials with Voronoi structures is scarce.

Another opportunity of improving the energy efficiency of cementitious materials - the use of phase change materials (PCMs) as additives - has been widely explored in recent years. In such applications, the phase change process occurs due to the indoor/outdoor temperature variation, in which the heat is absorbed by melting or is released by solidifying during the liquid-solid transition of the PCMs, therefore provide thermal inertia against the temperature fluctuation and therefore increasing the energy storage and efficiency [25, 26]. In the last two decades, appreciable studies have strived for incorporating the PCMs into the cementitious materials to enhance the energy saving in building environment [27-30]. However, it has been reported that the addition of PCMs [31, 32] causes a decrease in compressive strength and workability of cementitious [33, 34].

3D printing technology is one of the major industry innovations [35]. Integrating with CAD software, the customized objects and shapes can be produced by a layer-wise stacking process. Initially, the technology was mainly applied for rapid prototyping in the artware field. Due to the high-fabricating speed, material waste reduction, the possibility of fulfilling customized and complex design, 3D printing technology has been involved in many industries such as aerospace, medical science and civil engineering. Currently, many companies and institutes have studied and emphasized on the development of large-scale 3D concrete printing (3DCP) system for producing single structural element or the direct housing automated prefabrication, for the sake of rapid construction and labour cost reduction [36, 37]. The Netherlands is a pioneer in developing the application of 3DCP construction, the printed structures of completed and ongoing projects ranging from houses, bridges,

pavilions, and shelters [38]. At the left top of Figure 1-4 displays the 3D printed reinforced concrete cyclist bridge constructed by BAM Infra in Gemert [39], and at the right part of the same figure demonstrates the world first commercial housing based on 3D concrete printing technology in Eindhoven [40], both designed by engineers from Technical University of Eindhoven. Meanwhile, the evolution of 3DCP applications is moving forward with the combination of using parametric design tool. The bridge project (at the left bottom of Figure 1-4) which will launch in Nijmegen involving the initiative of Rijkswaterstaat and the design idea of Studio Michiel van der Kley, aims at making an innovation of 3DCP construction automation process [41]. In addition to the large-scale construction field, the 3D printing technology can be used for enhancing some properties of cementitious material which are not sufficiently explored yet, namely to “develop cementitious composites that cannot be made by conventional methods” as described in [42].



Figure 1-4 The 3D printed reinforced concrete bridge in Gemert, North Brabant constructed in 201[39](left top). The 3D Printed concrete and parametric designed bridge will be placed in Nijmegen.[41] (left bottom).The world first commercial housing project based on 3D concrete printing in Eindhoven,2019 [40] (right).

The concept of combining architected cementitious cellular structure with PCMs might be promising for developing lightweight cementitious cellular composites (LCCCs) with excellent mechanical and thermal performance. However, the effect of geometry traits and PCMs on the mechanical as well as thermal behaviour of LCCCs has yet to be fully understood. In this study, the mechanical and thermal properties of LCCCs will be characterized with the help of experimental test and numerical simulation. The effect of cell irregularity and the density of specimen, the addition of PCMs in the mortar and other factors concerning the compressive strength and behaviour, thermal insulation performance of LCCCs will be discussed and using 3D concrete printing to manufacture LCCCs will be implemented and described in this thesis.

1.2 Research scope and objectives

The goal of this research is developing architected lightweight cementitious cellular composites (LCCCs) with good mechanical and thermal properties for potential thermal insulation purpose and investigate the effect of geometry and physical characteristics of the LCCCs, mixture design on the mechanical and thermal properties of the architected LCCCs. To this end, this research pursues the following objectives:

- Experimentally investigate the compressive behaviour of the LCCCs. Specifically, quantify E-modulus, compressive strength and fracture behaviour of the LCCCs. Meanwhile, experimentally obtain the mechanical and thermal constitutive parameters of the constituent materials (reference mortar and PCM incorporated mortar) as input parameters for numerical simulations.
- Utilize numerical models for analysing the compressive and thermal performances of the LCCCs and carry out comparative studies between experimental numerical simulation results to clarify most performance influencing factors.
- 3D printing of construction scale LCCC brick using extrusion-based 3D concrete printing technology as a demonstration of the concept of architected cementitious materials and as a closure of this research.

1.3 Thesis organization and outline

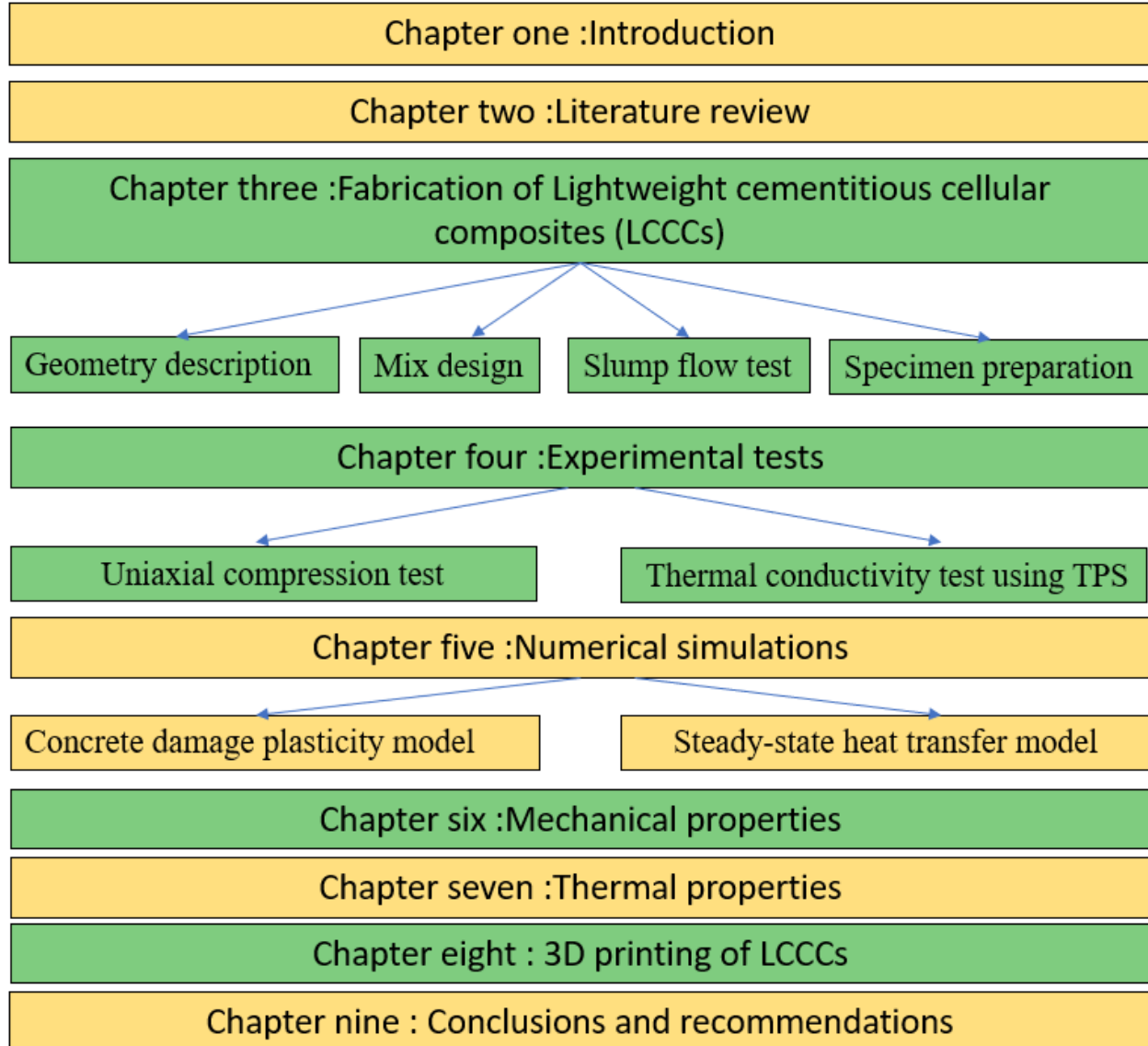


Figure 1-5 The thesis organization

This dissertation consists of nine chapters.

The *introduction* chapter describes the background of the increasing building energy consumption, the state-of-art of thermal insulation materials, points out their advantages and disadvantages, brings up the trend of using lightweight cementitious materials for thermal insulation purpose, highlights the great interest on study the combination of architected structure with PCMs so that lays the groundwork for developing a novel lightweight cementitious cellular composites and the application of 3DCP in the cementitious composites level, states the objectives of this research work and provides the outline of this thesis.

Chapter two provides a pertinent literature review *on the topic of this dissertation*.

Chapter three describes the preliminary preparation process for experiments. A detailed description of the sample geometry and mix design are provided. Slump tests of the designed mixtures as well as the sample preparation protocol are included. Among a total of five mixtures, two most suitable mixtures (REF and PCM14) are chosen to cast specimens considering the fluidity of mortar. Specimens with two different sizes are prepared for evaluating compressive strength and fracture behaviour respectively.

Chapter four focuses on describing theoretical background and experimental set-up. During the mechanical test, force and displacement of the specimens are recorded in uniaxial compression. The transient plane source (TPS) method was applied for measuring the thermal conductivity of the two chosen mixtures.

Chapter five is dedicated to introducing the numerical models of mechanical and thermal simulation. The principle and the governing equations of concrete damage plasticity model (CDPM) used as the mechanical simulation model in the Abaqus software, have been articulated in the first section, followed by the elaboration of simulation set-up. Steady state heat transfer analysis is emphasized as the second part, how the conductivity, convection and radiation are considered in the thermal simulation is described in this chapter. Moreover, the effect of natural air convection in the pores of LCCCs is briefly concluded.

Chapter six studies the compressive behaviour of the LCCCs according to experimental results accompanied by numerical simulations. The comparison between the experiment results and numerical models in terms of the elastic modules of LCCCs, the stress-strain response and the post-peak behaviour are discussed. The critical role of air voids defect on mechanical property of the LCCCs is clarified.

Chapter seven discusses the relationship between the geometry randomness, porosity of LCCCs specimen to the thermal conductivity based on both numerical and analytical analysis. Furthermore, the effect of convection, radiation on the thermal performance of the LCCCs is investigated by comparing the results from the situation in which only conduction is considered. In the end, the effect of incorporating PCM in the cement paste on the reduction of LCCCs specimens' thermal conductivity as well as the limitation of current thermal analysis on study the latent heat is elaborated.

Chapter eight, the attempt of 3D printing LCCCs specimen has been conducted by utilizing the concrete 3D printer. Printable PCM incorporated cementitious mortar is designed. Detailed information of mixing and printing process is introduced.

Finally, *Chapter nine* presents the conclusions of the dissertation. To the end, discussion of the potential use of the developed for LCCCs in the future is given.

2

Literature review

“When modern man builds large load-bearing structures, he uses dense solids: steel, concrete, glass. When Nature does the same, she generally uses cellular materials: wood, bone, coral. There must be good reasons for it.”

— M. F. Ashby, University of Cambridge

To be able to combine the two-dimensional cellular structure with cementitious material, initially, it is important to know the characteristics of cellular structures and how they are applied in the engineering field. Additionally, additive manufacturing offers an opportunity to architect the cellular structure while how it influences cementitious materials is crucial to be understood.

This chapter focuses on the review of honeycomb architected cellular material in engineering applications, introduces 3D printing related methods employed on the developing architected cementitious composites, provides the knowledge in terms of material properties of PCMs, the PCMS incorporation approaches and the effect of PCMs on the mechanical and thermal properties of PCMS incorporated cementitious material.

2.1 Classification and engineering applications of architected honeycomb cellular materials

Cellular structures ubiquitously exist in the nature. Many materials such as wood, bone and sponge are composed of substantial polygonal or polyhedral cells enveloped by solid edges or faces. Their cellular structures enable the good strength and stiffness at a low density, which have inspired humankind on developing synthetic material or composites with improved structural properties, reduced weight, excellent acoustic and thermal insulation performance, high energy absorption ability and other functional properties (shown in Figure 2-1) in broad fields such as aerospace, building and biomedical applications [43].

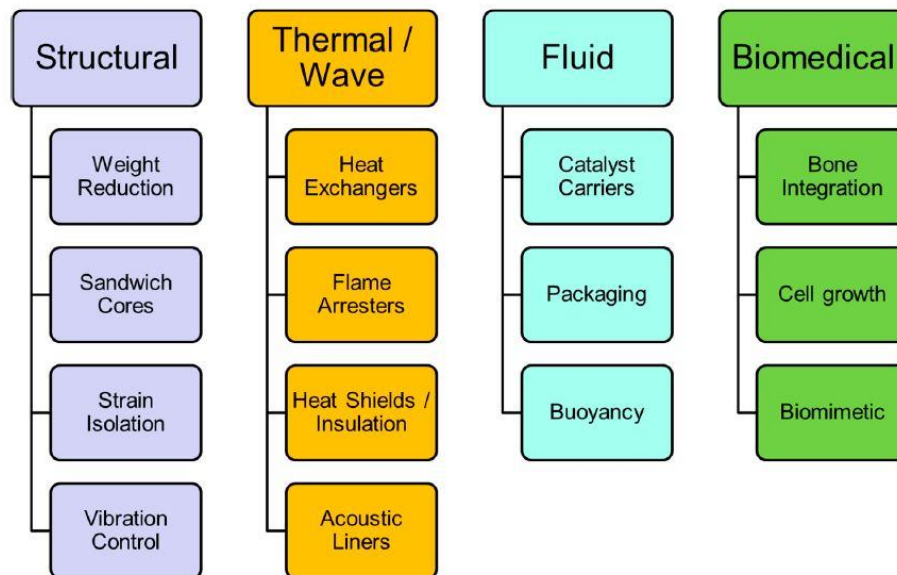


Figure 2-1 The application examples of cellular structures in which their specific properties enhance the targeted functions, adapted from [44].

One of the most well-known studies in terms of the classification and mechanical properties of cellular structure was provided by Gibson & Ashby in 1997 [45], in which they classified the cellular structure into two categories: honeycomb and foam. The name of honeycomb originates from the hexagonal cells' construction of a honeybee nest, see Figure 2-2 (left). The honeycomb is defined as the 2D prismatic cellular structure extruded out on the third direction, the thin plates or sheets compose the unit cell wall. On the other hand, the foam consists of three-dimensional arrays of cells generated by the foaming process (traditionally by the means of manipulating chemistry or microstructure of base material) and the forms of the cells are stochastic, which possesses higher complexity on the geometrical shape and spatial configurations compared with honeycomb, see Figure 2-2 (right) [46]. Considering that the study goals of this work is to investigate the effects of manipulating the architecture of the cellular structure and the influence on the properties of cementitious materials, therefore the emphasis has been put on the classification and relative application of honeycomb structure, the discussion of spatial-complex foam structure is out-of-the research scope. What is different from people's common perspective is that the topology of engineering honeycombs unit cell

is not always hexagonal, but can also be in the form of square, circular, triangular or irregular patterns [47]. Based on the classification proposed by Bhate et al [46], the topology of honeycomb structure can be subdivided in two categories: periodic honeycomb (the shape of unit cell is prescribed and repeated to filling the space, such as the examples in Figure 2-3 (A)-(E)) and stochastic honeycomb (the shape of unit cell is generated by a stochastic mathematical function, for example Voronoi honeycomb).

Periodic honeycombs are commonly applied as the lightweight cores of lightweight sandwich panel made of polymer or metal. Gu et al [48] studied the effect of cell morphologies and arrangement including the regular hexagonal, square cell and triangular cell on the heat dissipation and mechanical properties on the cellular metal core sandwich panel. It is reported in that honeycomb possessing square or hexagonal cells performs better on forced convection heat transfer than that of triangular cell, whilst the triangular cell provides higher in-plane strength and stress under the various load conditions.

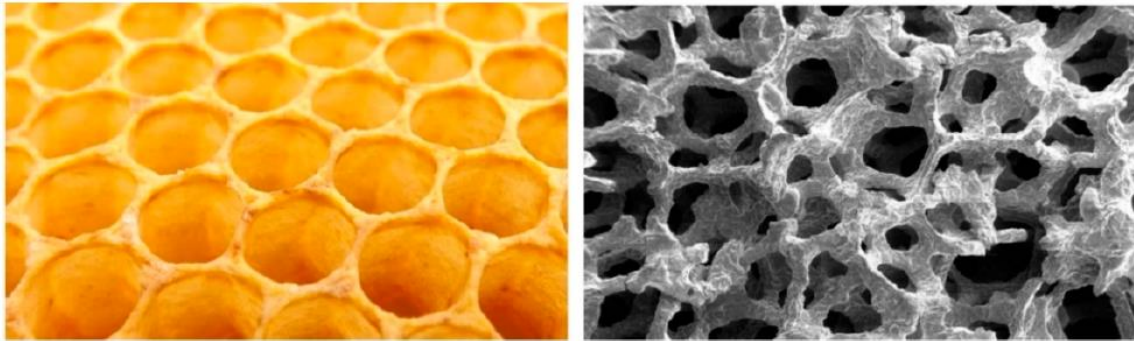


Figure 2-2 The honeybee's nest as the examples of prismatic periodic cellular structure(left). The 3D stochastic metal foam(right) [46].

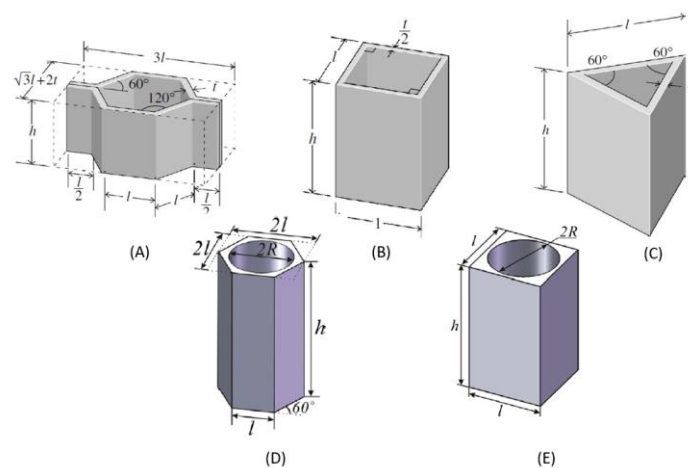


Figure 2-3 The periodic honeycombs: (A) Hexagonal honeycomb (B) Square honeycomb (C) triangular honeycomb (D) circular cored hexagonal honeycomb (E) circular cored square honeycomb [49]

Different with the periodic honeycomb which relies on the pre-supposition of regular cell shape with repeated unit cells in the two-dimensional plane, the stochastic honeycomb results from the random nucleation growth. One of the representative stochastic honeycomb is Voronoi honeycomb. Voronoi diagram is a mathematical approach for tessellating the n-dimensional cases coined by Ukrainian mathematician Georgy Voronoi. Gibson & Ashby [45] pointed out that Voronoi honeycomb formed by drawing perpendicular bisectors between the random nucleation points forming the envelope of cell surfaces that surround each points, each cell contains all points that are closer to its nucleation point than any others, and the construction of non-periodic cellular structure leads to other results. In addition to the cell shape and size, relative density (the ratio between the density of cellular material and the density of the material of which the cellular structures are made), the cell wall thickness that characterize the cellular material, the change of irregularity is necessary to be considered especially on characterizing the Voronoi cellular and other non-periodic cellular structures. Meanwhile, the modification of cellular irregularity might be a potential opportunity for optimizing the target application of tailored materials/composites.

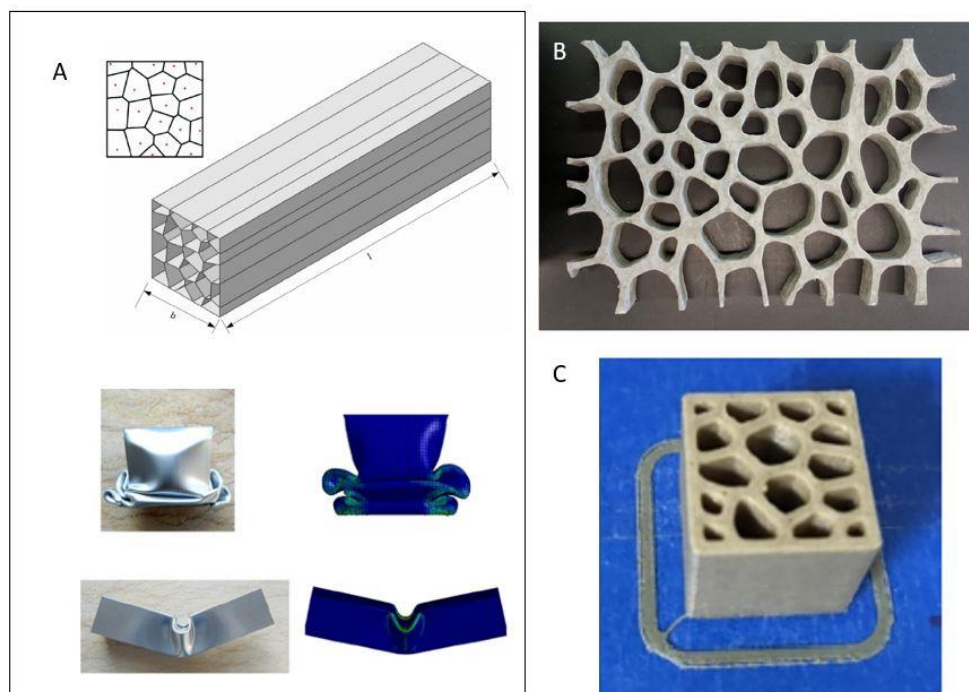


Figure 2-4 (A) The multi-cell thin square wall tube with Voronoi cross-section (top) experimental results demonstration of deformation pattern for axial crushing (bottom left) and for lateral bending (bottom right). [50] (B) The Voronoi-like tessellation formwork produced by strain hardening cementitious material. [51] (C) The 3D printed Voronoi-like cellular composites made by wood plastic [52].

Abdullahi et al [49] proposed a multi-cell Voronoi tubes (MVTs) used as front side rails in automobiles for enhancing the crashworthiness and energy absorption. It is shown in Figure 2-4 (A) that generation of multi-cell Voronoi tube geometry and it is the prototype for manufacturing the tested specimen made of aluminium alloy. The specimen was subjected to axial crushing and lateral bending load on the purpose of investigating the energy absorption capability of the MVTs.

Subsequently, the numerical model was developed and validated by the experimental results. Abdullahi et al. concluded that when subjected to the axial crushing, MVTs exhibits a better performance on crashworthiness than regular multi-cell tube because the MVTs have more corners facing the load direction, leading to the earlier deformation occurrence and the reduction of initial crush force. In terms of under the bending load, MVTs exhibits better on reducing the initial crush force whilst the regular multi-cell tube has higher energy absorption capability with the same mass. Furthermore, researchers in Ghent University exploited the possibility of combine the Voronoi-like tessellation formwork with strain hardening cementitious material to producing the self-healing strain hardening cementitious composites [50] (depicted in Figure 2-4 (B)). Tao et al [51] developed Voronoi-like cellular composites utilizing the fused deposition modelling printing technology and wood plastic composites as the base material, aiming at creating strong and sustainable cellular composite (see Figure 2-4 (C)).

2.2 Developing architected cellular cementitious material using three-dimensional printing technology (3DPT)

The development of concrete construction is oriented toward progressive automated process for achieving the construction efficiency enhancement and refining the manufacture precision, three-dimensional printing technology (3DPT) as one of the additive manufactures (AM) technology has received increasing attention, many large scale engineering structures have been completed via layer-by-layer on site three-dimensional concrete printing (3DCP) system [52]. However, compared with real-sized 3DCP project which emphasize on minimizing the cost of labour input as well as ensuring structural integrity and safety, using 3DPT on cementitious material to improve material properties, namely good strength and ductility with low density and high porosity and exploit the potential applications such as energy absorption, vibration damping by varying the architecture features which is not attainable by traditional casting method. Literature reveals that there are two approaches which have been proposed for developing architected cellular cementitious material: direct extrusion-based 3DCP method and indirect printing method [53].

Wang et al [54] utilized the extrusion based 3DCP printer (see Figure 2-5) and optimized cement mixture to make cubic and prismatic beam specimen with cellular, truss, triangular and lattice-shaped interior hollow sections. To investigate the mechanical behaviours of these concrete structure so that the shape efficient of four hollow section configurations on mechanical resistant capabilities could be compared, they conducted compressive test for measuring the compressive strength of cubic specimen ($150\text{mm} \times 150\text{mm} \times 150\text{mm}$) and four point bending to obtain the flexural strength of prismatic beam specimen ($400\text{mm} \times 100\text{mm} \times 100\text{mm}$). In the research, they designed five concrete mixtures containing different replacement ratio of ceramsite sand to silica sand, carried out the slump test for measuring the flowability of desired mixture. The tested sample were prepared and cured for 28 days until operating mechanical tests. Firstly, by observing the crack patterns, the weak interlayer which may influence the overall mechanical resistance of specimen as well as the crack propagation path could be observed (as shown in Figure 2-6(1) (2)). Secondly, to further elaborate the deformation resistance capacity of diverse hollow sections, the strain gauge was attached on the specimen for recording the displacement of tested sample subjected to the compressive or bending load, and the corresponding strain-stress curve was derived from the recorded displacement and

force. According to the experimental results, the interior hollow section structures exhibit promising advantage on optimizing the material usage, namely using 48% to 53% of material reaching 56.5% to 90% of strength, compared with solid ones. Lattice shaped configuration specimen has the highest compressive strength and truss shaped configuration specimen performs best on flexural bending properties. Besides the experimental research, Wang and his colleague employed the discrete element method which is different with finite element method to analyse the stress distribution and failure mechanism of tested sample. (see Figure 2-6 (3) (4)). The former method is particle-based approach and predicts the deformation and failure process of samples by the calculating the contact force between the adjacent contacted balls, which is proven as an efficient simulation method to evaluate the mechanical behaviour of hollow section.



Figure 2-5 The demonstration of extrusion-based printer for cementitious material (left) and the example of lattice-shaped hollow section specimen under the printing process(right) [54]

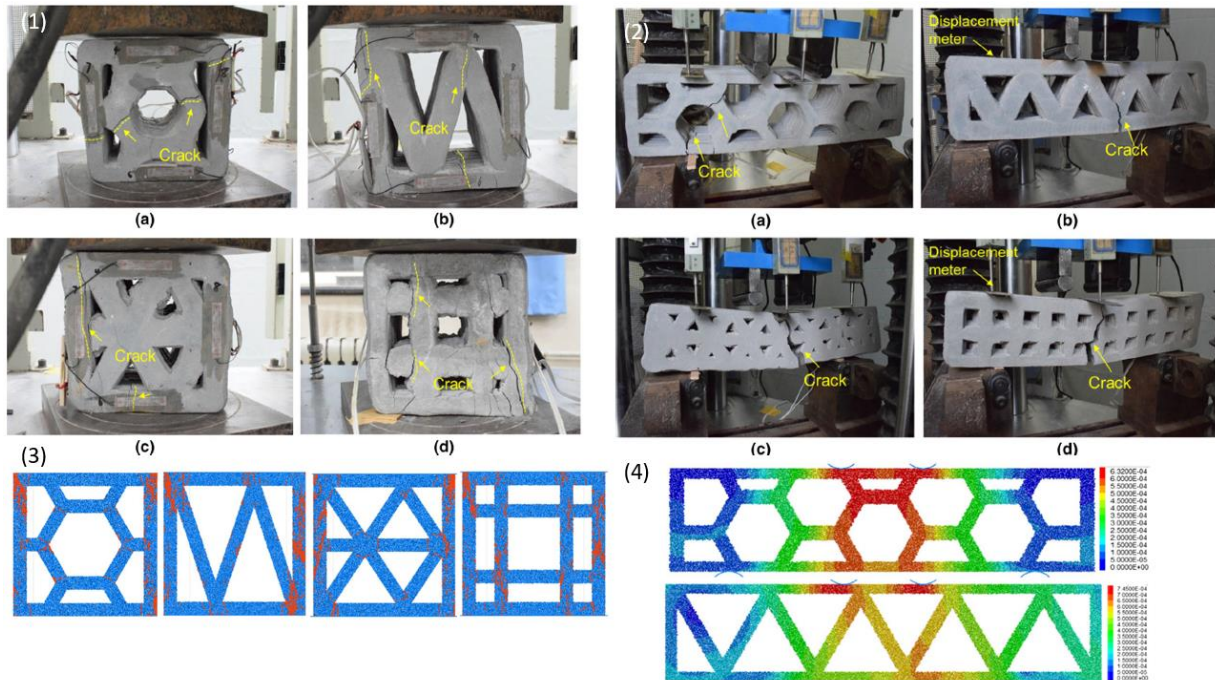


Figure 2-6 (1) The failure pattern of cubic specimen under compressive test (2) the crack pattern of prismatic specimen under four-point bending test: (a) cellular (b) triangular meshed (c) truss meshed (d) lattice-shaped (3) The crack pattern under 70% of peak load simulated by DEM (4) The example of numerical force chain distribution of cellular and triangular meshed specimen subjected to four-point bending [54]

Another extrusion-based 3DCP technology has been used in research is called direct-ink writing (DIW) preferred for micro-scale printing which offers high degree of control and possibility of fabricating the intricate architectures where high printing resolution can be achieved. However, the challenge of DIW and other similar extrusion-based technology facing with is intractable: due to nonuniformity of the cement paste, the particles might be jammed in the syringe or clogged in the nozzle; additionally, the air bubble are easy to be entrapped in the cement pastes during the mixing process. The mentioned two reasons might lead to the clogging and discontinuity of the extruded filament respectively (shown in Figure 2-7 (b) (c)). Besides, the ideal printed cement pastes ought to possess enough plastic viscosity and yield stress for developing the interlayer bonding and sustaining the printed filamentary shape. Sajadi et al [55] shed the light on studying the effect of nano-clay which is considered as a rheology modifier and reinforcement additive on balancing the flowability and shape stability of printed filaments. The ingredients and the mixing process of modified cement slurry are depicted graphically in Figure 2-8 (d). The researchers also emphasized on developing the complex architected cellular structures by applying the modified cement-based ink via DIW technology for exploiting the possibility of improving the toughness of brittle cementitious material. They printed hexagonal honeycombs, triangular-shaped honeycombs, and star-shaped honeycombs with the size of 11cm length, 6cm width and 1.6cm height. The uniaxial compressive tests have been carried out on three honeycomb structures to elaborate the mechanical behaviour of specimen as well as the diverse response of them due to the different configuration. The test process has been recorded and shown in Figure 2-8 (a). The force-displacement of in-plane loaded specimen displayed the ductile mechanical behaviour. It is clearly observed in Figure 2-8 (b) that the progressive load drops

occurred after the initial linear elastic stage has reached. On the other hands, the FEM analysed the localized stress distributions on different structures and unravels the localized stress tend to concentrate along the sharp edges(it is shown in Figure 2-8 (c) structure I which consists of sharp edges has higher localized stress).Based on the analysis from Sajadi et al, it is known that this incremental fracture mechanism can be attributed to the cell compartmentalization resulting in the cracks took place in different solid edges of cells, postponing the catastrophic failure of entire structure.

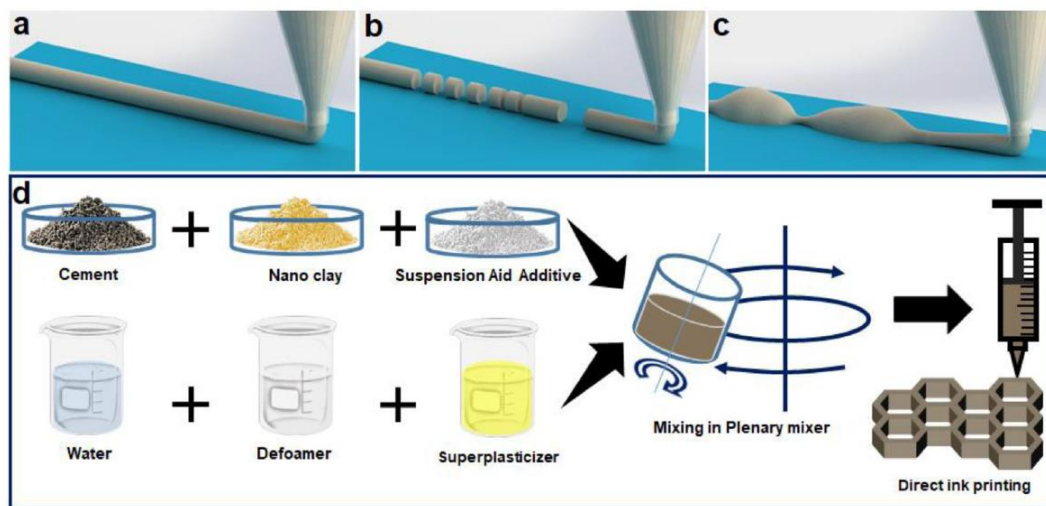


Figure 2-7 (a) The ideal smooth printing (b) discontinuity of extruded filament (c) clogging of extrusion (d) The modified solid constituent including nano clay and suspension aid additives which were mixed with cement separately, the defoamer and superplasticizer are added to water. The modified cement paste is formulated by uniformly mixing the liquid and solid constituent in the plenary mixer. The figures are adopted from [55]

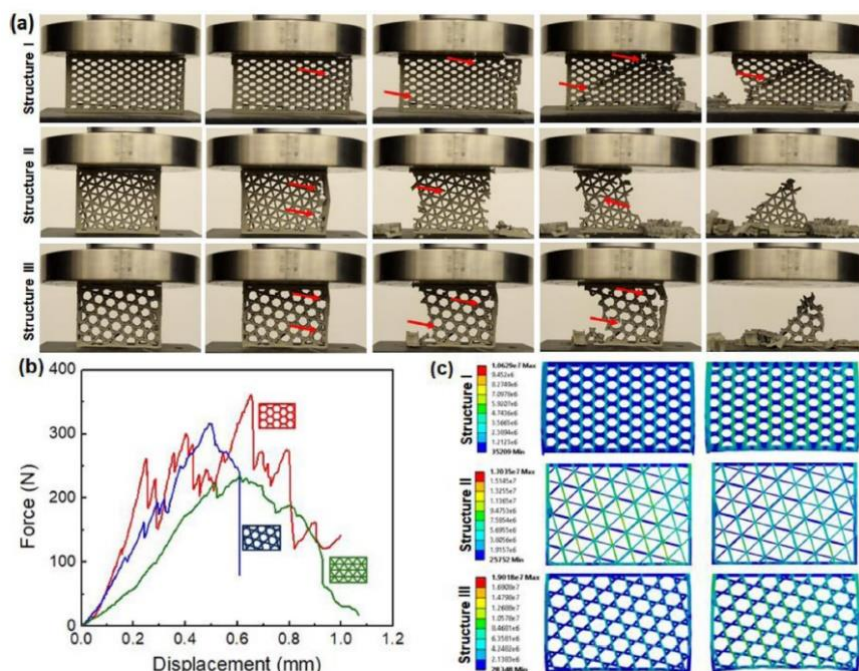


Figure 2-8 (a) A series of snapshots recording and demonstrating the mechanical failure of three different honeycombs structures under the uniaxial compressive tests. The initial crack occurs at each moment is indicated by the red arrow which shows the crack propagation (b) The representative force-displacement relationship of three honeycombs structures (c) The von Mises stress distribution in different strain range of various honeycomb structures via FEM simulation [55]

Although using three-dimensional concrete printing technology is a popular topic, drawbacks exist making it an imperfect alternative of traditional casting method. It is not hard to conclude from the previous two mentioned examples that to guarantee the printability of cement paste, the constituent raw material and the water-to-cement ratio must be chosen properly; Secondly, the possible material collapse during the printing process resulting from the low yield stress of material itself and loss of stability due to the deviation of centred self-weight of structure are high-risk threat for the printing failure. To overcome these adverse effects, some researchers use 3D printed plastic moulds and combine traditional casting technology for developing architected cellular cementitious material. Xu [56] et al proposed an “indirect” 3D printing working flow demonstrated in Figure 2-9 and briefly described as: at first, using the acrylonitrile butadiene styrene (ABS) as the printing material to 3D printing the plastic mould of designed shape; afterwards, pouring the silicone rubber into the plastic mould and put it into the vacuum chamber to extract trapped air in the rubber, after hardening and detaching hardened silicone rubber mould, casting mortar into the silicone rubber mould for manufacturing the cementitious cellular specimen. In the research, the chiral and ellipse shaped cellular structure were used for investigating auxetic behaviour of cementitious material. The auxetic behaviour resulted from the combination of geometry tunability and the modified material properties. Since normal cementitious material is brittle and sensitive to the tensile stress, if the ellipse shaped cementitious cellular structure is loaded under the compression, the crack occurs and propagates through the joint, leading to entire fracture of the structure. Xu added reinforced fibres into the cement mixture for enhancing the deformability of the cementitious material. Once the compressive load was applied on the unit cell, the crack bridge at joints developed. As a result, the lateral contraction of materials was attributed to the rotation of unit cell section (see Figure 2-10), similar with the material possessed the negative Poisson’s ratio which is so called auxetic behaviour. Benefiting from this behaviour, these novel cellular cementitious composites have exhibited energy absorption ability and can be considered as a promising vibration damping alternatives in engineering application. Nguyen-Van et al [57] proposed a novel approach of manufacturing architected cellular cementitious composites by means of 3D printing primitive triple periodic minimal surface (TPMS) structure combined with cubic block, lattice and gyroid-TPM thermoplastic Polylactic Acid (PLA) mould and cast the cement paste into the mould. With the help of experimental test and FEA tools, the mechanical performance of three structures was evaluated and identified the primitive-TPMS cementitious block as a promising coastal protection and lightweight block.

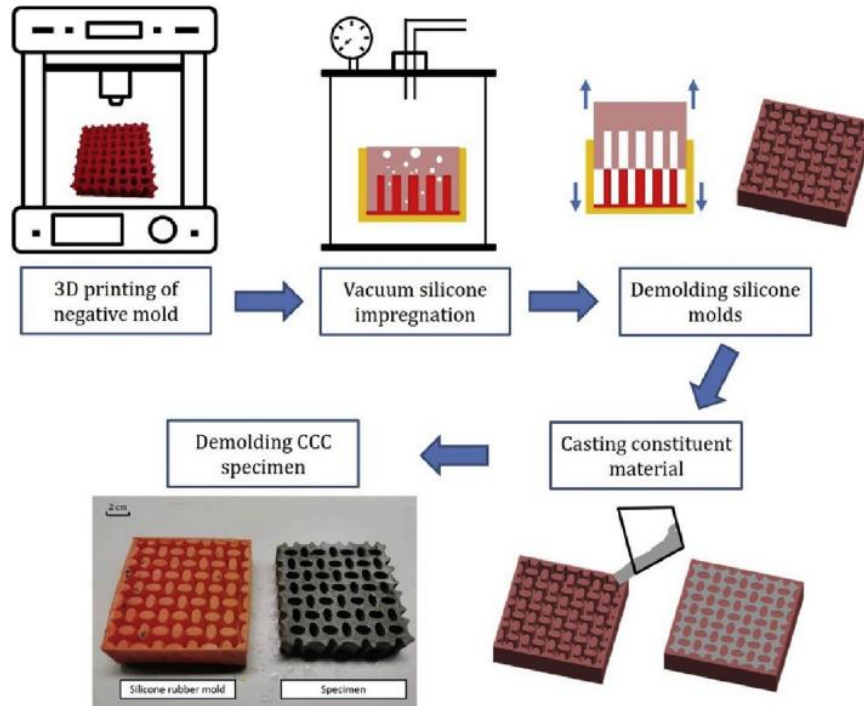


Figure 2-9 The "indirect" 3D printing working flow adopted from [56]

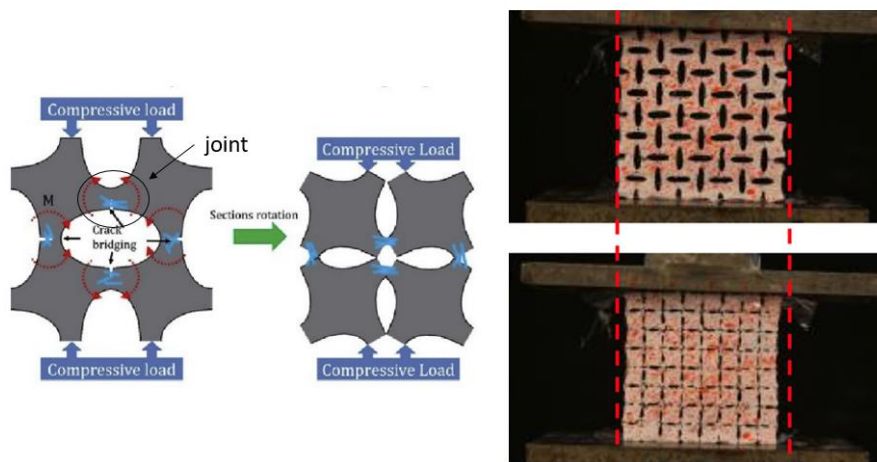


Figure 2-10 Left: the behaviour of crack bridging and the rotation of joint. Right: the auxetic phenomenon of cellular cementitious composites under compressive loading [42, 56]

2.3 Use of phase change materials (PCMs) for improving thermal performance in cementitious materials

Phase change material (PCM) is defined as substance that possesses high latent heat storage (LHS) capacity and energy is absorbed or released in the form of heat during the phase transition process, consequently regulating the ambient temperature [58]. In actual application, the large thermal mass of concrete wall benefit the thermal storage, the integration of PCMs improves the effect of energy saving. For instance, it is shown in Figure 2-11 that during the daytime PCMs absorb the heat by solid-to-liquid phase change while when the temperature is lower at night, dropping below the phase transition temperature of PCMs, the stored heat is released again by solidifying, therefore the heating and cooling cycles help to stabilize the indoor temperatures in a comfort range [27]. There are various types of PCMs in the market. Their physical characteristics, how they are combined with cementitious material and how they affect the properties of incorporated products should be well understood for their successful application.

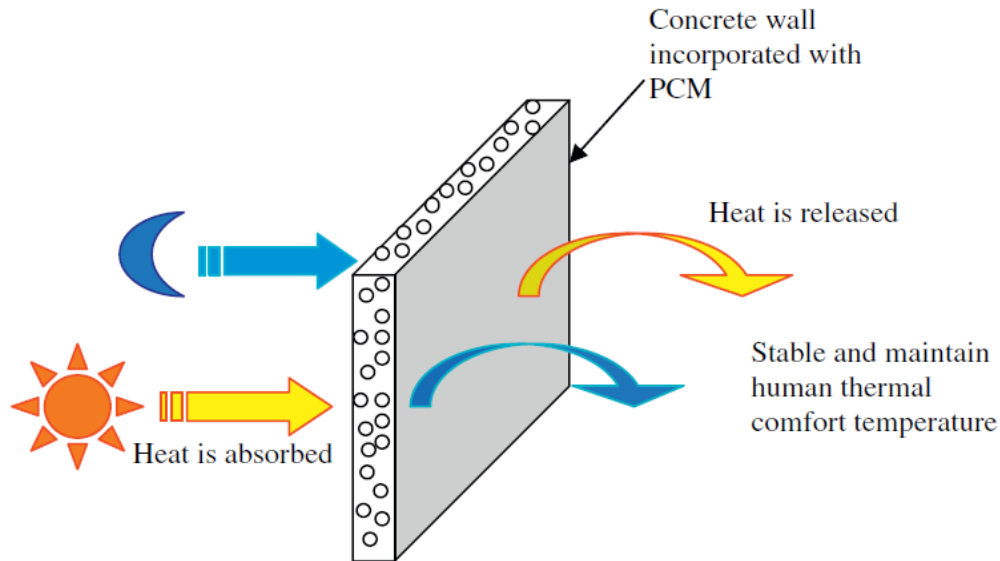


Figure 2-11 The schematic demonstration of heating and cooling process of concrete wall incorporated with PCMs, adapted from [27]

2.3.1 The material properties of PCMs

PCMs can be classified in two categories, depending on their chemistry: inorganic or organic.

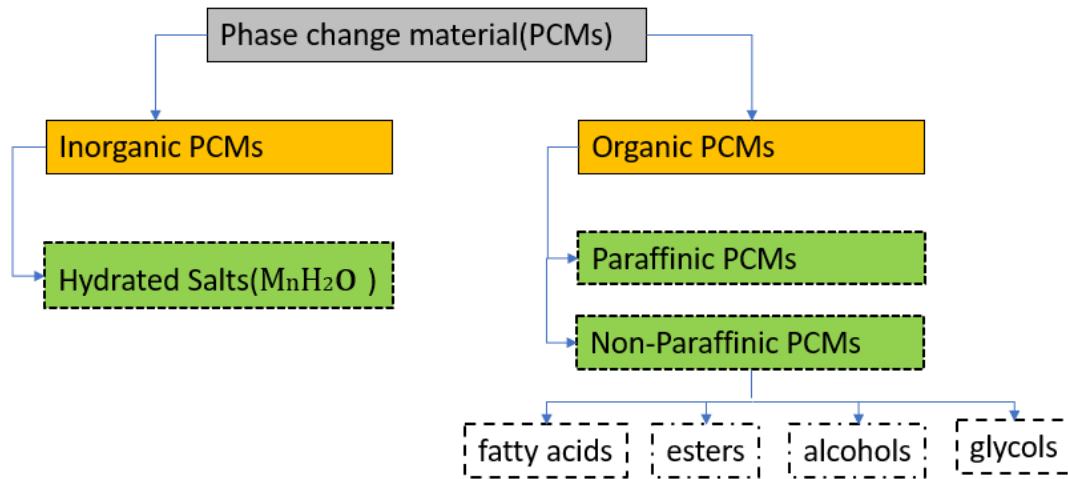


Figure 2-12 The general classification of PCMs ,information taken from [28, 30]

Hydrated salts (the main compound is M_nH_2O) is the most common used inorganic PCMs which possesses high energy density, good thermal conductivity, and is not flammable. However, the supercooling behaviour in the phase change process makes it an undesirable choice for incorporating in cementitious materials. Supercooling means that the temperature at which the liquid material starts solidifying is significantly lower than its melting temperature. Supercooling limits the application of hydrated salts in a specific narrow temperature range [59].

Paraffin wax is an organic PCM which is considered preferable for addition to cementitious materials. Due to advantages such as chemical stability, eco-friendliness, low cost, no phase degradation and inactivity in alkaline media which is compatible as an additive in the cement mixture, the paraffin wax is the most widely used PCM in cementitious materials. The thermal storage density of paraffin wax ranges from 120-210 kg/kJ and the phase change temperature has a wide range from 20 °C to 70 °C. Compared with inorganic phase change materials, the paraffin wax possesses a relatively low thermal conductivity which is around 0.2 W/m·K, making it a good mixture additive for the thermal insulation property. Additionally, it also exhibits relative volume change during the phase transition process which needs an appropriate incorporation method to overcome during the production of PCMs incorporated cementitious material [30].

Non-paraffinic PCMs including fatty acids, esters, alcohols, and glycols are suitable for heating applications and do not show supercooling effects. The high cost of non-paraffinic PCMs (three times higher than paraffinic) has impeded its widely application.

2.3.2 Incorporating approach of PCMs into cementitious materials

There are several studies focusing on the method of incorporating PCMs with cementitious materials and they are summarized as follows: (1) the immersion technology in which porous concrete is

soaked into liquid PCMs. The absorption rate of PCMs is attributed to the duration and the temperature of immersion, the type of PCMs, the porosity of concrete. On the other hand, in practical application an additional protection approach need to be employed in case of PCMs leaking from the voids in porous concrete [28]. (2) the lightweight aggregate impregnation method: porous aggregate is put in the vacuum chamber to evacuate air in the voids for 30 minutes. After that, the liquid PCMs is added into the chamber and flow around the porous aggregate. Finally, air evacuation stops, and fresh air can enter the chamber for driving the PCMs penetrating the aggregate. The impregnated porous aggregates work as carriers of PCMs [60, 61]. Regardless of the difference in technique, adopting immersion or impregnation technique, preventing the PCMs leakage during the solid-liquid phase change process is a problem and it gives a good reason for developing (3) microencapsulated PCMs (mPCMs). It is shown in the Figure 2-13 the tiny particles or droplets of PCMs are coated by the thin spherical shell, compositing the mPCMs. The shell is commonly made from polymer, providing a chemically stable barrier between the core material and other constituent materials, meanwhile preventing the PCMs from leakage. As known, the paraffin wax is widely used as the core material and the shell is fabricated by chemistry process such as in-situ polymerization, interfacial polymerization or by physical process such as pan coating, spray drying, solvent evaporation and so on [62]. The drawbacks of using mPCMs are concentrated on its low mechanical strength and the thermal conductivity which will be articulated in section 2.3.3.

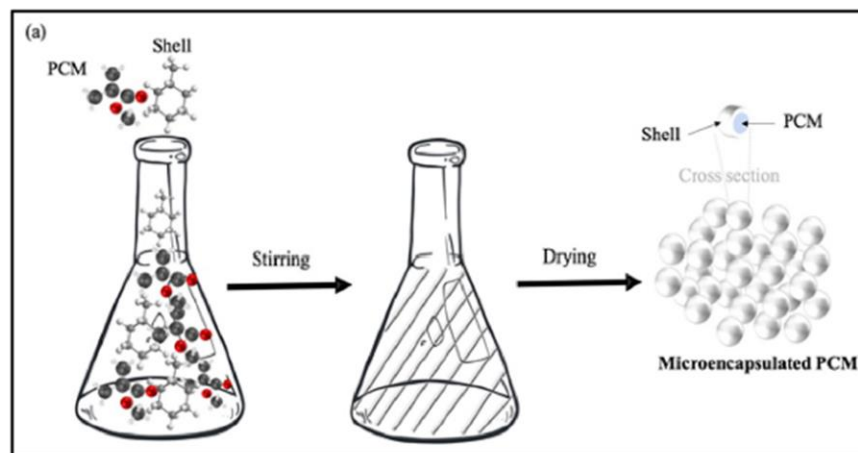


Figure 2-13 The schematic demonstration of fabricating the mPCMs [26]

2.3.3 Fresh, mechanical, and thermal properties of mPCMs incorporated cementitious materials

In recent years, since PCMs plays a promising role in increasing the energy efficiency of buildings and energy storage capability of construction materials. A large number of studies [26, 28, 62-67] trying to figure out the effect of PCMs on the fresh properties of the mixture, mechanical properties, and the thermal behaviour of PCMs incorporated cementitious material. In this research , the mPCMs is used as the additive in the cement paste, therefore the properties of mPCMs are emphasized in the following paragraphs.

Overall, the incorporation of mPCMs has a negative effect on the workability of modified cement paste. Higher water content is needed in the mixture for compensating the workability loss due to the presence of mPCMs [63, 64]. The possible reason is that the water is absorbed on the surface of polymer spherical shell, leading to the reduction of water which should have lubricate the cement-based matrix [68]. The reduction of free water in the cement pastes results in the increase of water/binder ratio, which is an important factor influencing mechanical properties of mPCMs incorporated cementitious material.

A general conclusion is derived by nearly every research which focus on studying the mechanical behaviour of mPCMs incorporated cementitious material that the decrease of compressive strength can be observed due to the inclusion of mPCMs, however the explanations of this behaviour are various and sometimes even contradict between different literatures. This is quite understandable since the type of mPCMs, the content of mPCMs used in mixture and incorporation method of mPCMs are devise from each research. For example, Cunha et al. replaced 20, 40, 60% weight of total mass of aggregate by mPCMs consists of paraffin was encapsulated in melamine-formaldehyde shell and the decrease of mechanical strength including flexural strength, compressive strength and adhesion was observed from the experimental results. The increased water-to-binder ratio as well as the porosity due to the presence of mPCMs were the major contribution to the mechanical strength decrease according to authors' investigation [69]. Jayalath et al. recognized the intrinsic low strength of mPCMs particle as the main contributor to the strength reduction of mPCMs incorporated cementitious material [33]. Šavija et al. [65] prepared cement paste with 0-30% per volume mPCMs inclusion, using mercury intrusion porosimeter to characterize the porosity of the mPCMs incorporated cement paste and concluded the increasing of porosity might be the minor factor leading to the strength decrease due to the fact that the pronounced porosity variety was captured only during 3-7 days after casting.

From the aspect of thermophysical properties, materials can be characterised by parameter such as the thermal conductivity k , which represent the ability of conducting heat. Material possessing smaller k indicates better thermal insulation. However, if the thermal conductivity is low enough that the heat is rarely conducted through the material the expected heat storage capacity cannot be fully utilized. It is not surprising that the thermal storage capacity increases when the content of mPCMs increases [33, 58, 63], meanwhile the thermal conductivity of mPCM-incorporated cementitious material decreases, which is attributed to the low thermal conductivity of mPCMs and the increased porosity induced by the mPCMs.

2.4 Summary

The literature review has covered three parts and provides technical knowledge and background for carrying out this research and fulfilling the research objectives. By introducing periodic and non-periodic honeycomb architecture on the material scale, better strength and stiffness with low density, higher crashworthiness and energy dispersion ability, excellent thermal and acoustic insulation capability have been achieved by synthetic metallic and polymeric products. The cell shape and size, the shape configuration, and the density of the cellular structure are of vital for determining the properties of architected cellular structure. Voronoi cellular structure as a typical stochastic honeycomb, generated by random distributed nucleation, has attracted researchers on combining it with metallic alloys, wood plastic, for the purpose of achieving the targeted function. However, the Voronoi cellular is rarely combined with cementitious materials. The influence of the randomness on the mechanical and thermal behaviour of cementitious composite is unclear and it deserved to put effort on. With the help of systematic research including experimental data collection and numerical simulation verification, this will be done in the present work.

Manipulating architecture of cementitious material has a great potential on optimizing the material properties, even achieving superior properties that cannot be achieved by the traditional casting. The complexity and special configuration of the tailored architecture has driven the manufacture process towards 3D printing process. The extrusion-based 3D concrete printing has its advantage in terms of automated cooperation with digital design model which indicates the enhance on the manufacture precision and efficiency as well as the labour-saving. This is a proper technique for fabricating construction scale blocks. Nevertheless, for manufacturing small specimens which are suitable for lab scale experiments, it is difficult to fulfil the rheological requirements of printable concrete. By combining with traditional casting method and 3D polymer printing, the so called “indirect 3D printing” process might be useful to tackle this issue, especially in the lab test.

According to literature review, the microencapsulated PCMs consists of paraffin wax as core material is one of the suitable additives in cementitious material aiming to improving its thermal performance. Generally, the mPCMs has negative impact on the workability and the compressive strength of PCMs-incorporated cementitious material due to the inactive polymeric shell of the mPCMs. Meanwhile, as the spherical particle resembles to artificially introduced air bobbles which lead to higher porosity, the PCM-incorporated cementitious material has low thermal conductivity. Furthermore, how the compressive and thermal behaviour of architected cellular cementitious composites made of PCMs-incorporated cementitious material is of interest and may offer a promising alternative of foam concrete blocks.

3

Fabrication of Lightweight cementitious cellular composites (LCCCs)

This chapter aims to describe the preliminary preparation process for the tests. A detailed description of the sample geometry mix design, slump tests as well as the sample preparation protocol is included. A total of five mix designs were employed for observing the effect of PCMS on the fluidity of mortar. Two suitable mixtures are chosen for sample casting. Two different specimen sizes were prepared for uniaxial compressive tests.

3.1 Geometry description

Voronoi tessellation is defined as the domain partition in the m dimensional space consisting of n distinct regions according to [70] and [71]. Each region, R_k , referred to as the Voronoi cell, is generated by corresponding point p_k , called seed. The Voronoi cell R_k represents the subset of the domain in which the distance of any point to the correspond seed p_k is always closer than its distance to other seed. Mathematically, this can be expressed as:

$$R_k = \{x \text{ in } X: d(x, p_k) \leq d(x, p_j), \text{ for all } j \neq k \} \quad (1)$$

In the present research, 2D ($m=2$) Voronoi tessellation is employed in MATLAB R2020a. In order to define the location of the randomly scattered Voronoi diagram's seeds, the 2D plane is meshed with $n \times n$ square cells (as shown in Figure 3-1). In each cell, a single seed point is located. The blue square in Figure 3-1 indicates the area where the seeds could be located, and the randomness depends on the ratio of blue square and the square cell. The randomness increases while the blue square become larger. The randomness is used to present the irregularity of structure. In order to determine the coordinate of points, the randomness $\delta = S/A$ is applied in MATLAB code. Theoretically, δ can be in the range from 0 to 1; the higher the δ , the more irregular the Voronoi geometry becomes. The generated points are then used as the seeds of the Voronoi partition. The function `Voronoi(x, y)` of MATLAB is applied to generate the Voronoi tessellation. Subsequently, the output of the code contains the coordinates of the vertices delimiting polygons associated with the seeds (see Figure 3-1).

In this research, 3 different randomness values - 0, 0.3, and 0.7 - are selected to investigate the effect of irregularity on the mechanical and thermal properties of cementitious cellular material. The process of experimental test and numerical simulation is elaborated in Chapter four and five.

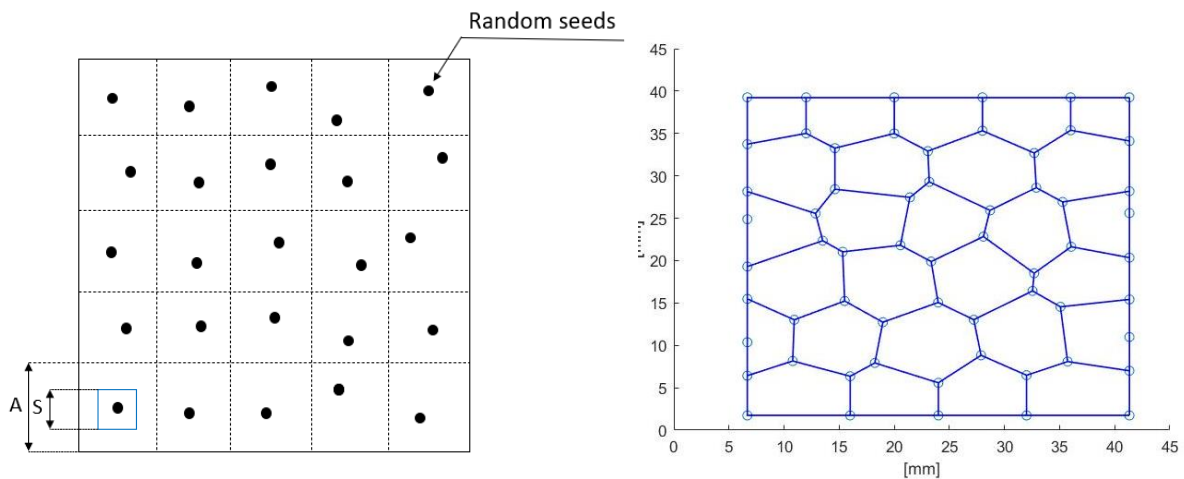


Figure 3-1 LEFT: The distribution of random seed in the square domain Right: The Voronoi tessellation generated in MATLAB

3.2 Mix design for preparing the reference and PCMs incorporated cementitious mortar

Prior to designing the mixture proportions of the cementitious materials, the requirements for the mixtures have to be verified. According to the literature, incorporating mPCMs enhances the thermal performance of the cementitious materials, so a high mPCMs content is preferred. However, the mPCMs are known to have a negative effect on the mechanical properties; with the increasing PCMs inclusion volume, the compressive strength of the mPCMs incorporated mortar decreases [67]. It is known from [65], by incorporating 20% volume of the same type mPCMs used in this study, the 28d compressive strength decreased around 50%, which can be considered a considerable decrease. Romero Rodríguez et.al [72] found that containing high amount (30% by volume of cement paste) of mPCMs in the mortar results in the decrease of the mechanical strength by 55% when they applied another kind of mPCMs for investigating the effect of mPCMs addition on the frost resistance of mortar. So, the volume fraction range of the mPCMs is limited up to 20% of total volume. In this research, mPCMs consists of core material and shell material. The paraffin waxes as the core material are encapsulated in the melamine formaldehyde (MF) shell for precluding the leakage of core material, along with resisting the corrosion, thereby facilitating the desired function. According to the data provided from manufacturer, the latent heat of fusion of the used mPCMs is 143.5J/g and the median particle size is 22.53 μm [65]. Furthermore, in this study the specimens are prepared in the same way as reported in [73, 74] (explained later). Therefore, highly fluid mixtures are of great help in filling the moulds, which is paramount for the quality of the hardened samples after 28 days curing. Considering these requirements, a mPCMs incorporated mortar with a moderate content of mPCMs while maintaining the fluidity is used herein. Accordingly, a reference mix design (REF) with high fluidity is adopted from [75, 76]. This mix comprises CEM I 42.5 N and fly ash as binder material and fine sand as aggregate. The water-to-binder ratio of the REF mixture is 0.33. Based on the REF mixture, additional mixtures are designed by varying mPCMs content and water-to-binder ratio. The mixture design is listed in the Table 3-1.

Table 3-1 The proportion of REF and PCMs-S14 mix design(g/l)

No.	CEMI 42.5N	Fly ash	Sand	SP	PCMS	Water	w/b	PCMs volume ratio (%)	Slump flow (mm)
REF	550	650	550	2	0	395	0.33	0	243
PCM10	550	650	448	4	112	495	0.41	10	284
PCM14	550	650	385	4	165	495	0.41	14.4	243.3
PCMW3	550	650	385	2	150	395	0.33	14.4	96.4
PCM20	550	650	310	4	240	495	0.41	20	187

3.3 Slump flow test

The introduction of mPCMs into the cementitious mortar leads to a significant change of workability. In this research, the mPCMs incorporated mortar should be flowable enough for casting as well as obtaining sufficient strength of which is capable for fabricating load bearing composite. Aiming at investigating the workability of mPCMs incorporated mortar, mini slump tests were carried out. The concept of “mini-slump test” are proposed and the test procedure are devised by DL.Kantro [77] for evaluating the influence of water-reducing admixture on cement. It is proved that mini slump test is reproducible and reliable in terms of assessing the workability of cement paste and it is characterised by the spread of paste [78, 79]. The dimensional details of the cone are given in Figure 3-2. The mix steps are in accordance with EN 196-3:2005+A1:2008 (E). First, the dry material (cement, fly ash and sand) was placed in a Hobart mixer and mixed for 4 minutes. Then, the superplasticizer was dropped into the water and then they were added into the mixed dry material within 10 s. This was followed by mixing for 2 minutes at low speed. The mixer was then stopped for 30 s during which all paste adhering to the wall and the bottom part of the bowl was scrapped using a metal scraper, meanwhile the PCM powder was added. After that, the mixture continued for 2 minutes. The total mixing time is 8 minutes.

The paste was filled into a metal cone from the top opening which was placed on a glass plate. After 1minute, the cone was lifted rapidly but with a reasonable speed for remaining clear of flowing mortar as well as avoiding additional inertia on the mortar. The flowing mortar spread was measured on the surface of the glass plate, after waiting for 30s. For this, a digital image of the top view of the spread area was taken, and Image J software was used to precisely measure the average value of the orthogonal diameter d_1 and d_2 . The measurement was calibrated by a scale grid. It was observed in Figure 3-3 and Table 3-1 that the mini slump flow width of the cementitious mortar significantly decreases with increasing the volume fraction of the mPCMs. With the same water-to-binder ratio as the REF mixture, more water is required to main the same workability (slump flow) after adding mPCMs. For the purpose of developing the mPCMs incorporated mortar for which reasonable workability for casting as well as sufficient amount of mPCMs are required for facilitating thermal performance, the PCM14 was eventually selected as the mPCMs incorporated mortar mixture design.

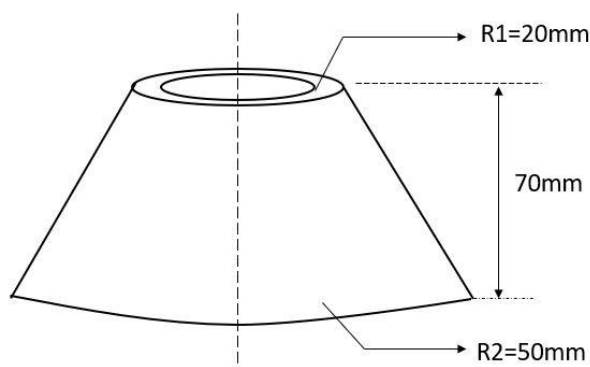


Figure 3-2 Schematics of the mini slump cone

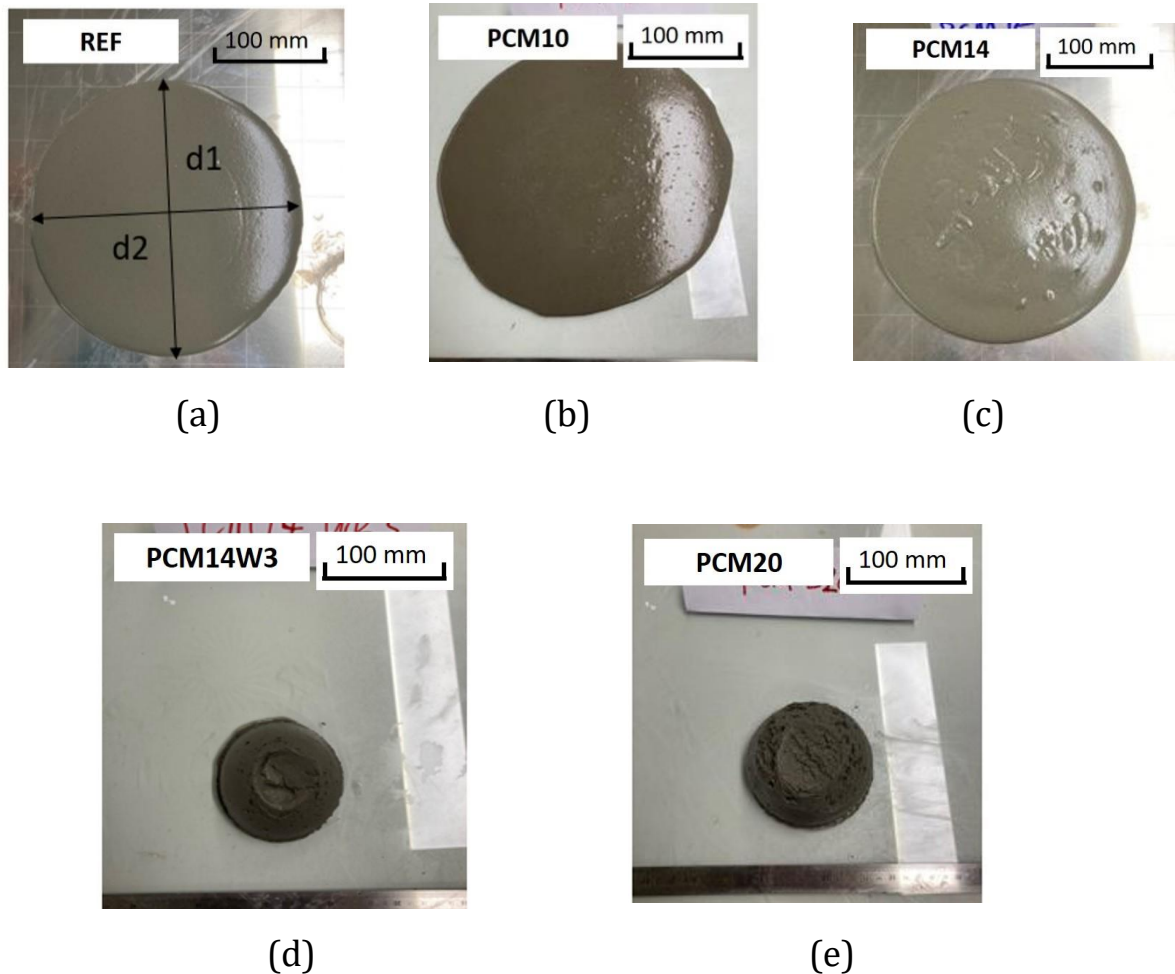


Figure 3-3 The slump flow (a)REF, (b)PCM10, (c)PCM14, (d)PCM14W3, (e)PCM20

3.4 Specimen preparation

The cellular structures of the LCCCs developed herein are architected by varying the randomness of the Voronoi geometry. Normally, the mechanical properties of cellular materials are influenced by the cellular porosity (relative density) [80, 81]. Therefore, the specimen design employed herein was performed under the premise of keeping a constant porosity (the deviation should be smaller than 5%) for different designs. Two sizes of specimens were manufactured in this study: specimens with the size of 48 mm (length) \times 46 mm (width) \times 40 mm (height), referred to as H40; and specimens with the size of 24mm (length) \times 23mm (width) \times 20mm (height), referred to as H20. Aiming at normalizing the compressive strength of the tested sample, the H40 specimens were designed with a size defined by NEN-EN 196-1, a norm according to which the strength of the solid mortar had been determined. On the other hand, the H20 specimens were fabricated with the aim of getting an insight of compressive behaviour of the cementitious cellular materials. A smaller size was required because the compressive strength of the H40 design was beyond the capacity of the hydraulic testing machine

needed to measure the complete compressive stress-strain response, including the post-peak behaviour. The characteristics of two groups of specimens are given in the Table 3-2 and Figure 3-4.

Table 3-2 Characteristics of specimens

Randomness of specimen	Porosity	Cell wall thickness (mm)
0	0.498	2(for H20 is 1)
0.3	0.493	2(for H20 is 1)
0.7	0.484	2(for H20 is 1)

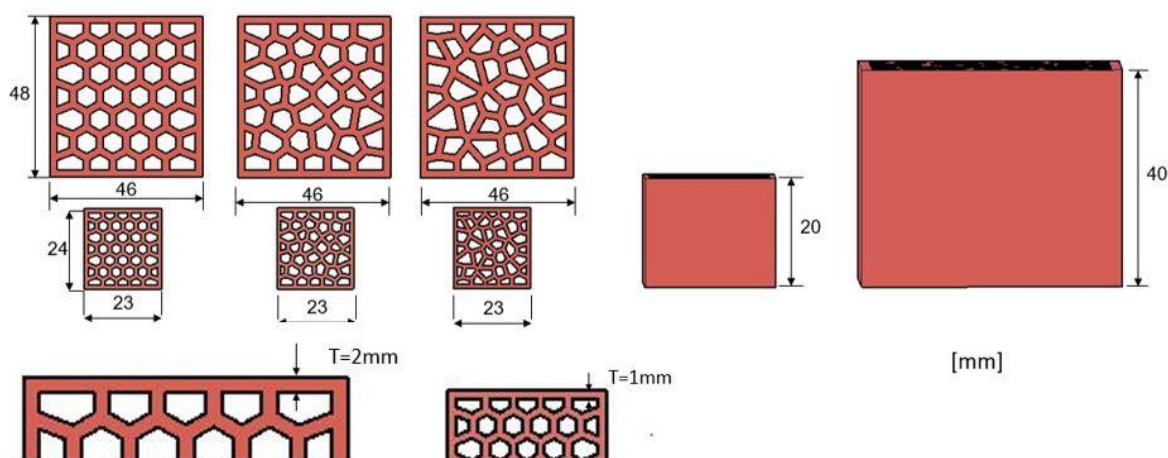


Figure 3-4 The schematic demonstration of size and thickness of specimens with three different randomness

The specimens were fabricated employing a so-called “indirect 3D printing” workflow proposed in [73]. The same procedure is followed herein and is described as follows:

- In the first step, the digital model design of Voronoi honeycombs with 3 different randomness was conducted in AutoCAD, after which the digital models have been exported as the stereolithographic format (STL). The models in STL files were decomposed into stacks of 2D slices, saving as a G-code program to benefit the printing process. The ABS (acrylonitrile butadiene styrene) mould was fabricated using fused deposition modelling (FDM) method by employing a commercial 3D printer (Ultimaker 2+). The ABS was heated up until 260 ° C, becoming semi-liquid, and then extruded with a nozzle diameter of 0.8mm. The nozzle path was based on the contour of designed geometries. Each filament layer was 0.2mm high and the printing speed 40mm/s.
- After 3D printing, the ABS mould was glued to the bottom of a cardboard box. A mixture of two component silicone rubber (consisting of Poly-Sil PS 8510, mixed 1:1 by weight) was poured into the ABS mould. The mould was then put into a vacuum chamber for extracting the air from silicone rubber. After 2h, the silicone rubber mould had hardened.
- The hardened silicone rubber mould was easily detached from the initial ABS mould. It should be noted that the mould is completely reusable. The fresh mortar is poured into the silicone

rubber mould and compacted. After 2 days, the cementitious cellular specimens are demoulded and cured under water until testing at 28 days.

The details of the specimen preparation working flow are given in Figure 3-5. In addition to cellular samples displayed in Figure 3-6, reference and PCM14 mortar specimens were casted into cube for compressive strength test and cylinders (height 20 mm, diameter 54 mm) for thermal conductivity tests. These results were also needed as input for the numerical simulations.

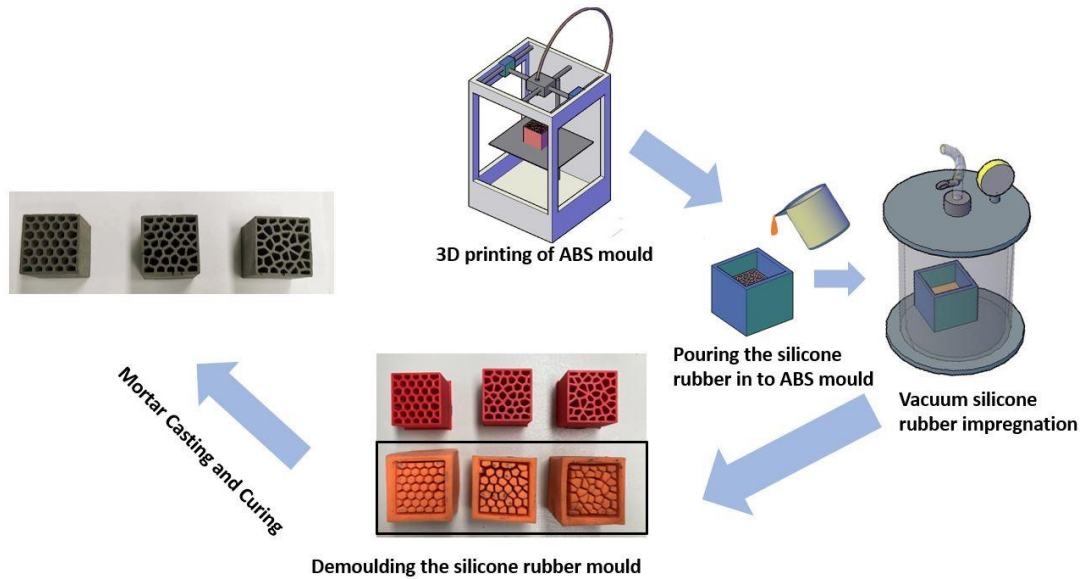


Figure 3-5 Specimen preparation workflow

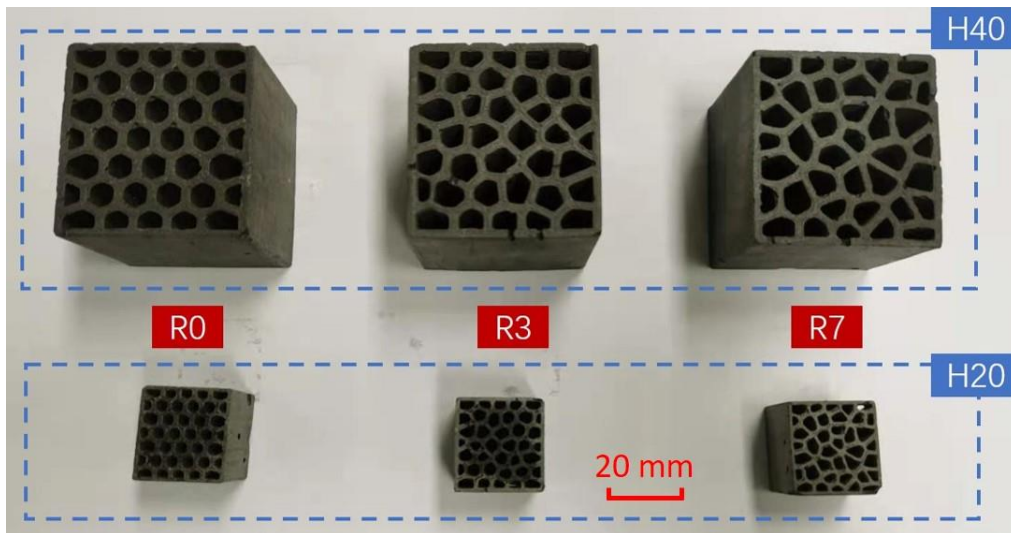


Figure 3-6 Casted cementitious cellular specimens

4

Experimental tests

This chapter describes the theoretical background and the experimental set-up. During the mechanical test, the force and displacement of specimen were recorded by the Instron hydraulic testing machine and Linear variable displacement transducer (LVDT). The transient plane source (TPS) method was used for measuring the thermal conductivity of cementitious material and they are used as the input parameter of numerical simulation.

4.1 Uniaxial compression test

To evaluate the compressive strength and compressive behaviour of the specimen including pre-peak and post-peak stages, displacement controlled uniaxial compressive test were conducted by employing INSTRON 8872 servo-hydraulic press, with the fixed rate of displacement is 0.003mm/s. The specimen is generally loaded in a stiff loading frame through a hydraulic actuator. The servo-valve is mounted on the hydraulic actuator to control the flow of oil in the actuator. The load is measured by load cell (see Figure 4-1). The test is displacement-controlled testing for measuring both pre-peak and post-peak response of specimens which indicates the axial displacement is measured over the total specimen length as the control variable.

As discussed in Section 3.4 that two groups of specimen were fabricated for the compression test. A smaller size (H20) was required because the compressive strength of the H40 design was beyond the capacity of the hydraulic testing machine needed to measure the complete compressive stress-strain response, including the post-peak behaviour. On the other hand, according to van Mier 's research [82], the cornerstone of a stable compressive test is to balance the energy released from elastic part of the specimen and the loading frame during the softening process. In the case of cementitious material which cracks rapidly, a very fast response time of the loading system is required, the relative smaller specimen testing is controlled easier.. This might be another reason two specimen sizes were used in this study

The uniaxial compression experiment setting up configuration is shown Figure 4-2. During the experiment, the frictional restraint has played a role on influencing the outcome of test, the boundary of the specimen must be remained straight, therefore the surfaces of specimen was polished by using sandpaper. The specimen was placed on the steel plate; a plastic film was utilized as the interlayer between specimen and steel plate for the purpose of reducing the effect of friction restraint on the test result. The stress-strain curve was calculated from the force versus displacement data recorded during the test. During testing, Linear Variable Displacement Transducers (LVDT) were installed on the side face of the steel plates for recording the displacement of specimen.

Due to the load limitation of INSTRON 8872 which provides maximum 10KN compression, the peak force of H40 specimen cannot be measured. The manual hydraulic press possesses maximum 250KN load was utilized as the principle of load control testing (see Figure 4-3). During the test, the upper press face lowered until contacting with the top face of the specimen, then push the pump to build up the pressure on the specimen, after the specimen fractured, recorded the maximum load which is recognized as the peak load. The peak strength was calculated from the peak load divided by cross section area. The four duplicated tests were carried out on each kind of design.

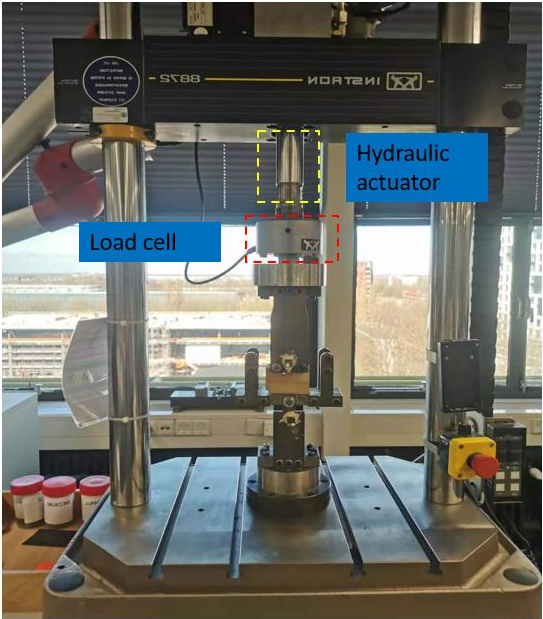


Figure 4-1 The INSTRON 8872 servo-hydraulic press

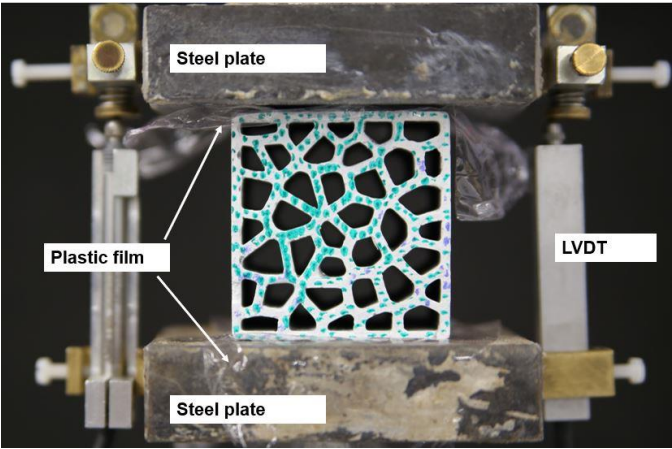


Figure 4-2 The uniaxial compression experiment setting up configuration



Figure 4-3 Left: The operation of manual hydraulic press. Right the detailed demonstration of specimen

4.2 Thermal properties test using transient plane source (TPS) method

To precisely analyze the thermal performance of LCCCs, the heat transport properties of the material itself, such as thermal conductivity and specific heat capacity, should be measured to provide input of the numerical thermal simulation. As known, the commonly used thermal conductivity measurement devices are steady-state device and transient device. The former measurement depends on creating the constant temperature difference on the top and bottom boundary of the tested sample and measures the heat flow through the specimen due to the temperature difference, whilst the latter device measures the time-dependent heat dissipation through the specimen, the increasing of temperature is measured as the function of time. The steady state device has its advantage since the simple operation and the thermal conductivity on the thickness direction is generated based on the Fourier's Law, however the prerequisite of the effective steady state measure is that the specimen reaches the thermal equilibrium which takes a long duration. Compared with steady state method, the transient method offers shorter test time.

The transient plane source (TPS) method, also known as Hot disk method, which belongs to one of the transient test methods, have received an increasing attention in recent years due to its ability of determining isotropic and anisotropic behavior of thermal conductivity suitable for a great range of materials: solids, liquids and powders [83]. The TPS method was first proposed by Gustafsson [84], and the detailed information in terms of how to apply this method for determine the thermal conductivity and diffusivity of tested material is recorded in International Standard (ISO22007-2:2008)[85]. The transient source plane element (hot disk sensor) is usually made by thin metal foil in the form of a bifilar spiral, acts as both heat source and temperature sensor [86]. This TPS probe was embedded within two layers of cementitious specimens with a diameter of $\phi 54\text{mm}$ and a thickness of 20mm (As shown in Figure 4-4). The age of specimens used for thermal properties test is 7 days. The REF and PCM14 were cast in the lab and were poured into the cylinder containers for curing. After 7 days' curing, the cementitious plate was cut as the required size for thermal test (see Figure 4-5). As shown in Figure 4-6, the mass of 2.2 kg was applied on the specimen for compressing the specimen to achieve a better contact between the sensor and the specimen. After the initial setup, an amount of electric power (e. g. 20mW) was applied to the sensor. A heat pulse in the form of a stepwise function was produced by an electrical current through the hot disk sensor to generate a dynamic temperature field. When the temperature increased, the corresponding voltage decreased due to the increasing resistance of the sensor and these voltage and current variation was recorded in the certain period, consequently the heat flow information between the sensor and tested material was captured. After a short time, once the temperature variation over the electrically insulating Kapton layer which was attached to the surface area of specimen where the sensor contacted with stayed constant due to the liberation of constant power, the thermal conductivity and diffusivity could be determined, provided the criteria for the penetration depth of the temperature transient into the sample $\Delta_p = 2 \cdot \sqrt{D \cdot t}$ (D is the thermal diffusivity of the material and t is the measuring time of the experiment) are met.

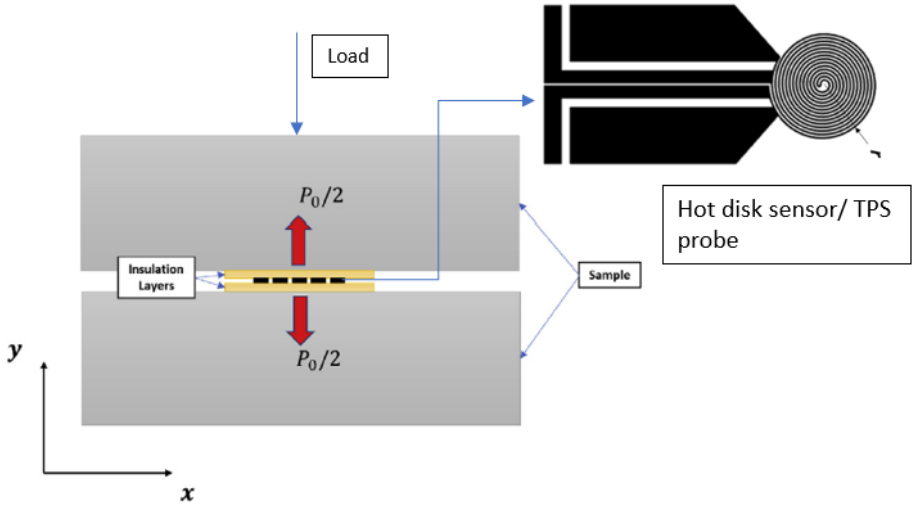


Figure 4-4 The schematic diagram of TPS set up, adapted from [87]

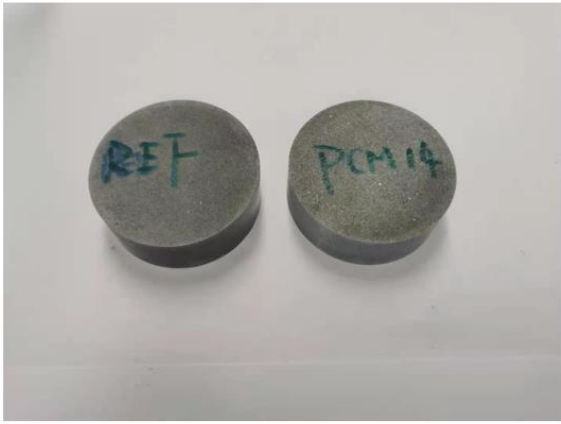


Figure 4-5 The demonstration of preparing the thermal test specimens

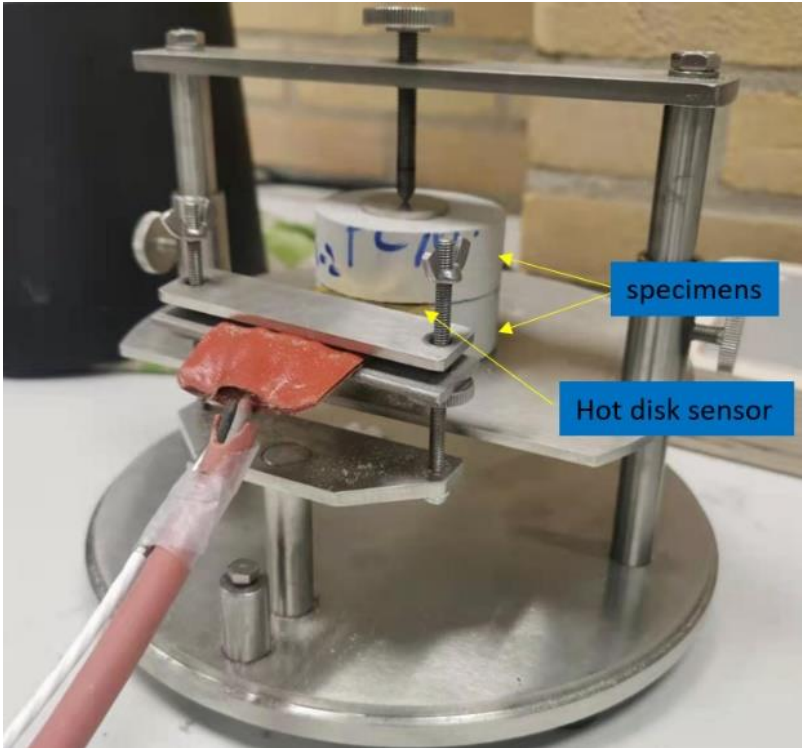


Figure 4-6 The realistic demonstration of thermal test in the lab

5

Numerical simulations

This chapter is dedicated to introducing the numerical models of mechanical and thermal simulations. The principle and the governing equation of concrete damage plasticity model (CDPM) used as the mechanical simulation model in the Abaqus software have been articulated in the first section, followed by the elaboration of the simulation set-up. The steady state heat transfer analysis is emphasized as the second part, how the conductivity, convection and radiation are considered in the thermal simulation is described in this chapter. Moreover, the effect of natural convection in the pores of LCCCs studied by using ANSYS is briefly concluded.

5.1 Concrete Damage Plasticity (CDP) Model

In this research, numerical simulations have been carried out by employing Commercial Software ABAQUS. The principle of analysing damage process of the cementitious materials is based on the Concrete Damage Plasticity Model [87, 88]. The CDP model considers the effect of plasticity damage on the compressive and tensile response of the material and the formulation is as expressed in Eqs (2,3,4,5). By conducting the compression test on cementitious cubic specimen and bending test on cementitious prismatic specimen, the initial elastic modulus E_0 , compressive inelastic strain $\varepsilon_c^{in,h}$ and tensile cracking strain $\varepsilon_t^{ck,h}$ are obtained. $\varepsilon_c^{pl,h}$, $\varepsilon_t^{pl,h}$ are compressive plastic strain and tensile plastic strain, which are key parameters for controlling the compressive and tensile failure. They are derived from $\varepsilon_c^{in,h}$ and $\varepsilon_t^{ck,h}$ and their corresponding damage parameter d_c, d_t . The damage parameter represents the elastic modulus reduction, which is calculated based on the ratio of nominal stress and ultimate strength. $d_c = 1 - \frac{\sigma_c}{\sigma_{cu}}$, $d_t = 1 - \frac{\sigma_t}{\sigma_{tu}}$. The CDP model is calibrated by these parameters which are denoted as the compressive behaviour and tensile behaviour input of cementitious material.

$$\sigma_c = (1 - d_c) \cdot E_0 \cdot (\varepsilon - \varepsilon_c^{pl,h}) \quad (2)$$

$$\sigma_t = (1 - d_t) \cdot E_0 \cdot (\varepsilon - \varepsilon_t^{pl,h}) \quad (3)$$

$$\varepsilon_c^{pl,h} = \varepsilon_c^{in,h} - \frac{d_c}{(1-d_c)} \cdot \frac{\sigma_0}{E_0} \quad (4)$$

$$\varepsilon_t^{pl,h} = \varepsilon_t^{ck,h} - \frac{d_t}{(1-d_t)} \cdot \frac{\sigma_0}{E_0} \quad (5)$$

5.2 Model calibration

To calibrate the model input parameters, numerical uniaxial compressive and tensile tests were performed on the cubic (15mm×15mm×15mm) and prismatic specimens (40mm×40mm×160 mm). As CDPM is intrinsically mesh size dependent, 1 mm tetrahedron elements were used for all simulations in this work. Compressive input and tensile parameters (presented in Table 5-1 to Table 5-4) were obtained by a trial-and-error method to fit experimentally obtained stress-strain and flexural-deflection curves. Boundary conditions of the numerical uniaxial compressive and bending tests the same as in the experiments: in compression, two rigid body plates were generated to apply the external load on the specimens; in bending, four loading rollers were used to apply the external load. Frictionless contact was assigned for the contact between the rigid plates/loading rollers and the specimen top and bottom surfaces. All degrees of freedoms (DOFs) of each rigid plate/loading roller were constrained on a reference point at the centre of the plate/roller. Vertical downwards displacement was applied on the reference point on the top while other DOFs of the reference point were completely fixed. All DOFs of the reference point on the bottom plate were completely fixed. It

can be found in Figure 5-1 that simulated uniaxial compressive and flexural curves show good agreement with experimental curves, which allows the use of calibrated input parameters in further simulations.

Table 5-1 Compressive input parameters of REF

Yield stress (MPa)	Inelastic strain	Damage parameter
30.4	0	0
33.6	0.001115	0
14.4	0.013047	0.571429
7.68	0.020946	0.771429
3.44	0.025923	0.897619
0.88	0.037988	0.97381

Table 5-2 Tensile input parameters of REF

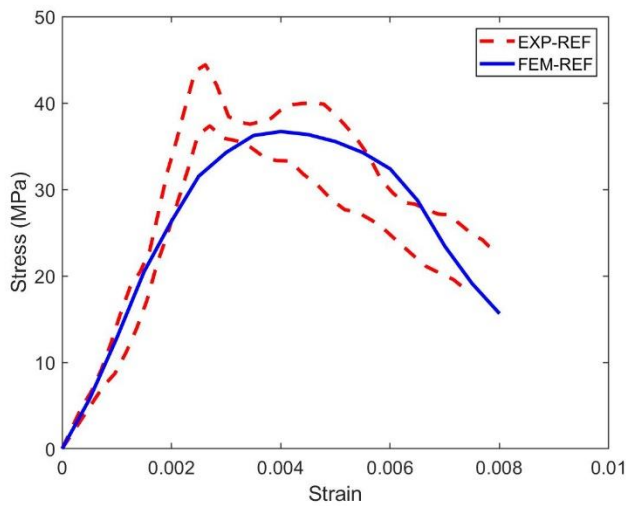
Yield stress (MPa)	Cracking strain	Damage parameter
5.25	0	0
3	0.000172	0.428571
1.5	0.000417	0.714286
0.45	0.000688	0.914286
0.15	0.000808	0.971429

Table 5-3 Compressive input parameters of PCM

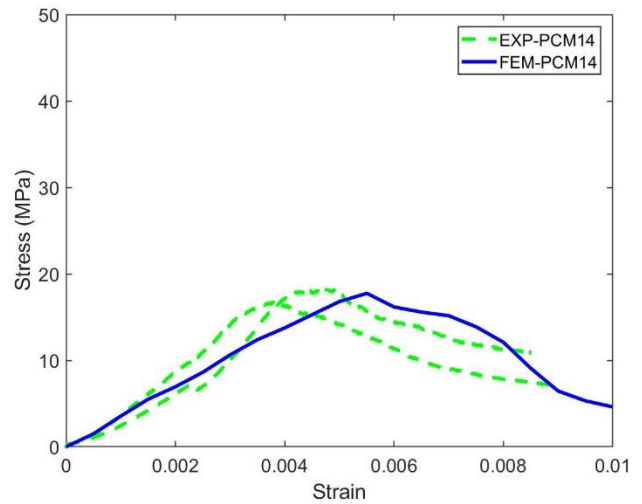
Yield stress (MPa)	Inelastic strain	Damage parameter
11.2	0	0
16.8	0.000264	0
7	0.014235	0.583333
3.5	0.02614	0.791667
1.4	0.032141	0.916667
0.3	0.048684	0.982143

Table 5-4 Tensile input parameters of PCM

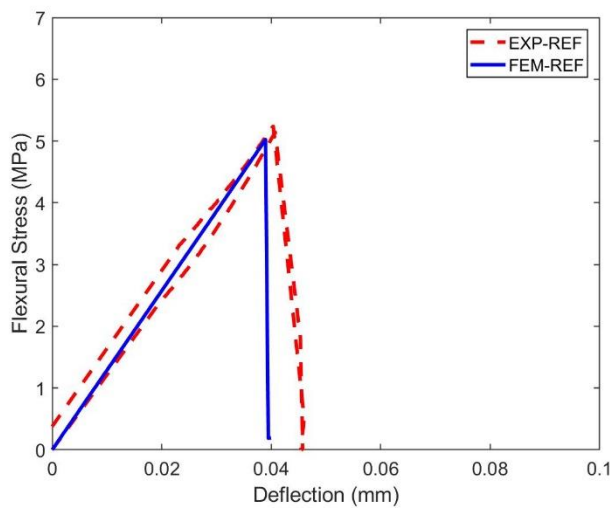
Yield stress (MPa)	Cracking strain	Damage parameter
1.8375	0	0
1.05	0.000237	0.428571
0.525	0.000516	0.714286
0.1575	0.00083	0.914286
0.0525	0.000971	0.971429



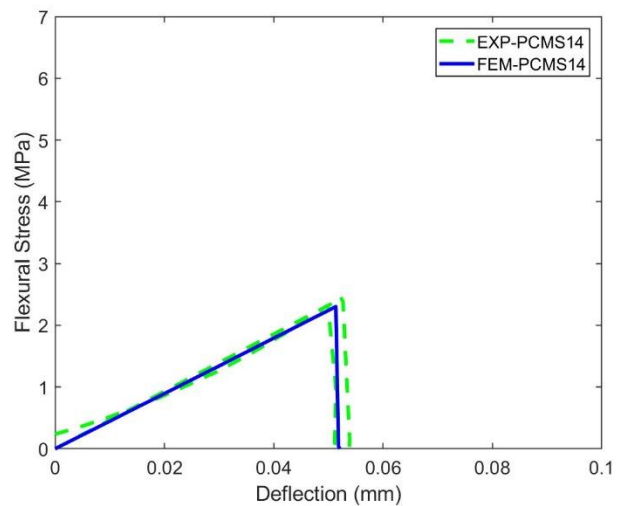
(a)



(b)



(c)



(d)

Figure 5-1 Comparison between experiment and calibration simulation results, (a) compression results of REF, (b) compression results of PCM14, (c) bending results of REF and (d) bending results of PCM14

5.3 Simulation of the cellular specimens

Considering the heterogeneity of cementitious materials, to simulate the mechanical response of the cementitious materials as precisely as possible, the microstructure or the meso-structured of the cementitious materials usually needs to be implemented in the numerical model. Heterogeneity exists on different scales. At microscale, for hardened cement paste, the geometry and local mechanical properties of the cement particles, hydration products and capillary pores usually need to be considered such that the simulated global mechanical response agrees with the experiments. When aggregates are present, the interface between the cementitious matrix and the aggregates also needs to be implemented. At the macroscale, which is the scale of this study, cementitious mortar is usually treated as homogenous material, but when air voids are present, the influence of air void structure needs to be specifically considered because it may cause stress concentrations. Normally, a certain amount of air voids (entrained or entrapped) exists in hardened cementitious mortar, especially at the surface of a specimen in contact with the mould surface. In the present study, due to the complex geometry of the specimen and the mould, there is much larger surface area in contact with the silicon moulds compared to specimens with regular shapes. Therefore, comparing to regular specimens there might be a higher chance that air bubbles agglomerate on the mould surface after casting and form air voids in the hardened specimens. Using computed tomography (CT) scan to provide reliable input for the numerical model is an option: however, the data size to be processed for each computational specimen is still prohibitive. Furthermore, for reliable results, usually several specimens need to be scanned and analysed which causes extremely heavy computing requirements. Therefore, herein, a simplified approach of generating the numerical model of the tested specimens is used in this study.

According to [89-91], the air void content of cementitious materials is around 1 %~6 % and the radius of air voids is commonly reported to mainly distribute from micrometres up to several millimetres. In order to study the influence of air voids, in this study, four air content values are used: 0%, 1.5%, 3% and 7%. Very small air voids require very dense mesh in the simulation, and they need extremely high computing effort. For simplification, spheres with radius ranging from 0.125mm to 1 mm, which are commonly found in cementitious mortar, are used to generate virtual air void structure of the cementitious mortar. Similar normal size distribution of this range reported in [92] was used for the generated spheres. The size distribution of the generated air voids is shown in Figure 5-2. The specimen generating process is shown in Figure 5-3, at first these spheres are randomly placed in a space 24 mm × 23mm × 20 mm (same size of the H20 specimens) then subtracted from the H20 specimens such that H20 specimens with different air void structures are generated.

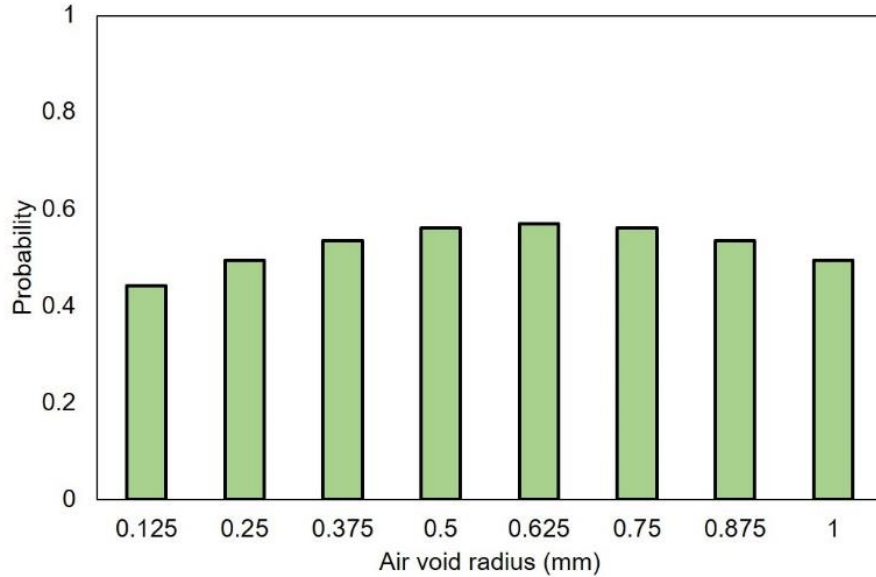


Figure 5-2 Distribution of air void radius

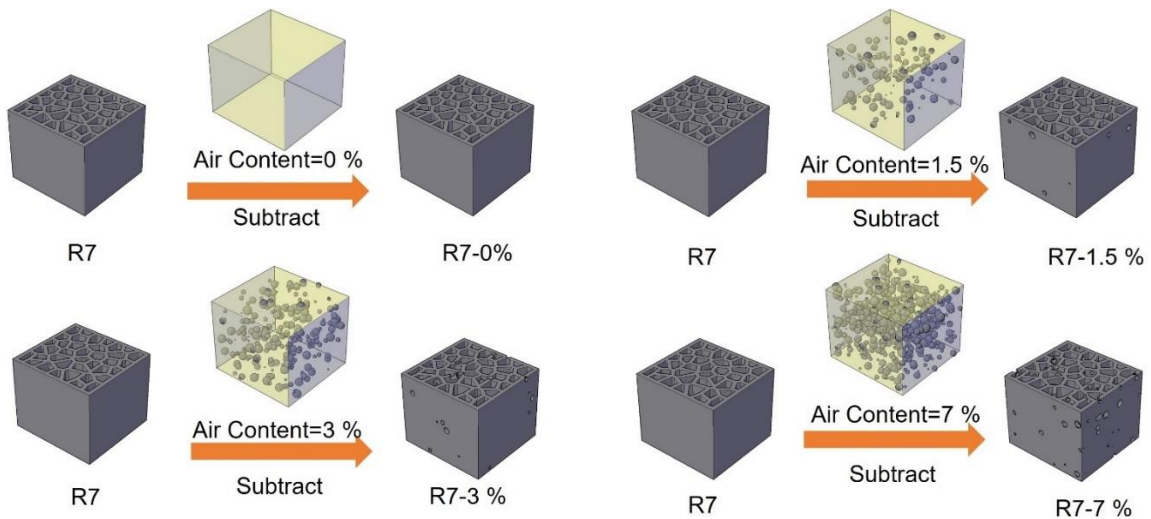


Figure 5-3 Schematics of generating cellular specimens with virtual air void structure

As shown in Figure 5-4, the simulation on the cellular specimens is performed in the in-plane and out-of-plane directions, respectively. In the out-of-plane direction due to the small contact area between the plate element of the specimen and the steel loading plates, the specimens are more easily influenced by the surface roughness of the steel loading plate. Under this condition, although plastic films were used in the experimental to decrease the confinement from the loading plate, friction should not be ignored. Under this condition, similar to the method used in [76], a minor friction coefficient 0.15 is used to avoid unrealistic sliding.

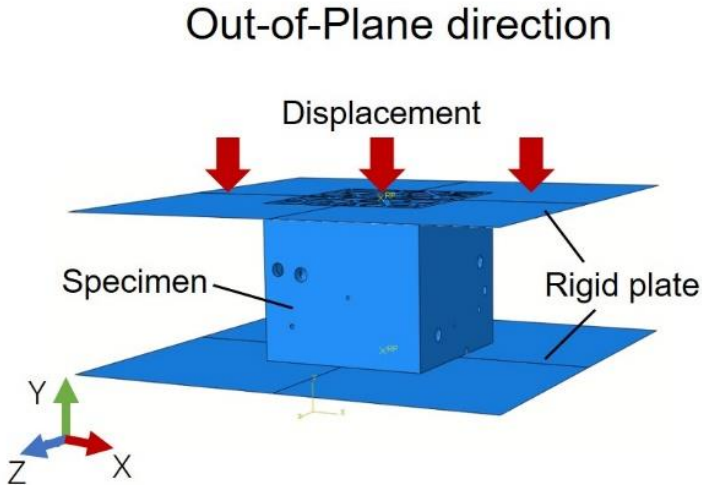
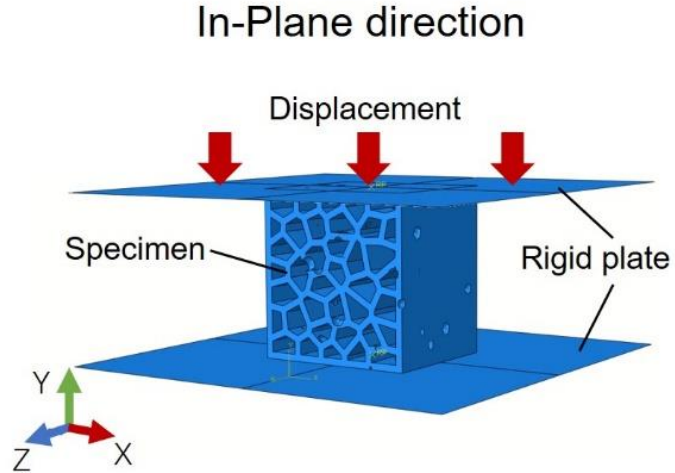


Figure 5-4 Loading setup in the simulation of the (a) In-plane direction and (b) Out-of-plane direction

5.4 Steady-state heat analysis

The 3D finite element model was developed in Abaqus CAE 2019 for exploring the thermal conductivity of the LCCCs, the effect of geometry randomness, density as well as the thermal bridge of the specimens on the heat transfer characteristics. The H20 specimen model (24 mm width \times 23mm length \times 20 mm height) was utilized for steady-state heat analysis (see Figure 5-5). Three modes of heat transfer: conduction, convection and radiation are considered in the simulations. It is shown in Figure 5-6 that pure conduction occurs through the solid cell walls in the specimen, convection and radiation occur through the inner cavities, the former process occurs as the air flow from the region of higher temperature to the lower temperature and the latter process depends on the material emissivity coefficient and the temperature variation of the inner cell wall [93]. Table 5-5 lists the thermo-physical properties of REF and PCM14 generated from the TPS test mentioned in section 4.2, the thermal conductivity and specific capacity of material are average value of 10 replicated tests and are assumed as the constant input in the simulation.

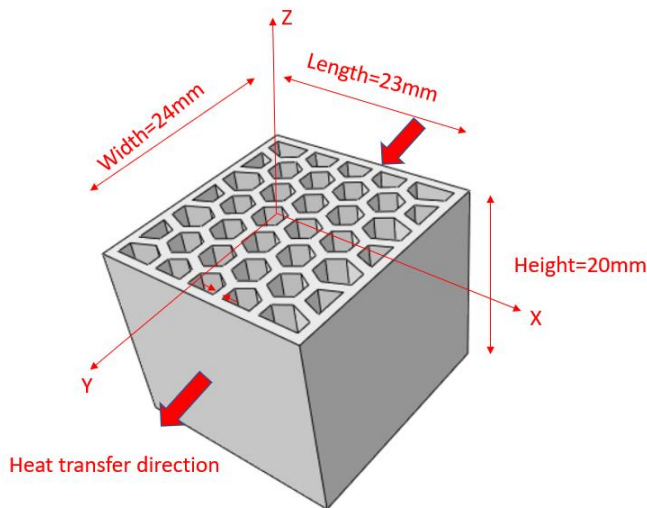


Figure 5-5 The dimension of H20 specimen and the heat transfer direction

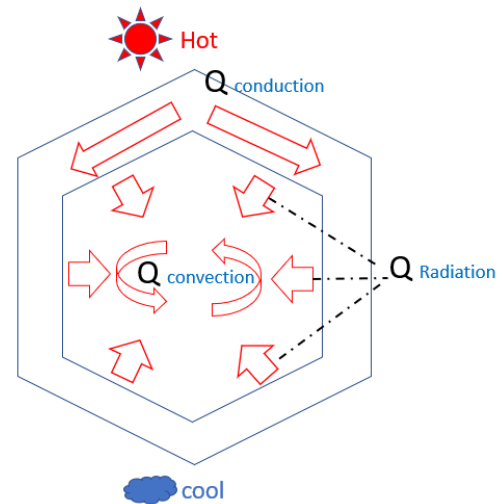


Figure 5-6 The schematic diagram showing the heat transfer mechanism inner the pore

Table 5-5 Thermo-physical material properties of REF and PCM14*

No.	Thermal conductivity (W/m·K)	Specific heat capacity(J/Kg·K)	Density (Kg/m ³)
REF	1.117	1171.7	1990
PCM14	1.372	1853.4	1780

* thermal property values are measured by TPS method described in the previous chapter

After assigning the material properties to the model, the linear heat transfer element was applied on R0, R3 and R7 model. The mesh type is hexahedron, and the mesh size is 0.5 mm. The total element number of R0, R3, R7 model is 46400, 51600 and 54040 respectively.

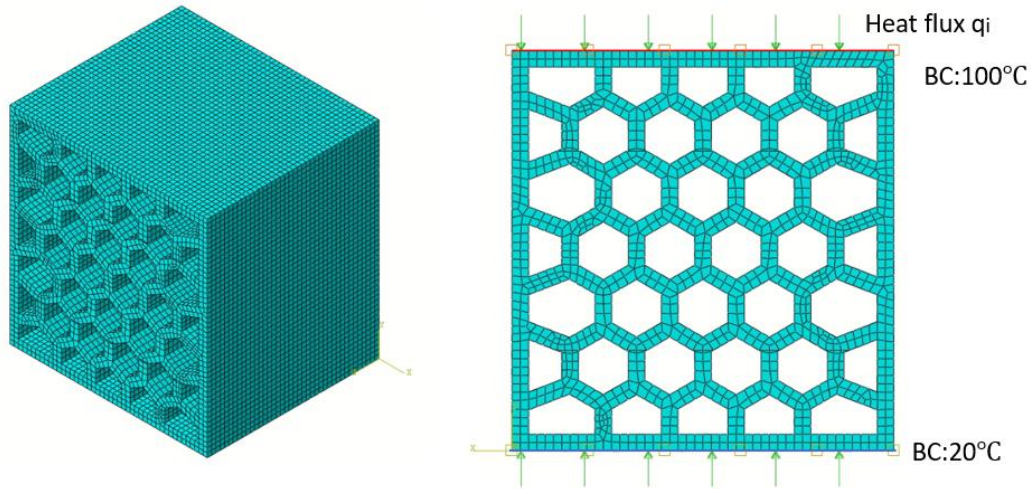


Figure 5-7 The simulation model and the applied boundary conditions in Abaqus

The boundary condition consists of two constant temperature surfaces, the upper surface temperature was taken as 100°C (373K) and the bottom surface temperature was taken as 20°C(293K) (see Figure 5-7). A heat flow was generated toward the cooler face, the thermal conductivity on the i direction of the applied thermal gradient can be calculated based on Fourier’s Law:

$$\lambda_i = \frac{-q_i}{S_i} \cdot \frac{d_i}{\Delta T} \quad (6)$$

$$q_i = \sum_{j=1}^N q_j \cdot S_j \quad (7)$$

Where S_i represents the cross-section area, which is perpendicular to the heat flow direction, q_i indicates the sum of heat flux of the cooler surface, q_j is the heat flux on the number j element (j is in the range of 1 to N , N is the total number of elements on the surface) of the cooler surface in the model

whereas S_j is the surface area of number j element. d_i represent the distance between the hotter and cooler face, which is equal to 24mm in the model and the ΔT is the temperature difference of two boundary condition which is 80°C.

In Abaqus, the radiation of inner cavities of the LCCCs was applied through cavity radiation interaction, which was performed by setting the emissivity coefficient and calculating the sink temperature which is the interior surface average temperature of each cell unit. Stefan-Boltzmann constant is $5.67 \times 10^{-8}(\text{W}/\text{m}^2\text{K}^4)$. Similarly, the convection of inner cavities depends on the surface film coefficient and the sink temperature [94]. In this research, radiation emissivity is assumed as 0.8 and film coefficient is assumed as 0.009, they were both adopted from materials thermal properties database [95].

5.5 Natural convection in the pore structure

Incropera and Dewitt [96] stated that the natural convection is induced by buoyancy force which is due to the density difference caused by temperature difference in the fluid, the force is proportional to the density and gravitational. The density of the air depends on the temperature, generally decreasing with the increasing of temperature. When the heat transfer through the fluid leading to the local volumetric expansion, the gravity induced pressure gradient occurs, the hot air rising off while the cooler air dropping down, resulting in the heat transfer by the means of fluid motion. Similar with the study of mechanical, the natural convection flow phenomenon take place both in in-plane direction and out-of-plane directions (see Figure 5-8), this phenomenon was studied numerically by using computational fluid dynamics (CFD) ANSYS 18.2 to formulate the 2D numerical model to analyse the behaviour of air flow, temperature distribution and density of the air in the cavities.

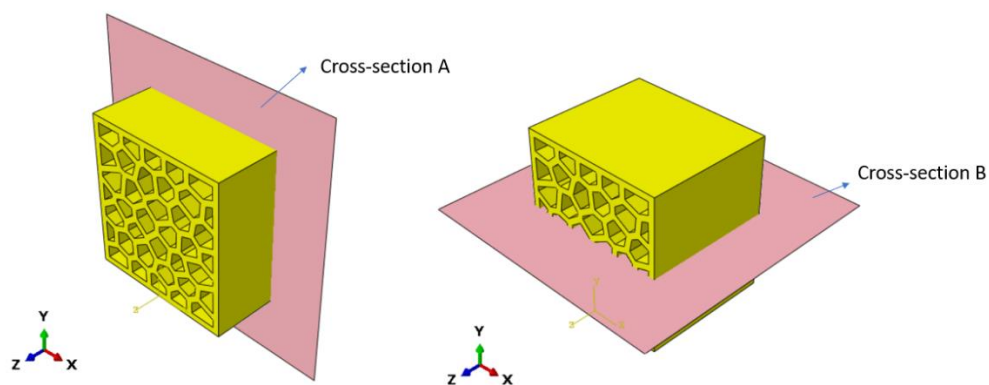


Figure 5-8 Left: cross section A indicates the natural convection takes place on the in-plane direction, Right: cross-section B indicates the natural convection takes place on the out-of-plane direction.

The ANSYS natural convection simulation on the in-plane direction aims to clarify whether the air flow has influence on heat transfer and verify the accuracy of steady-state method. The ANSYS results will be compared with Abaqus results and discussed in section 7.3. On the other hand, it is known that the air flow velocity on the height direction of a cellular construction (for instance: cavity wall) play an important role on heat transfer. When the air flow velocity increases, more heat loss exists in the process of fluid motion, therefore it is interesting to explore the relationship between the height of the cell and the air flow velocity and corresponding temperature distribution.

In the ANSYS workbench, the fluent analysis system was chosen and the geometry of R0, R3, R7 cross section was imported. After geometries were completed, it is important to define the proper mesh to yield more accurate result display since the mesh type and size determine the calculation method and speed. The triangular mesh was applied to the cross section with mesh size of 0.5mm. The general setup of the solver including the pressure-based with gravitational force acting downward $y=-9.81\text{m/s}^2$, transient method, 2D planar and absolute velocity formulation were carried out before the next analyzing steps. The properties of the air in the cavities were defined as incompressible-ideal gases with specific heat C_p equals to $1021\text{J/kg}\cdot\text{K}$ and thermal conductivity equals to $0.0371\text{W/m}\cdot\text{K}$. It can be seen in Figure 5-9 that the 2D model for analyzing the effect of height on air flow and heat transfer is simplified as a vertical rectangular enclosure space, the width of the space is 8mm (same with the one cell width in the H40 LCCCs) and the height is taken as 40 mm, 80 mm, 120 mm which are 5 times,10 times and 15 times of the width respectively. The boundary condition of the model was set on the two vertical walls of the enclosure wall, the hot wall was set with temperature as 299.15K while the cool one was set with temperature as 293.15K. In order to obtain the accurate results and guarantee the results were converged, the convergence threshold of each residual equation was set as $1\text{e-}06$. After finishing all the setup, the calculation started and the contour of air flow velocity, temperature distribution of the model has been displayed. The details of each steps of simulation setup will be demonstrated in Appendix A.

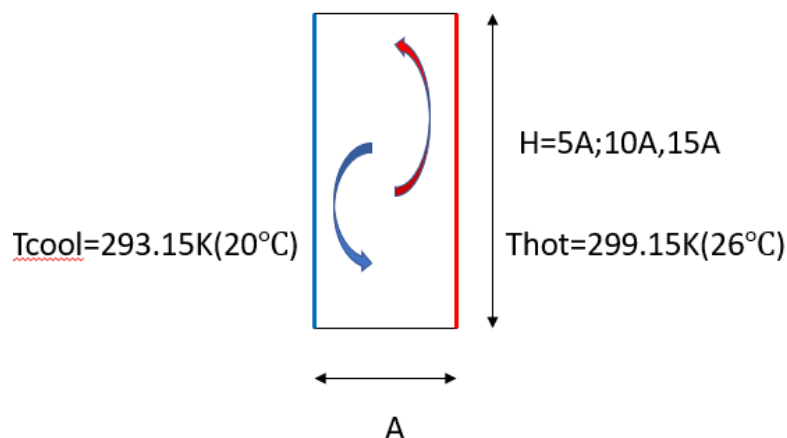


Figure 5-9 The schematic of natural convection in vertical rectangular enclosure

According to the velocity magnitude on the Y direction, it is concluded from Figure 5-11 that the air flow speed is relatively small which is 6.82×10^{-3} m/s, the effect of height on the natural convection is negligible. The thermal conductivity of the air in the vertical enclosure space keeps constant although the height of cavity increases from 40mm to 120mm (As seen in Figure 5-10). Moreover, the temperature distribution is uniform along the height and the temperature transition is linear along the width of the rectangular space, the effect of natural convection leading to the change of temperature distribution concentrates on the top and bottom area of the vertical enclosure (see Figure 5-11 (b)).

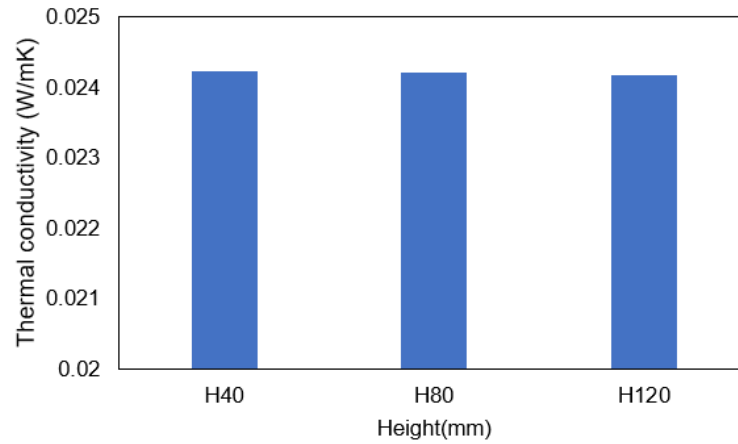
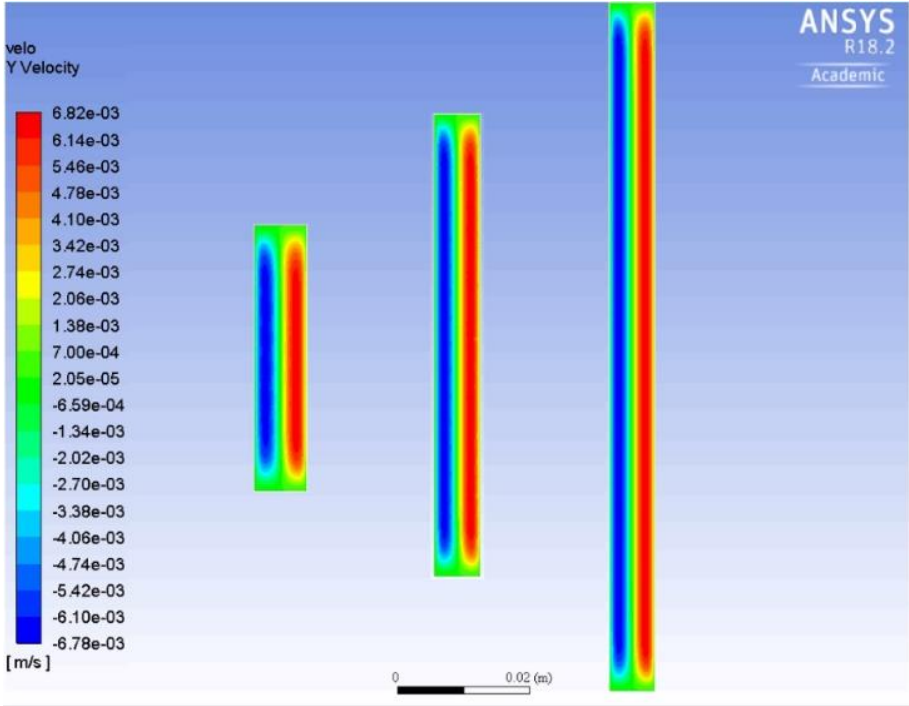
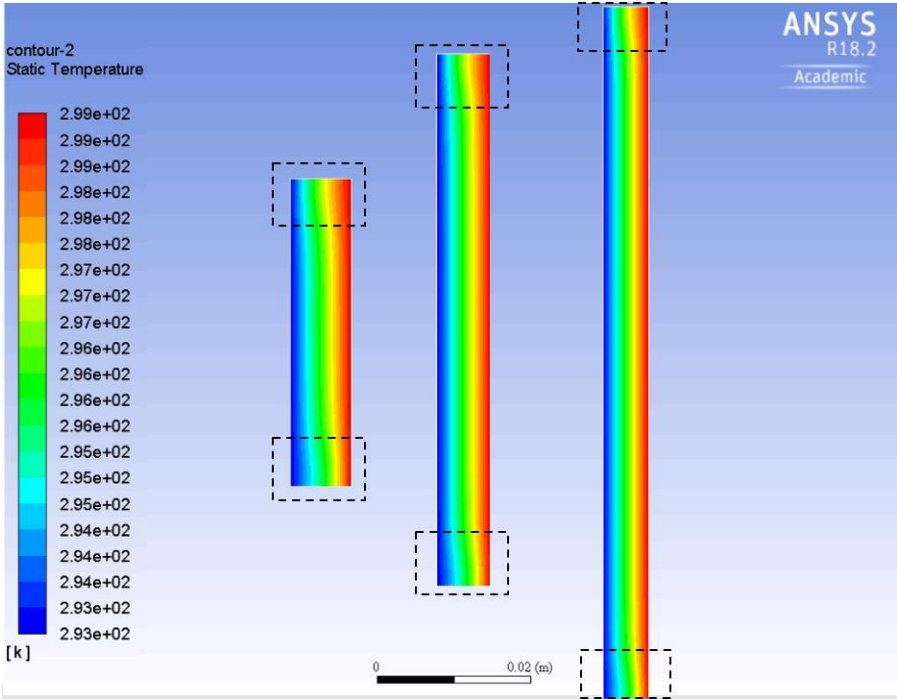


Figure 5-10 The thermal conductivity of air calculated from ANSYS simulation results, considering the variation of height including 40,80,120mm



(a)



(b)

Figure 5-11 (a) the contour of air velocity in the vertical enclosure (b)the contour of temperature distribution in the vertical enclosure, change of temperature distribution concentrates on the top and bottom area is marked as black dash line rectangular

6

Mechanical properties

This chapter studies the compressive behaviour of the LCCCs by experimental results accompanied by numerical simulations. Deformation and fracture of the developed LCCCs have been simulated using finite element modelling (FEM) in Abaqus. The comparison between the experiment results and numerical models in terms of the elastic modules of LCCCs, the stress-strain response and the post-peak behaviour due to the defects and the addition of PCMs are discussed

6.1 Out-of-plane compressive behaviour

At the advent of discrepant failure of specimen observed when load is applied on the different direction, many experts started to allocate attention on the effects of pores direction on the compressive behaviour as well as energy absorption of cellular material [97-99]. Specifically, the concept of anisotropy in compressive behaviour is embodied on the direction where the pores are loaded parallel to the compression (namely out-of-plane direction) and perpendicular to the compression (namely in-plane direction) in this research. The experimental results of compressive testing are discussed in detail, showing stress-strain curve in different directions and numerical simulation elaboration also helps author to equip the understanding of cementitious cellular material.

The compressive strength of cementitious material is one of the important factors determining the capability of damage resistance and it ought to be measured by standard testing. Thus, as mentioned in Section 4.1, H40 specimens were used in the mechanical test for measuring the compressive strength. Firstly, out-of-plane compressive strength of the R0, R3, R7 specimen were gauged by servo hydraulic press mentioned in section 4.1. For each randomness of two mixtures, 3 duplicated specimens were tested respectively. As discussed previously, the cellular specimens were designed under the premise of keeping the consistent porosity, which is around 50% among the three tested groups. Figure 6-1 shows the results of out-of-plane compressive strength. In general, the out-of-plane compressive strength of all cellular specimens is much lower than the material cube strength, as expected for specimens with such high porosity. Specifically, both for REF and PCMS14 specimens, specimens with a randomized structure (R3 and R7) show lower compressive strength than the regular honeycomb structure R0. For the REF specimens, compressive strength of R0, R3 and R7 is 7.4 MPa, 7.0 MPa and 5.8 MPa, respectively. Comparing to the REF specimens, all LCCCs specimens made of PCM14 have lower compressive strength in the out-of-plane direction. The compressive strength of R0 has the highest value of 6.1 MPa while R3 and R7 have lower values of 4.6 MPa and 5.1MPa. The possible mechanism of randomized specimens has lower compressive strength is discussed later through numerical simulation analysis. Considering the high porosity of the cellular specimens, in order to provide fairer comparison, the compressive strength of the cellular specimens is normalized by their porosities to the same volume of the cube specimens, defined as relative strength. The relative strength of the cellular specimens is obtained and also given in Figure 6-1. R0, R3 and R7 has a relative strength of 14.7MPa,13.7MPa and 11.3MPa respectively, decreasing around 60% compared with the cube strength which is 35MPa after 28 days curing. It can be found that even normalized by the porosity, the strength of the cellular specimens still decreases with the increased randomness. This may be attributed to the significant influence of defects or imperfections on the compressive behaviour of the cellular materials. More in-depth mechanism is elaborated later by comparing numerical results and experimental measurements of the H20 specimens.

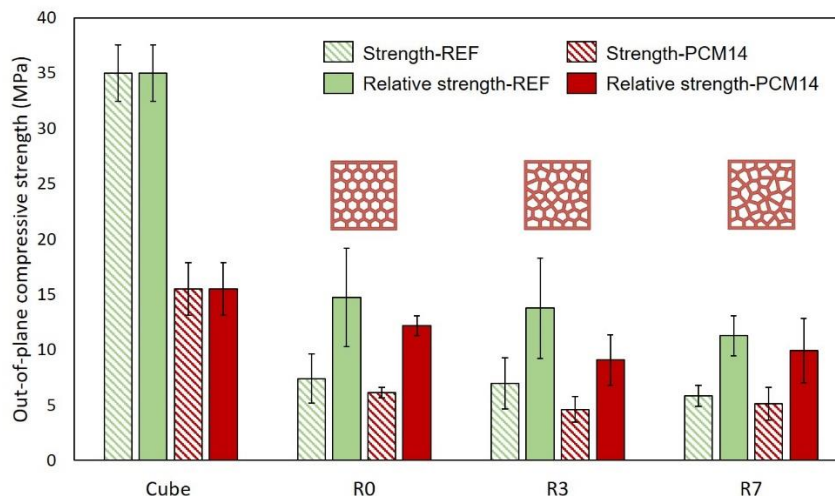


Figure 6-1 Comparison of out-of-plane the compressive strength between R0, R3, R7 (measured from H40 specimens) and the material cube strength

According to previous studies [26, 33, 67], it is concluded that the addition of mPCMs has negative effect concerning the mechanical strength of mortar. The microencapsulated PCM particles are soft and with low density (around 0.9kg/l) compared with other aggregate constituent in the mixture, leading to the overall strength reduction of cementitious materials. Besides, the strength reduction is also possibly attributed to the increasing porosity with the introduction of mPCMs particles. Depending on the mixture design, adding around 14% of mPCMs by volume results in a compressive strength loss of 20%-60% [26]. In this work the incorporated mPCMs is 14% of total volume and the cubic strength has decreased from 35MPa to 15MPa, 55.7 % of strength reduction.

Normally, the reduction in compressive strength is one of the main concerns of incorporating mPCMs with cementitious materials. However, for these lightweight cellular specimens, the compressive strength decreases due to incorporating mPCMs is much less notable. The R0, R3 and R7 specimens made of PCM14 mix has only decreased 17.2%, 34.0% and 12.1% of the compressive strength comparing to the REF group counterparts, respectively. Especially for R7, the reduction of out-of-plane compressive strength of R7 specimen between using REF (average value is 5.82Mpa) and mPCMs incorporated mortar (average value is 5.12Mpa) is significantly mitigated. This indicates that incorporating mPCMs within these lightweight cementitious cellular components could be a proper strategy to combing the high porosity feature of the lightweight LCCCs and the potential thermal property enhancement by mPCMs without sacrificing the mechanical properties. Considering the high porosity of the LCCCs, in engineering practice the LCCCs would be used as lightweight non-structural elements, for instance insulation panel or façade panels. In this sense, they would fulfil a role commonly fulfilled by foam concrete. As shown in Figure 6-2 the out-of-plane compressive strength of the LCCCs made of PCM14 is similar to the foam concrete with similar density. In terms of compressive strength, the mPCMs incorporated LCCCs would be a potential alternative to foam concrete in the context of non-structural applications using lightweight cementitious materials.

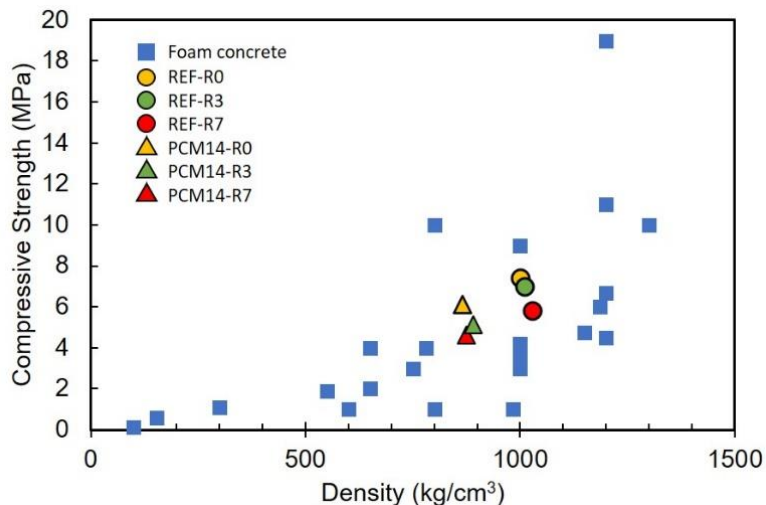


Figure 6-2 Comparison of the compressive strength of the cellular specimens with normal foam concrete [12, 14]

Owing to the testing set up limitation mentioned in section 3.4, the H20 specimen were used to study the complete compressive behaviour. It is observed in Figure 6-3 that, in the out-of-plane direction, the stress-strain response of the lightweight LCCCs is similar to conventional cementitious materials: for both REF and PCM14 specimens, as soon as external was applied, an ascending branch can be observed which indicates the elastic deformation stage. Afterwards, the slope started to flatten and followed by a peak stress of the specimen, then a softening branch occurs representing the process of post-peak. In terms of elastic deformation stage, usually when calculating the elastic modulus, up to stress level of 30% of peak stress σ_{peak} is chosen and divided by its corresponding strain, namely the slope of the stress-strain curve. In this work, $0.2 \sigma_{peak}$ is used for measuring the slope of all specimens. The value measured from the cubic specimens is regarded as the material E-modulus while the values measured from the LCCCs are comparatively regarded as the out-of-plane stiffness of the corresponding specimens. In the elastic regime, due to the existence of the pore structure, the stiffness of all tested LCCCs on the out-of-plane direction has dropped substantially, has fallen to around 50% of the material E-modulus. Nevertheless, when E-modulus of all tested specimen are normalized according to their porosity to the same amount of material (namely the relative E-modulus), the discrepancy between the material E-modulus and the stiffness of the LCCCs becomes much smaller. For LCCCs made of REF mixture, the stiffness of R0, R3 and R7 has only dropped 12%, 24% and 27% respectively. Especially for the LCCCs made of PCM14, after normalizing by the porosity the relative stiffness is even higher than the material E-modulus (see Figure 6-4). Among all LCCCs specimens R7 possesses the lowest stiffness compared with R0, R3 groups. It is assumed that, comparing to R0 and R3, air voids more easily get entrapped in R7 due to its more complex geometry. This will be discussed later in detail by comparative study between the experimental and numerical simulation results.

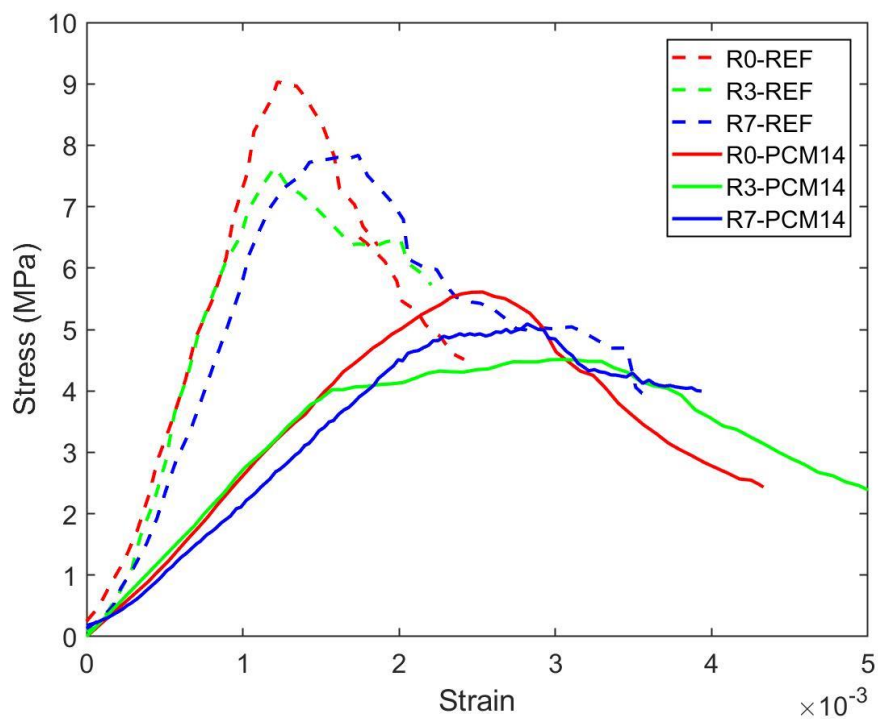


Figure 6-3 Stress-strain curves of the LCCCs on the out-of-plane direction, a) REF specimens; b) PCM14 specimens, measured from H20 specimens

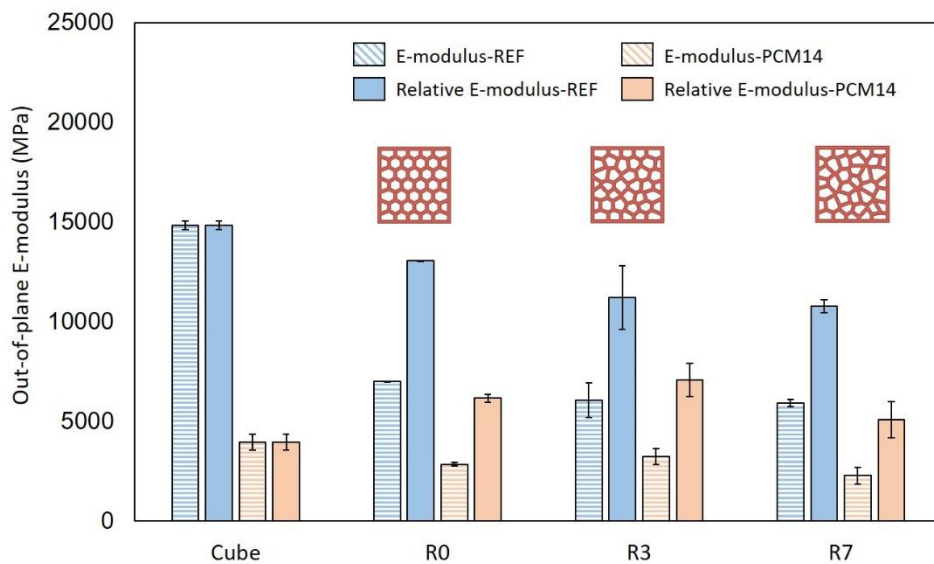


Figure 6-4 E-modulus of the lightweight LCCCs in the out-of-plane direction

After the elastic regime, a peak stress is reached for all test groups. It is worth noticing that the peak stress measured from H20 specimen is slightly higher than the compressive strength measured from H40 displayed in the Figure 6-1. It is plausible that the size effect [100] has influence concerning the peak stress which means the smaller specimens tend to achieve a higher compressive strength. Considering the geometrical features of the LCCCs, on the out-of-plane direction they can be seen as multiple thin-walled structure consisted by plate elements with various orientations. When loaded on the out-of-plane direction, the deformation and fracture behaviour of each plate determines the global behaviour of the cellular specimen. As mentioned previously, air voids commonly exist in cementitious materials and may become critical defects for the cellular specimens used in this study, especially if a void penetrates the plate element of the cellular specimen. From the theory of fracture mechanics, when external compressive load applied on top of an infinite plate, due to the structural discontinuity intensive compressive and tensile stress concentrates at the edge of the circular hole. In theory [101], three times of compressive stress appears at the direction perpendicular to the applied stress, and tensile stress concentrates at the parallel direction to the applied stress with the same absolute value. This was also simulated using a FEM tool, as shown in Figure 6-5 when 1MPa compressive load applied on top of a plate. Tensile and compressive stress concentrates at the edge of the circular hole. Note that in the FEM simulation the plate is not an infinite plate such that the compressive and tensile stress are not exactly theoretical values. For cementitious materials, the tensile strength is significantly lower than their compressive strength. In this work, the compressive strength of PCM14 and REF are around 8 times higher than their tensile strength such that cracks may initiate around the air voids at the location with high tensile stress concentration. After initiation, the crack propagates parallel to the direction of the applied load forming a vertical cracking along the plate (see Figure 6-6). These vertical cracks were also observed from the experiments and simulations of the LCCCs (see Figure 6-7). In this sense, the strength of those plate elements with air voids is significantly reduced, and these plate elements become critical parts of the LCCCs which eventually results in reduction of the compressive strength than the case without any introduced air voids. The more air voids are introduced, the more critical parts the LCCCs will have, and thus the lower compressive strength may be observed.

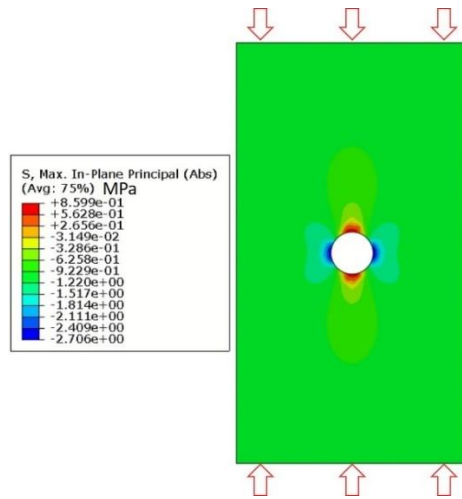


Figure 6-5 Stress concentration, crack initiation and propagating at the edge of a circular hole on a compressive loaded plate

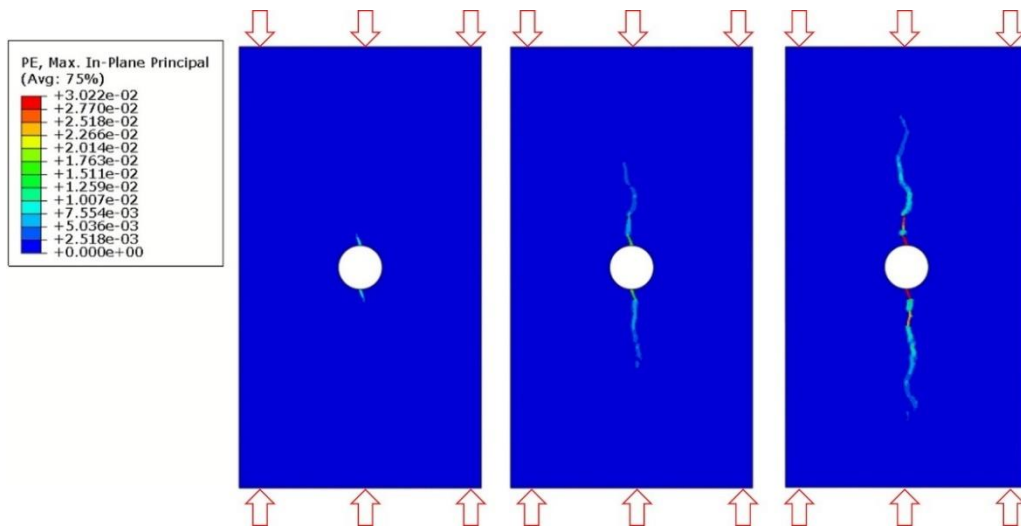


Figure 6-6 Crack initiation and propagation process on a compressive loaded plate

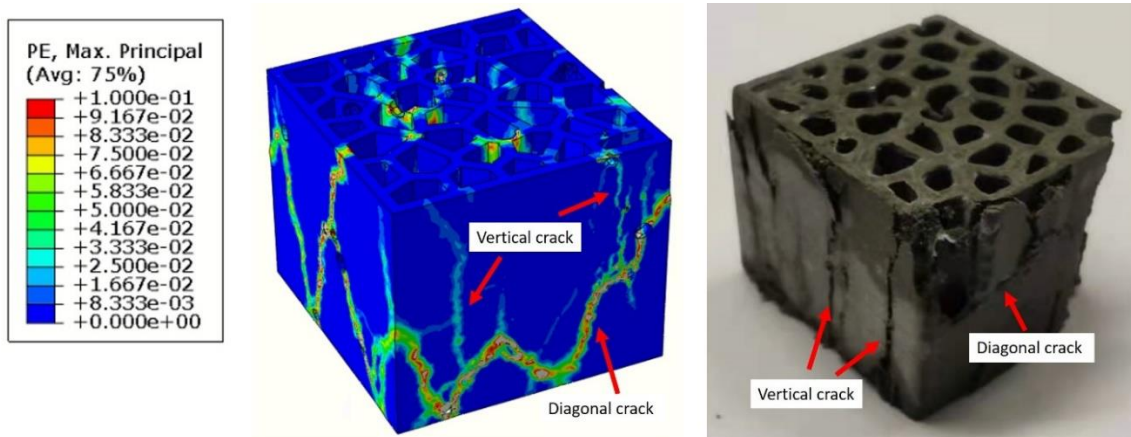
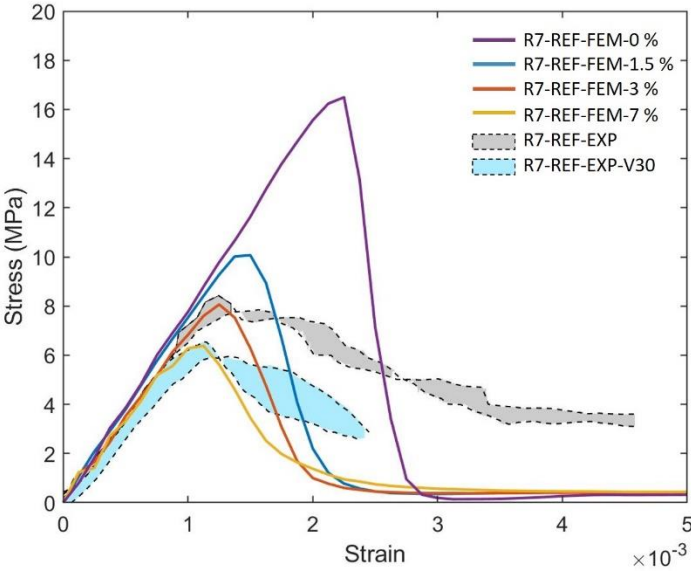
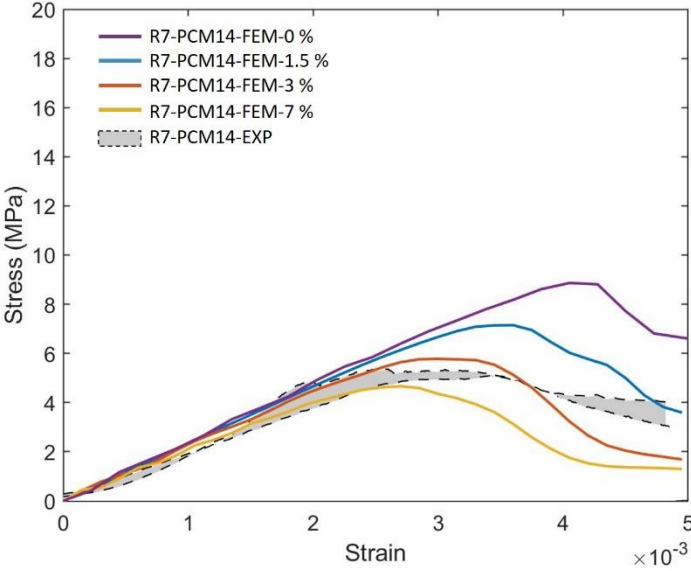


Figure 6-7 Comparison of the crack pattern obtained from simulated and experimental tested specimen, obtained from R7-PCM14

Therefore, in terms of the compression damage process of the LCCCs, the presence of air voids might be a decisive factor. In order to elaborate the influence of air voids on the compressive stress-strain response of the LCCCs, R7-REF with different air void fraction (by volume) was simulated and taken as an example. As can be seen in Figure 6-8 the presence of air voids significantly decreased the compressive strength of R7-REF. In the simulated case with no air voids (R7-REF-FEM-0%) the compressive peak stress is substantially much higher than the experimental results (hatched area marked as R7-REF-EXP). However, by increasing the air void fraction by only 1.5% percent, comparatively the simulated peak stress immediately decreased to around 10 MPa which is 37% lower than the case with no air voids. When increasing the air void fraction to 3% the simulated curve (R7-REF-FEM-3%) has the best agreement with experiments within all used air void fraction values. Similar effect of the air voids on the compressive stress-strain curves can be also found on the PCM14 specimens. It is obvious that the peak stress of the R7-PCM14 is affected by the air content and within all simulated curves specimen with 3% of air has the best agreement with experiment. Besides the stress-strain curves, the simulated crack pattern also show good agreement with experiments (see Figure 6-7 as an example). Conventionally, for cementitious materials diagonal cracks can be witnessed on the compressive fractured cubic sample due to the shear failure process. Comparatively, for the tested LCCCs in this study, diagonal cracks can be also observed indicating shear fracture of the LCCCs under compression. Besides the diagonal cracks, due to the presence of air voids as well as the sharp corners along the pores of the cellular structure, vertical cracks can be also identified on the fractured specimen. Still, a discrepancy can be found at post peak branch between the experimental results and the simulated curve: the experimental results show higher toughness comparing to the simulated curve. According to the principles of concrete fracture mechanics [12], a possible reason might be that the friction between the loading plate still affects the post peak part of the stress-strain curve even plastic films were used in the experiment in the out-of-plane condition. Increasing the friction coefficient (FC) from 0.15 to 1.0, the area below stress-strain curves of the R7 specimen substantially increased without significantly changing the peak stress (see Figure 6-9). Still, the softening branch of experimental stress-strain curves have larger area. Another possible reason might be the introduced air voids did not completely cover the air size distribution in the experiment: smaller air voids are able to induce local fracture which generate more distributed cracks making the experimental LCCCs show “softer” behaviour in the post peak branch.



(a)



(b)

Figure 6-8 Comparison between experiment results and simulated results of (a) R7-REF specimens with different air content and vibration time, (b) R7-PCM14 specimens with different air content

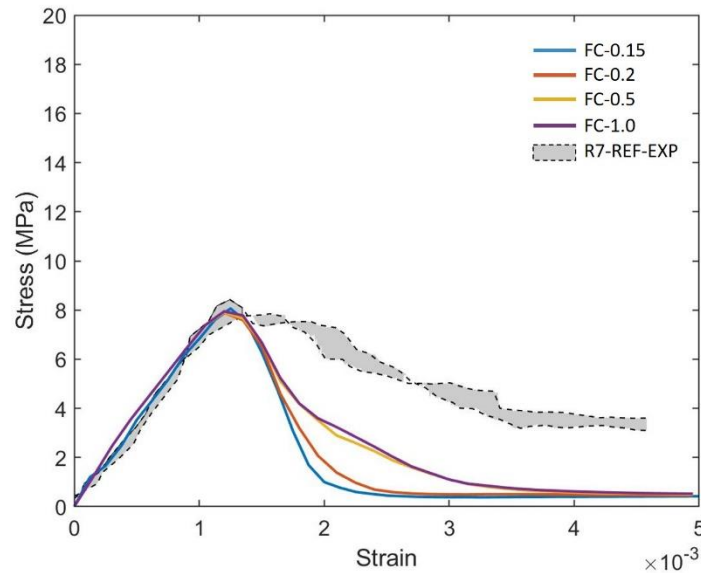


Figure 6-9 Comparison of stress-strain curves of R7-REF-3% with different friction coefficient (FC)

On the other hand, during the experiment, the specimen fabricated by mixture with 30s vibration time (R7-REF-EXP-V30) and mixture with 60s vibration time (R7-REF-EXP) were control groups, aiming to investigate the effect of vibration time on the compressive strength of the specimen. It can be witnessed from Figure 6-8 (a) that the peak stress of specimen with 30s vibration time has dropped to around 6MPa, lower than the 60s vibrated specimen. The possible reason is that the vibration time influence the amount of air bubbles maintained in the mixture. Based on the previous research, vibration is very effective expelling air from fresh cementitious mixture[102]. However, to what extent the vibration time influencing the air void volume as well as the air void distribution is not clear, the CT technology is one of the effective method for providing the air bubble dispersion information in the microstructure of the specimen and can be used in the future investigation.

It was previously observed that both for REF and PCM14, specimens with higher air content have lower compressive strength. While contradictory to experimental observations, assuming with the same fraction of introduced air content (3 %), the simulated peak stress values of the LCCCs are almost the same (shown in Figure 6-10). Considering the compressive strength is rather sensitive to air content, this indicates that entrapment of air bubbles more easily arises in the cellular specimens with higher randomness due to their more complex structures. What should be noticed is that, in the simulations where the friction coefficient was slightly increased to 0.15, the peak stress of the simulated curves is higher than that in the frictionless condition due to the increased confinement. As a result, the actual air content of the specimen is slightly lower than the introduced value. Therefore, the actual air content of the tested LCCCs should be within a range from 1.5% to 3% by volume of the entire cubic domain, or around 0.75% to 1.5% by volume of the LCCCs specimens.

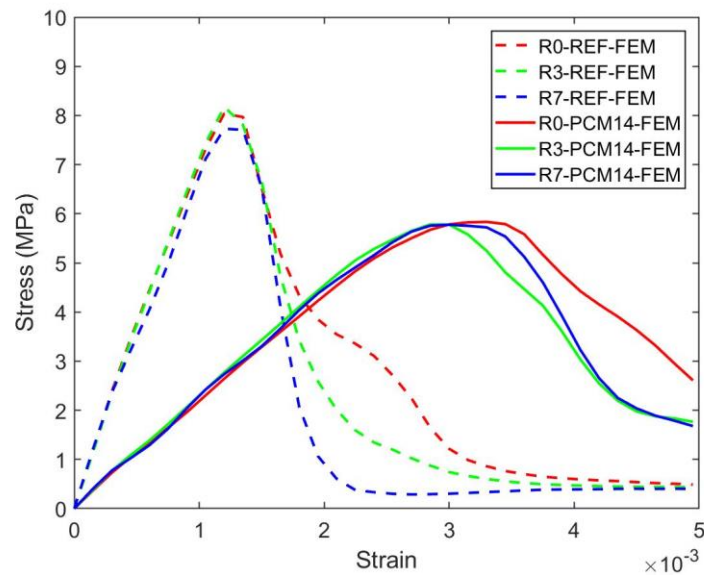


Figure 6-10 Simulated stress-strain curves of the LCCCs, 3% of air content are used for simulation

6.2 In-plane compressive behaviour

In general, as plotted in Figure 6-11 incremental stress drops can be identified from the stress-strain curves of the LCCCs indicating that the LCCCs cracked layer by layer because of the pore structure. In detail, at first an elastic regime can still be witnessed before the first peak stress. As mentioned previously, the slope until $0.2\sigma_{\text{peak}}$ of the stress-strain curve obtained from the cube specimens is regarded as the material E-modulus and the slope until $0.2\sigma_{\text{peak}}$ of the stress-strain curve obtained from the LCCCs is regarded as their stiffness. It is notable in Figure 6-12 that the in-plane stiffness of the LCCCs decreases dramatically with respect to the material cube E-modulus as well as the out-of-plane stiffness. Comparing to the out-of-plane direction, the stiffness of the LCCCs on the in-plane direction is strikingly lower: even normalized by the porosity, the in-plane relative stiffness of the LCCCs is still much lower than the corresponding material E-modulus. For REF specimens, the stiffness of the LCCCs have only 34.4 %, 36.4% and 30.6% of the REF material E-modulus, respectively; for PCM14 specimens, the stiffness of the LCCCs have only 38.4%, 37.6% and 38.2% of the PCM14 E-modulus. Similar to the trend found in the out-of-plane direction, the stiffness reduction with respect to the material E-modulus of the mPCMs incorporated mortar is lower than the reference in the in-plane direction.

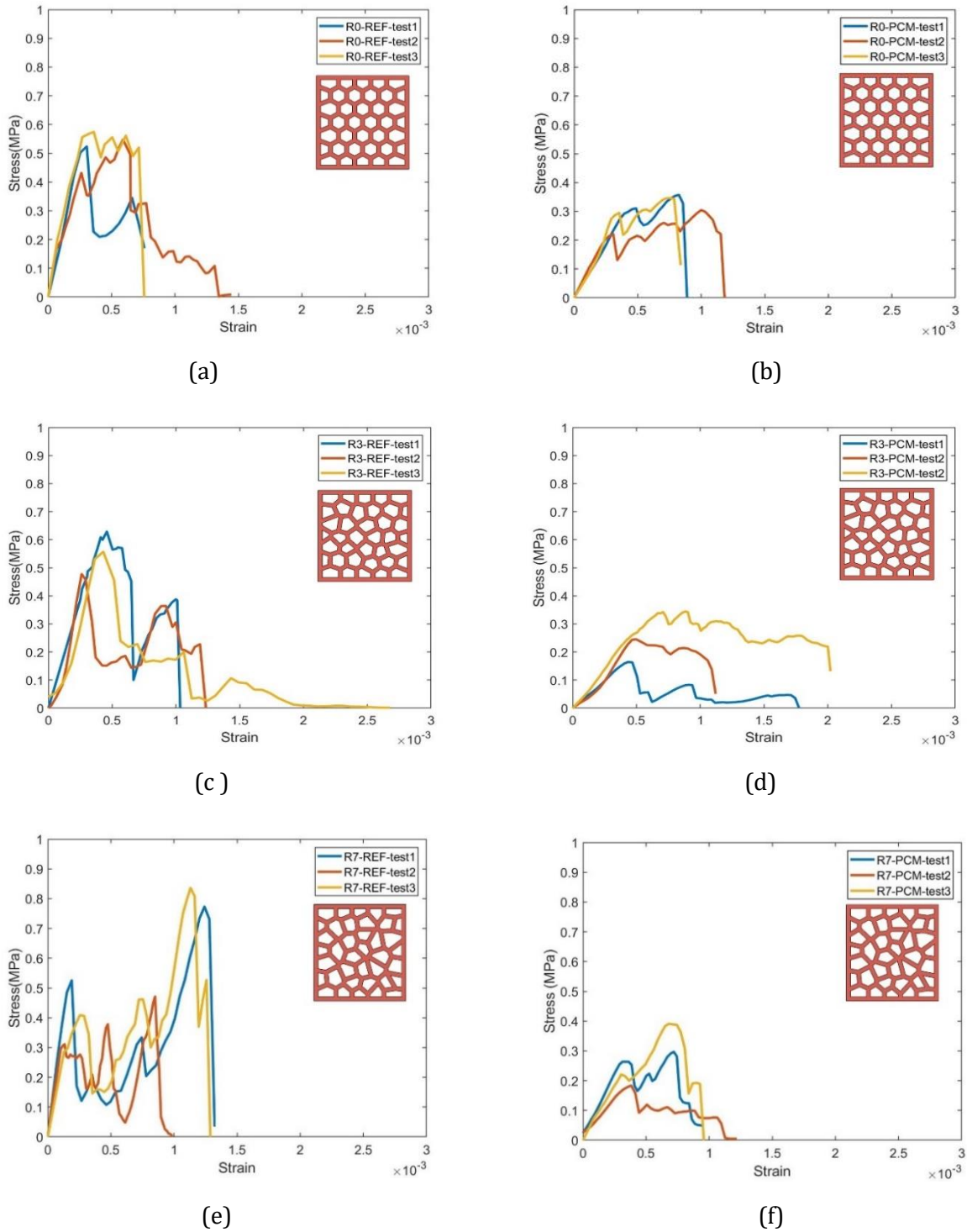


Figure 6-11 The in-plane compressive stress-strain curves of (a) R0-REF, (b) R0-PCM14, (c) R3-REF, (d) R3-PCM14, (e) R7-REF, (f) R7-PCM14, all curves are measured from H40 specimens

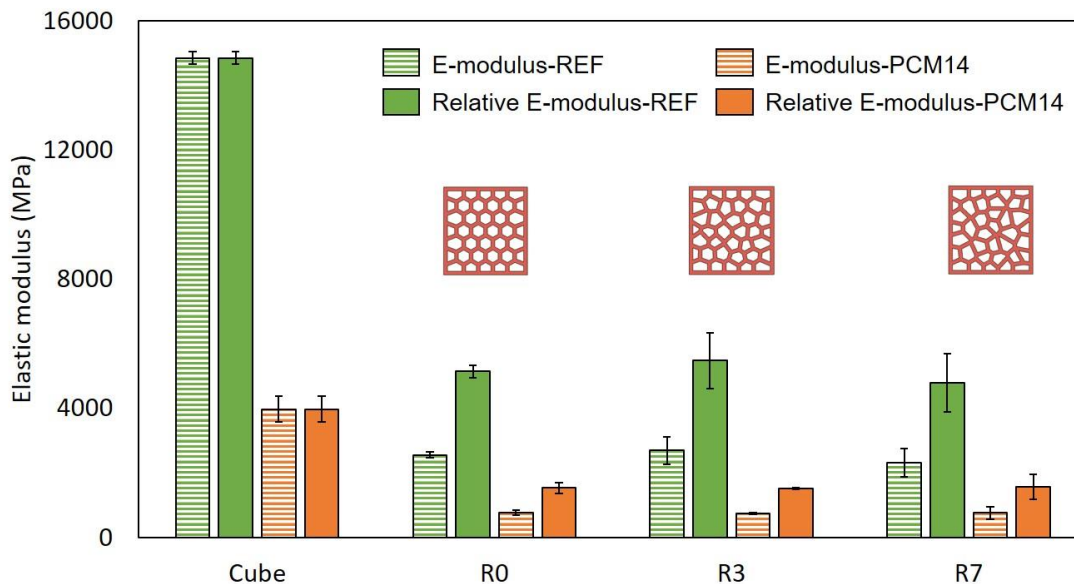


Figure 6-12 In-plane E-modulus of the LCCCs, measure from H40 specimen

After the elastic regime, multiple peaks can be witnessed, the maximum peak load is regarded as the in-plane compressive strength of the LCCCs. It can be seen in Figure 6-13 the in-plane compressive strength of all LCCCs is less than 1MPa which is only around 10% of the compressive strength in the out-of-plane direction. One possible reason of the dramatical strength drop is that when the specimen loaded from the in-plane direction, the occurrence of tensile stress on the plate elements governed the damage process of the LCCCs due to the cellular structure. This is elaborated later by simulation results. As shown in Figure 6-14, when loaded from the in-plane direction, within the elastic regime the sharp corner of the cellular structure induces high tensile stress concentration. It was explained previously, tensile strength of cementitious is significantly lower than their compressive strength. As a result, cracks may generate and propagate from these locations on the plate element of the LCCCs with high tensile stress concentration. After initiating, cracks propagate from one element to another thus multiple drops can be witnessed on the stress-strain curves. Eventually the cracks on each single element form a cracking plane through the cellular structure leading to the failure of the specimen. As can be seen in Figure 6-15, cracks distribute on the plate elements of the LCCCs which indicates the element-wise failure process and thus multiple drops on the stress-strain curves can be found.

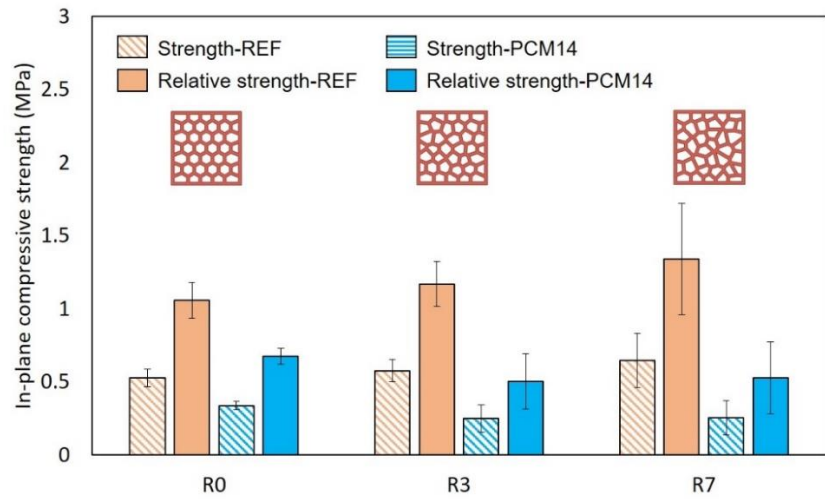


Figure 6-13 In-plane compressive strength of the LCCCs

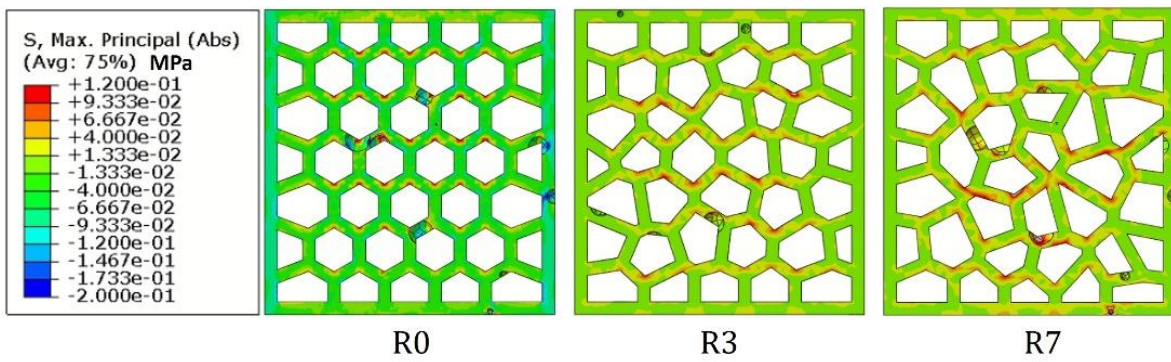


Figure 6-14 Stress distribution of the LCCCs within the elastic regime

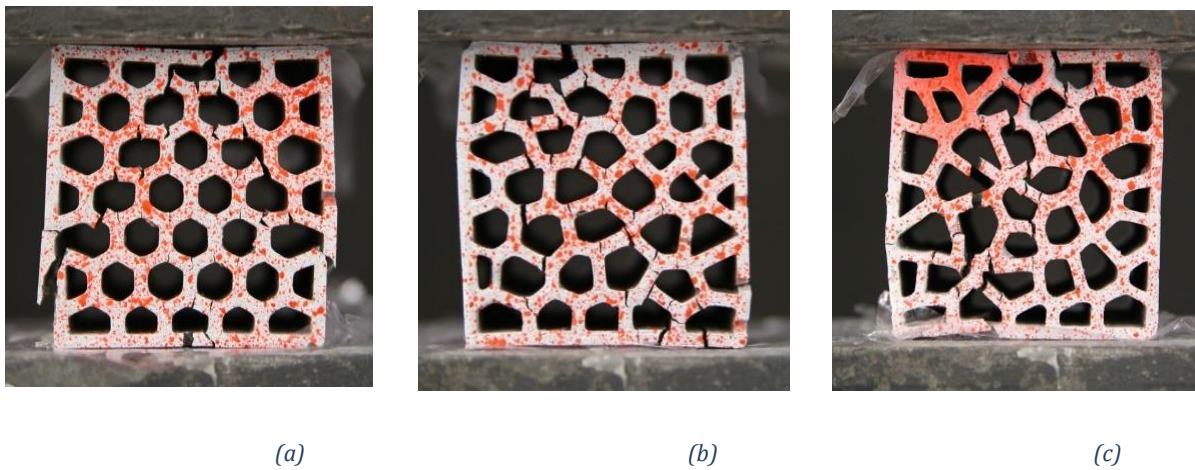


Figure 6-15 Crack pattern of the LCCCs, a) R0, b) R3 and c) R7, LCCCs-REF

Similar to the out-of-plane direction, the influence of air voids is also studied by comparing the experimental results and numerical simulations, for consistency H20-R7 specimens is taken as an example. It is shown in Figure 6-16 that for both types LCCCs made REF and PCM14, introducing air voids also decreases the in-plane peak stress while the negative effect is much more moderate comparing to the out-of-plane direction. This can be explained by the tensile stress distribution on the plate elements of the LCCCs. It was already shown in Figure 6-14, the sharp corner of the cellular structure already induces high tensile stress concentration when the specimen was loaded from the in-plane direction. Even without air voids, the sharp corners already contribute as critical part on the specimens as a result, the influence of air voids is mitigated. The multiple drops in the stress-strain curves also indicate that the step-wisely, damage process of the cellular structure due to the crack propagation between the elements. The crack pattern obtained from experiment and simulation is shown in Figure 6-17, cracks are indicated by high strain region. As can be seen from the figure, cracks distribute on the plate elements of the Voronoi structure which corresponds to the multiple drops observed from the stress-strain curves.

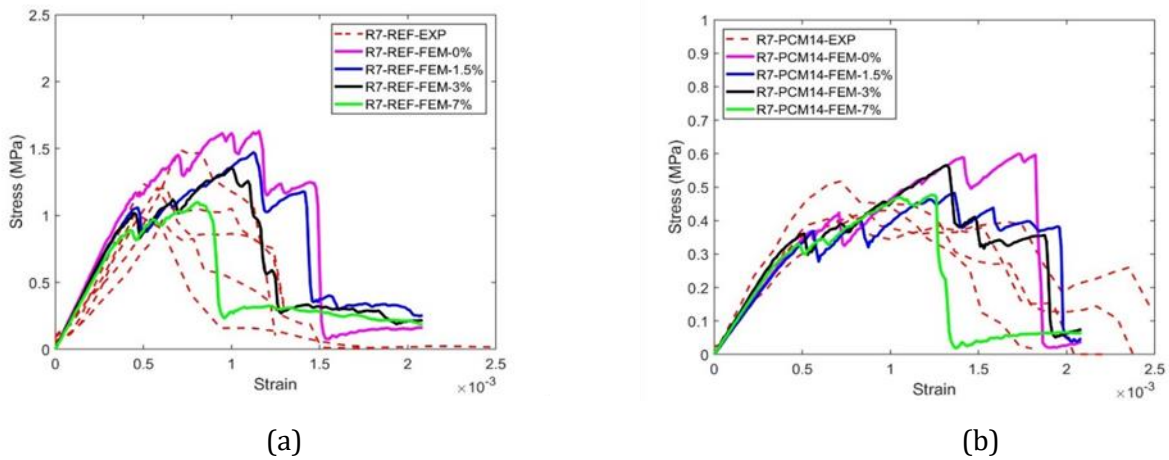


Figure 6-16 In-plane stress-strain curves of a) R7-REF and b) R7-PCM14, note that the y-axes of two figures are different

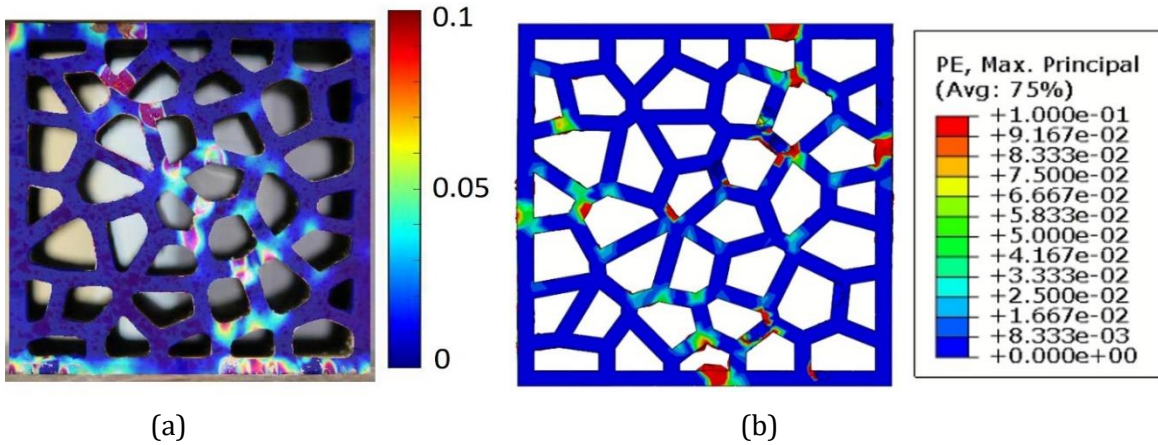


Figure 6-17 Comparison of crack pattern obtained from (a) experiment and (b) simulation

7

Thermal properties

This chapter discusses the relationship between the geometry randomness, porosity of LCCCs specimen to the thermal conductivity based on both numerical analysis and analytical analysis results. Furthermore, the effect of convection, radiation on determining the thermal performance of LCCCs are investigated by comparing the results from the situation in which only conduction is considered. The ANSYS simulation results are compared with Abaqus simulation results for validifying the steady state heat transfer analysis. In the end, the effect of incorporating mPCMs in the cementitious mortar on the reduction of LCCCs specimens' thermal conductivity as well as the limitation of current thermal analysis is elaborated.

7.1 Relationship between thermal conductivity and geometry randomness

Since the Abaqus simulation is based on steady state heat analysis and the boundary condition is consistent between R0, R3 and R7 group, the temperature distribution on the y direction which is the main heat transfer direction which is a nearly linear transition. The difference between 3 groups is relatively small so the temperature distribution will not be discussed. First of all, when only consider the conduction as the heat transfer mechanism, the simulated thermal conductivity of R0, R3 and R7 specimen is $0.429\text{W/m}\cdot\text{K}$, $0.435\text{W/m}\cdot\text{K}$ and $0.444\text{W/m}\cdot\text{K}$, respectively. Correspondingly the density of R0, R3 and R7 is 999.98 kg/m^3 , 1008.9 kg/m^3 and 1027.6kg/m^3 , respectively (as listed in Table 7-1).

It is seen in Figure 7-2 that based on the data taken from building physics tables and formulas, the thermal conductivity of lightweight and cellular concrete is $0.35\text{ W/m}\cdot\text{K}$ when the density is 1000 kg/m^3 . Although the calculated thermal conductivity of LCCCs is slightly higher than $0.35\text{ W/m}\cdot\text{K}$, as the LCCCs possess high porosity, it is predicted as a promising alternative of the lightweight concrete for fulfilling the role of thermal insulation. Meanwhile, by collecting the thermal conductivity tested based on different principles and technologies [14], It is seen in the Figure 7-1 that at similar density, the thermal conductivity of R0, R3 and R7 LCCCs are comparable with that of foam concrete.

As mentioned in section 5.4, the thermal conductivity of LCCCs is calculated from the average heat flux. According to Figure 7-3, the heat flux distribution in the cross sections of R0, R3 and R7 on the y direction is can be observed: due to the heat transfers direction through the specimen is vertical, those horizontally orientated cell walls have lower heat flux flow comparing to the vertical orientated ones. When the randomness of geometry increases, the cell distribution becomes more arbitrary, more cell walls are orientated horizontally (for instance, the black circles on R7 heat flux graphic indicates that there are more blue area occurring on the x direction cell walls).

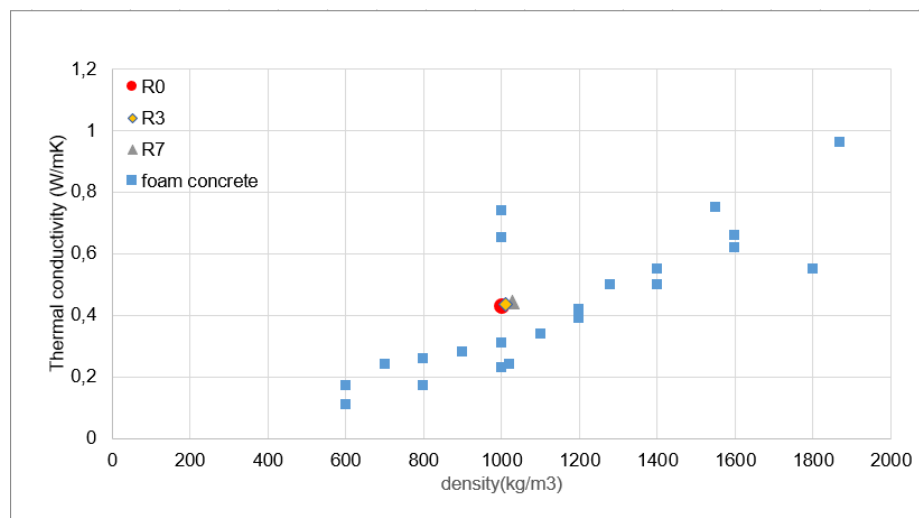


Figure 7-1 Comparison of thermal conductivity between LCCCs and foam concrete, the value of foam concrete were taken from [14]

Table 7-1 The thermal conductivity and density of LCCCs made by REF

Materials	λ (W/m·K)	ρ (kg/m ³)
LCCCs (REF R0)	0,429	999,98
LCCCs (REF R3)	0,435	1008,93
LCCCs (REF R7)	0,444	1027,64

Density ρ , heat conduction coefficient λ , specific heat c and vapour diffusion resistance figure μ of building materials

Material type	ρ (kg/m ³)	λ (W/m · K)		c (J/kg · K)	μ –
		I *)	II *)		
Lightweight concrete	1900	0.95	1.4	840	130
	1600	0.70	1.2		80
	1300	0.45	0.8		75
	1000	0.35	0.5		65
	700	0.23			55
	500	0.17			45
	300	0.12			35
Cellular concrete	200	0.08		28	
	1300	0.50	1.2	7.5–9	
	1000	0.35	0.7	5.5–7.5	
	700	0.23		4.5–7.5	
	400	0.17		3–7.5	

Figure 7-2 The thermal-physical properties of Lightweight concrete and Cellular concrete taken from building physics tables and formulas*

However, the calculated thermal conductivity of 3 groups of specimen reflects the difference between total heat flux of R0, R3 and R7 LCCCs is actually very small. Seemingly, the geometry randomness of the cellular structure has no contribution on benefiting the thermal insulation capacity. Nevertheless, it is also observed that no matter how different the heat transfer in the interior cellular structure of specimen, the number of thermal bridges which connects the interior structure to the outer surface (the parts highlighted by black dash line rectangular in Figure 7-3) is constant among three groups. This might be the potential reason explaining why the thermal conductivity of R0, R3, R7 is similar.

*the details of building physics tables and formulas can be checked from https://website.thiememeulenhoff.nl/binaries/content/assets/standaardsites/hbo-bouwkunde/building-physics/9006951554_insteekatern_pms.pdf

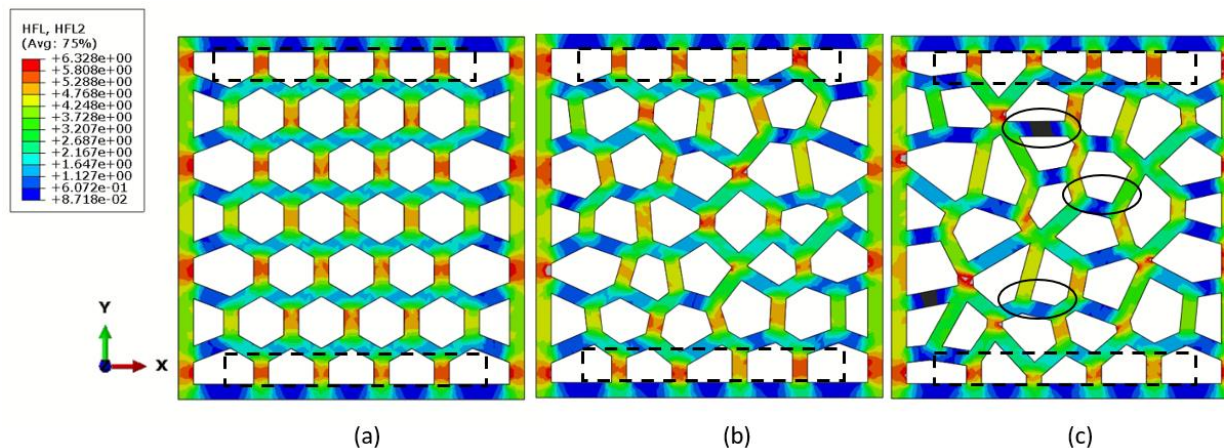


Figure 7-3 The graphic of heat flux on y direction (a) R0 (b)R3(c)R7, black circles indicate the blue area of x direction cell wall, black dash line rectangular indicates the thermal bridge connecting inner structure to outer surface

A thermal bridge is defined as an area of the objects which has higher thermal conductivity, providing the path for heat transfer. Mao et al [103] studied the effect of thermal bridges on the effective thermal conductivity of vacuum insulation panel and stated that heat losses can be reduced sharply by eliminating the effect of thermal bridge.

Restricted by the requirement of designing cubic specimen meanwhile maintain the integrity of the Voronoi cells, the margin cells (marked by black dashed lines in Figure 7-3) need to be somehow regulated such that the influence of randomness was potentially eliminated. To investigate the real effect of the randomness in the interior cellular structure of different groups of specimens, the middle section of R3 and R7 specimen has been cut along the z direction and the heat flux on this cross section is studied (shown in Figure 7-4). The average heat flux on the middle section has been calculated respectively under the same boundary condition (the 100 °C as the hot temperature and 20 °C as the cooler temperature). Table 7-2 lists the y-direction heat flux on middle section of R3 and R7 specimen is 4.64 W/m² and 3.83 W/m². Higher randomness apparently deduces lower heat flux. As seen in the Figure 7-4 , the cross-sectional area of R7 specimen is bigger than that of R3 specimen, indicating more heat flow is dissipated towards x direction, therefore the y-direction heat flux of R7 specimen is smaller than that of R3 specimen on the middle section, consequently proving the effect of geometry randomness on the ability of conducting heat flux.

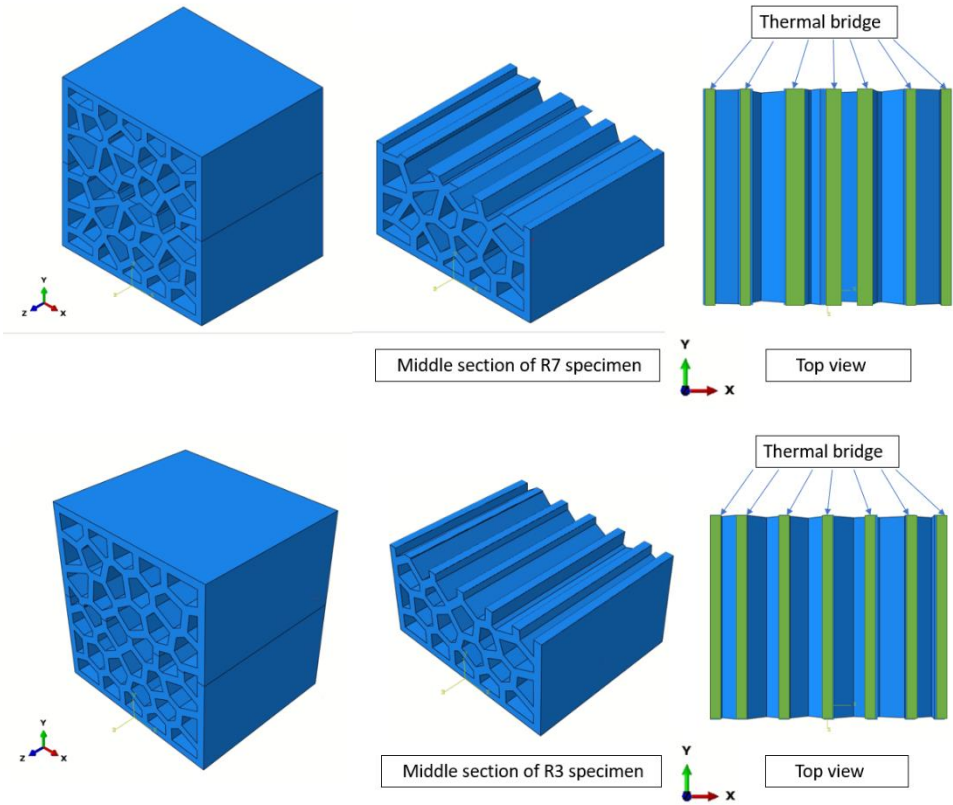


Figure 7-4 The graphic of thermal bridge at the middle section of R3 and R7 specimen

Table 7-2 The y-direction heat flux on middle section of R3 and R7 LCCCs

Name of group	y-direction heat flux on middle section(W/m ²)
R3	4.64
R7	3.83

7.2 Relationship between the thermal conductivity and porosity

It is well known the thermal conductivity of the cellular composites highly depends on its porosity. There are four empirical equations proposed based on different models to reveal the relationship between thermal conductivity and porosity: the weighted average or linear equation (eq. (8)); the weighted harmonic average equation (eq. (9)) ; the geometrical average equation (eq. (10)) and Maxwell's equation (eq. (11)) [104]. The numerical simulation results will be compared with empirical equation results for getting better insight of the relationship between thermal conductivity and porosity in these two points of view.

Four equations are listed below

The weighted average or linear equation:

$$k = \phi k_a + (1 - \phi)k_c \quad (8)$$

The weighted harmonic average equation:

$$\frac{1}{k} = \frac{1}{\phi k_a} + \frac{1}{(1 - \phi)k_c} \quad (9)$$

The geometrical average equation:

$$\frac{1}{k} = \frac{1}{\phi k_a} + \frac{1}{(1 - \phi)k_c} \quad (10)$$

Maxwell's equation:

$$k = k_c \frac{(2r + 1) - 2\phi(r - 1)}{(2r + 1) + \phi(r - 1)} \quad (11)$$

With:

$$r = \frac{k_c}{k_a}$$

In these equations, k is the effective thermal conductivity of the specimen ($\text{W/m}\cdot\text{K}$), k_c is the thermal conductivity of REF cement which is $1.327 \text{ W/m}\cdot\text{K}$, k_a is the thermal conductivity of air which is $0.026 \text{ W/m}\cdot\text{K}$, ϕ is porosity which is calculated from the volume of air cells divided by the total volume of LCCCs.

The thermal conductivity results from weighted average or linear equation, Maxwell's equation and the geometrical average equation have been plotted in Figure 7-5, comparing with numerical results. The results calculated from weighted harmonic average equation will not be discussed since its result deviates away a lot from other results. Although the effect of geometry randomness on the thermal conductivity is not very clear (in this case, the porosity of three groups specimen is similar as well), it can be seen that the relationship is linear and there's a slight decrease of thermal conductivity when the Voronoi pattern becomes more regular. The simulation result line is parallel to all equation lines and close to the Maxwell's line.

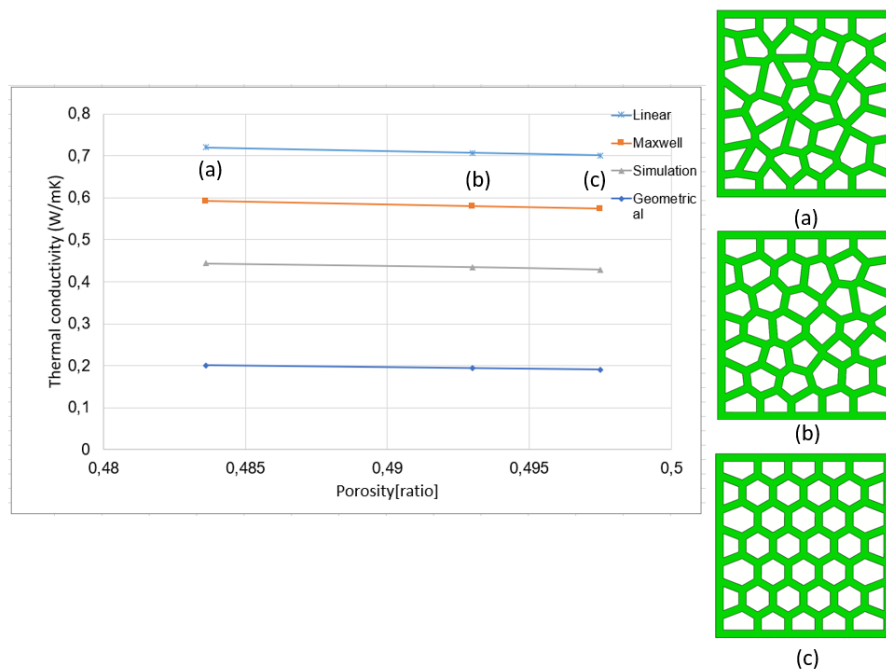


Figure 7-5 Thermal conductivity of LCCCs with various geometry randomness, calculated from empirical equations and numerical simulation (a)R7 (b)R3 (C) R0

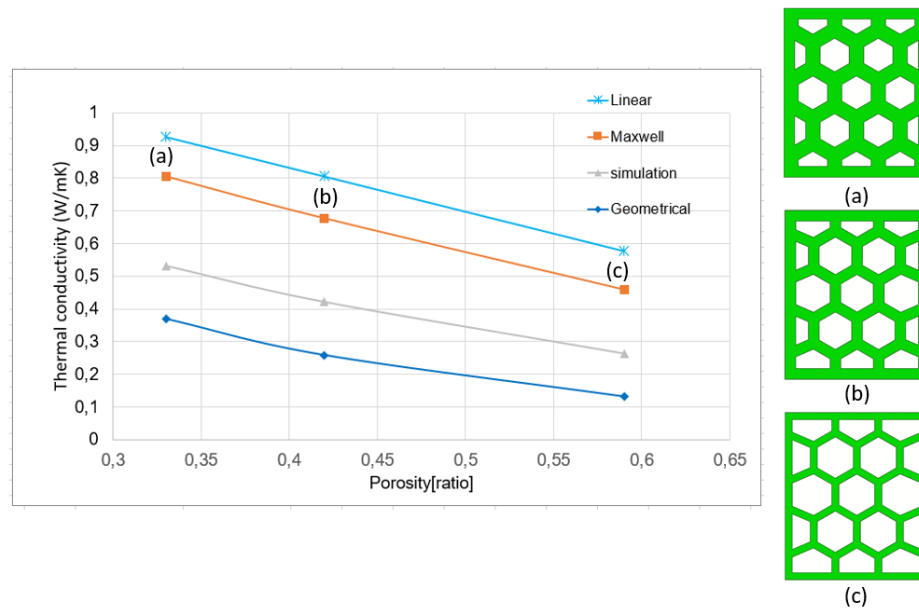


Figure 7-6 The thermal conductivity of R0 LCCCs with various porosity. (a) R0 LCCCs with cell wall thickness equals to 4mm (b) R0 LCCCs with cell wall thickness equals to 3mm (c) R0 LCCCs with cell wall thickness equals to 2mm

The positive effect of increasing the porosity on reducing the thermal conductivity of LCCCs can be observed in Figure 7-6. The porosity was modified by means of changing the cell wall thickness from 2mm to 4mm, leading to the porosity decreases from 0.59 to 0.33. The simulation results reveal the relationship is not completely linear which is slightly different from the linear equation results and Maxwell equation results. The simulation line is similar with and close to the geometrical average equation line.

In section 7.1 the effect of thermal bridge on the heat flux and thermal conductivity of the specimen has been discussed. Inspired from the assumption that thermal bridge will influence the heat transfer process, another design was generated which possess same porosity with the R0D4 which is R0 LCCCs with cell wall thickness equals to 4mm. It is seen in Figure 7-7 (a), the interior structure of the new design is not attached to the upper and lower cell wall in y direction (the two connections are provided on x direction). Under the same boundary condition, the heat flux on the y direction is dramatically decreased due to the “broken” thermal bridge. On the other hand, considering R0D4 as the reference, when reducing the cell wall thickness to 3mm (namely R0D3 in Figure 7-8), porosity has increased 27% while the corresponding thermal conductivity has decreased 21%, however when eliminating the effect of thermal bridge in the y direction, the corresponding thermal conductivity has decreased 45%, which indicates the significant effect of thermal bridge on thermal conductivity of LCCCs.

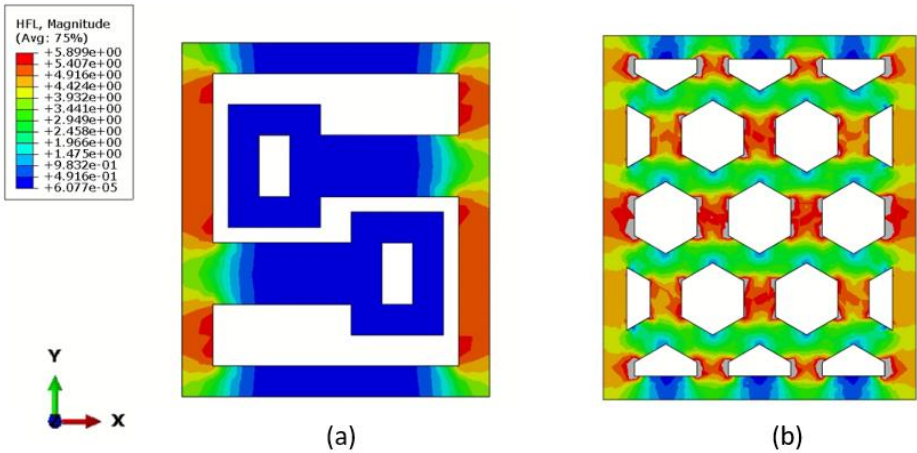


Figure 7-7 The comparison of heat flux between two R0 LCCCs with cell wall thickness equals to 4mm (a) without thermal bridge (b) the R0D4 with thermal bridge, the porosity of two models is same.

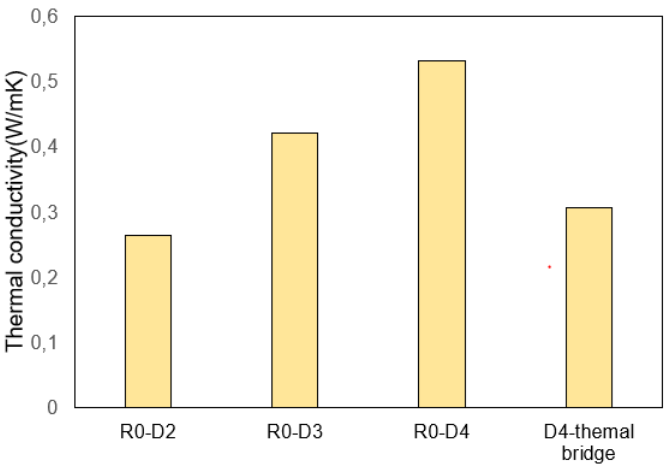


Figure 7-8 The comparison of thermal conductivity between R0 specimens with various porosity and the new design which eliminate the thermal bridge on the y direction.

7.3 The effect of convection and radiation on the thermal conductivity

As described in section 5.4, the conduction, convection, and radiation are considered in the thermal performance analysis in Abaqus. The conduction occurs through the solid cell wall in the specimen. Convection and radiation occur through the inner pores, the former process occurs as the air flow from the region of higher temperature to the lower temperature and the latter process depends on the material emissivity coefficient and the temperature variation of the inner cell wall. The convection of inner cavities was considered by applying surface film coefficient and the sink temperature.

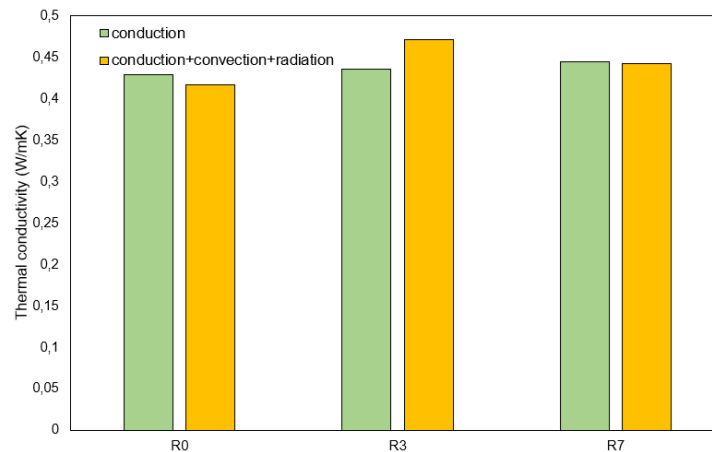


Figure 7-9 The comparison of thermal conductivity between only considering the effect of conduction and considering the effect of conduction, convection and radiation

It is shown in Figure 7-9 that there is less notable difference between the thermal conductivity calculated from only considering the effect of conduction and considering the effect of conduction, convection and radiation. Due to the temperature difference between the air in the unit cell and its surrounding cementitious cell wall is very small, the heat exchange due to the convection is limited, on the other hand, since the radiation is proportionally related to T^4 , the temperature settings in the simulation is too small to generate the significant effect.

In Abaqus, the convection is simplified as film condition, which differs from realistic heat transfer process and the simulation results might deviate from the situation in which natural convection is present. In the following part, the influence of natural convection in the unit cells of LCCCs on the y direction will be discussed by analysing the ANSYS simulation results, therefore validating the accuracy of the simplified steady state heat transfer model.

The ANSYS simulation is based on transient heat analysis air density change due to temperature variation was taken into consideration thus air flow was explicitly simulated. CFD posts are used to display the air flow velocity and temperature contour of the natural convection. As shown in Figure 7-10 the y-direction velocity magnitude of air in the inner cavity is around 6.02×10^{-6} m/s, the maximum value is around 1.15×10^{-4} m/s, which is very slow indicating that the air flow in the pores of the LCCCs had minor influence on the heat transfer process. The comparison between simulated thermal conductivity considering natural convection using ANSYS and using the simplified film condition in

Abaqus are demonstrated in Figure 7-11 the difference between the two results is less than 10%. The potential reason for the deviation is the inaccuracy of sink temperature value in each cell in Abaqus, although the general temperature distribution is linear, the exist of temperature deviation between the adjacent cavities may lead to the deviation of overall thermal conductivity. In ANSYS, the calculation of the thermal conductivity is based on more realistic transient temperature in each cell. In general, the effect of convection and radiation on thermal conductivity of LCCCs is limited and neglectable.

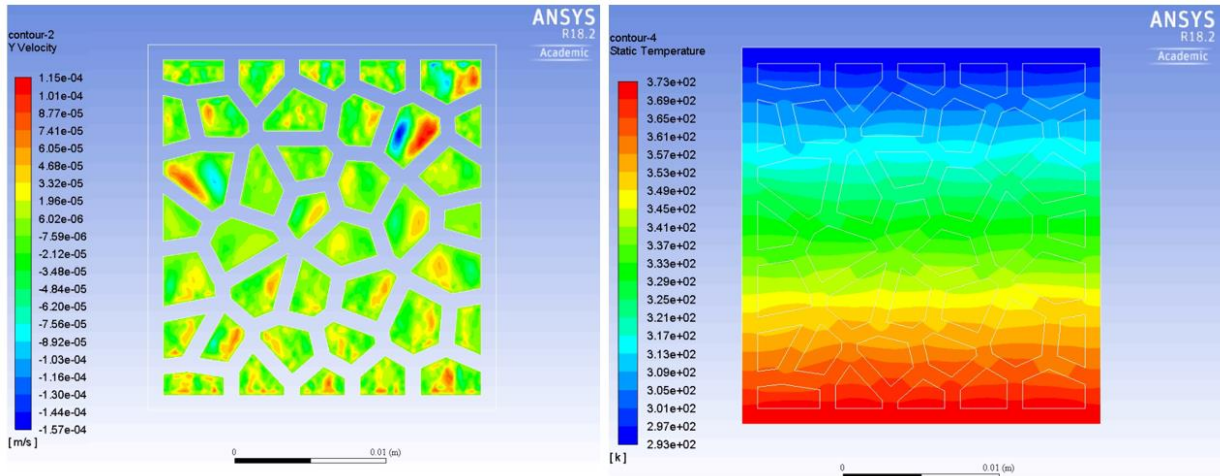


Figure 7-10 Left: the air flow velocity in the cells of R7 LCCCs Right: the temperature distribution on the y direction

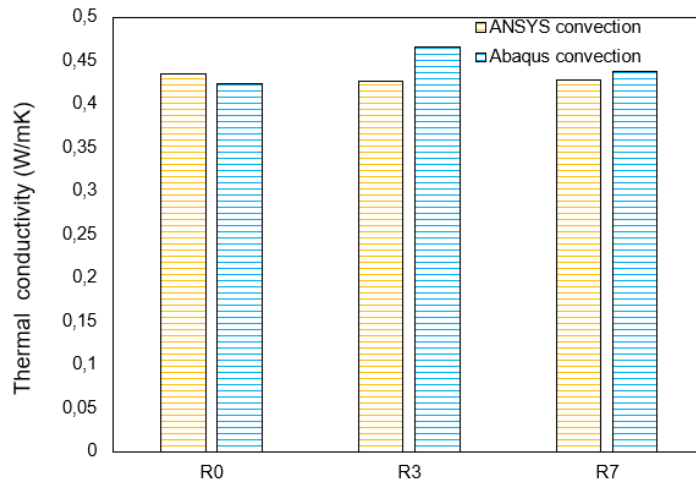


Figure 7-11 The comparison of thermal conductivity considering both conduction and convection between using ANSYS and Abaqus software

7.4 The effect of mPCM on thermal conductivity

By comparing the thermal conductivity between LCCCs made from REF mortar and PCM incorporated mortar, it is found that the thermal conductivity of R0, R3, and R7 LCCCs has decreased 18.2%, 18.6% and 18.9% respectively after using the modified mortar incorporated with 14.4% volume of mPCM particles as the base material (see Figure 7-12 and Table 7-3).

Some explanation might be used for elucidating the result. Firstly, the introduction of mPCMs lead to an increase of porosity and considering the microstructure of cementitious material. Since the plastic shell of the mPCMs particles is chemically stable and inactive in the alkaline environment, therefore the incorporated mPCMs is assimilate to the entrained air bobbles in the cement paste. In section 7.2 it is discussed that porosity plays an important role on effecting the thermal conductivity of specimen. However, to what extent it affects the thermal properties of LCCCs is unclear in this study. On the other hand, because the shell material of mPCMs is polymer which has lower thermal conductivity comparing to cementitious matrix thus the mPCMs incorporated constituent mixture also shows lower thermal conductivity.

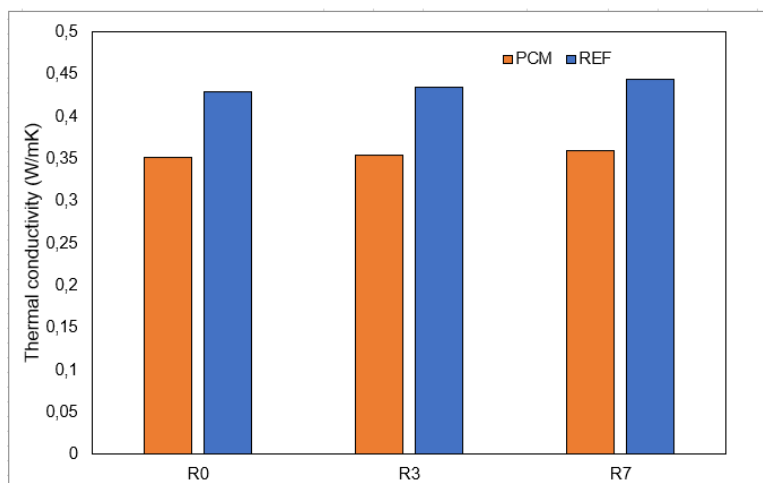


Figure 7-12 The comparison of thermal conductivity between LCCCs made from REF mortar and PCM modified mortar

Table 7-3 The thermal conductivity and density of LCCCs made by REF and PCMs14 mixtures

Materials	λ (W/m·K)	ρ (kg/m ³)
LCCCs (REF R0)	0,429	999,98
LCCCs (REF R3)	0,435	1008,93
LCCCs (REF R7)	0,444	1027,64
LCCCs (PCMs14 R0)	0,351	898,97
LCCCs (PCMs14 R3)	0,354	907,02
LCCCs (PCMs14 R7)	0,36	923,84

To further elaborate the mechanism, mercury intrusion porosimetry (MIP) might be a useful method for measuring the porosity and pore diameter of the mPCMs incorporated mortar. The computed tomography (CT) scan can provide 3D information of heterogeneous material and the pores dispersion information in the microstructure of PCM incorporated cement paste. The mentioned two methods can help to quantitatively explaining the effect of porosity on the reduction of thermal conductivity and worth of investigating in the future.

Although lower thermal conductivity gives the PCM incorporated mortar better insulation property than the reference mortar, in terms of heat storage the low thermal conductivity of PCM incorporated mortar is considered as a drawback of the utilization of PCM incorporated mortar because it may hinder the phase change process when the material is less thermal conductive. thermal storage material. The latent heat attributed to the phase change process wasn't taken into consideration due the limitation of experimental set-up as the test temperature is around 21 °C which is lower than the phase changing temperature. In potential future studies, the phase change process might be taken into consideration by a multi-scale modelling approach: considering the microstructure explicitly introduces PCM spheres in the numerical model; simulate heat transfer process of the constituent material at the microscale; using the simulated microscale results as the material input parameters for simulating the LCCs at the scale implemented in this study.

8

3D printing of LCCCs

An attempt of 3D printing LCCCs specimen has been conducted by utilizing the concrete 3D printer in micro-lab. The mix design of printable concrete incorporated with PCMs and the detailed mixing steps, the general printer information and printing procedure are introduced in this chapter

8.1 Mix design

As mentioned in the subsection 2.3.3, the incorporated PCM has a negative effect on the workability of modified cement paste and increasing amount of water is therewith required for guarantee the suitable workability. In the case of 3D printing of LCCCs, the mix design must be tailored in order to achieve the enough pumpability, extrudability and buildability. The addition of superplasticizer helps to reduce the water/binder ratio and provide desirable workability of printing. The viscosity modifier agent which is made of hydroxypropyl methylcellulose plays the role on modifying the extrudability of the mixture. The specific constituent of LCCCs printing mix design is listed in Table 8-1 .

Table 8-1 LCCCs printing mix design (g/l)

CEMI 42.5N	Fly ash	Sand (125- 250 μ m)	SP	PCMs	Water	Viscosity modifier agent (VA)
456.4	539.4	319.5	1.6	136.9	302.8	0.33

8.2 The general printer information, printing settings and printing procedure

An extrusion-based concrete 3D printer was used for printing a LCCCs brick with similar size to commonly used clay bricks. A brief introduction of the extrusion-based 3D printer is given below.

As seen in Figure 8-1 (a) the multi-material 3D printer uses a gantry system, the metal printer head (see Figure 8-1(b)) is supported on the gantry frame along the X-Y axis as the printer head moves around to print the parts on the print-table. The print-table can move up or downwards along the z axis for satisfying the height requirement. The effective printing size of 3D printer is 480mm(l) \times 480mm(w) \times 500mm(h). The ram extruder(see Figure 8-1(d)) connected with a barrel is mounted on the vertical metal frame which stables the printing process in a high speed , the volume of the barrel is 1.5L. The printing settings is fully control from the computer via WIFI in the real time and it is seen in Figure 8-1 (c) the straightforward operation can be achieve on the touch screen for modifying the printing process.

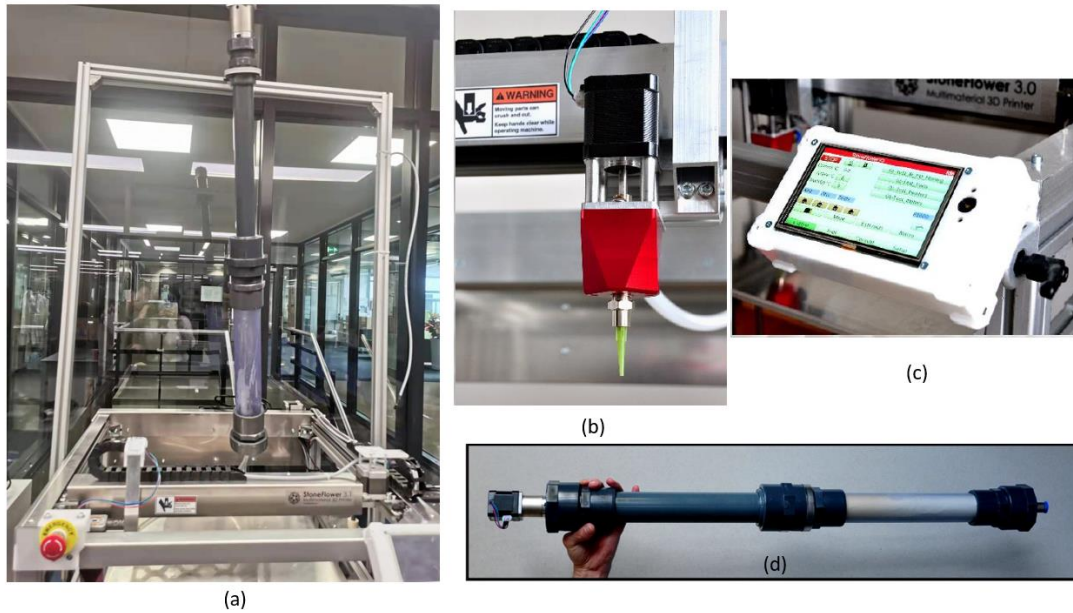


Figure 8-1 (a) The multi-material 3D printer (b) The metal printer head (c) The operation control (d) The ram extruder

The printing settings of the 3D printer play an important role on determining the extrusion process, the quality of the printed filament and the mechanical properties of the printed specimen. As the printing mixture possess high viscosity and is extruded though the plastic hose with 73 mm length and 11 mm diameter, the material extrusion rate should be tested preciously in case the overpressure occurs during the extrusion. In this research, the material extrusion rate is ensured as 0.01 L/min after a couple of pre-tests and keep constant during the printing procedure. On the other hand, the nozzle travel speed is decisive during the overall printing process: the too low of travel speed causes the excess of extruded material resulting in the accumulation of filament at the same spot, the too high of the travel speed leads to the stretch of the printing filament, resulting in the deformation of filament and the irregularity of the printing specimen. The overall printing settings are listed in .

Table 8-2.

Table 8-2 Printing settings

Parameter	Setting	Unit
Nozzle travel speed	6.7	mm/s
Material extrusion rate	0.01	L/min
Nozzle diameter	6	mm
Ram extruder diameter	67.8	mm
Layer height	4	mm
Layer width	8	mm
Hose diameter	11	mm
Hose length	73	mm

8.3 The mixing and printing procedure

Similar with the description given in the section 3.3, the mixing steps of the LCCCs printable mixture are as follows: firstly, the dry material (cement, fly ash and sand) was placed in a Hobart mixer and mixed for 4 minutes; then, the superplasticizer was dropped into the water and then they were added into the mixed dry material within 10 s followed by for 2 minutes mixing at low speed. The mixer was then stopped for 30 s during which all paste adhering to the wall and the bottom part of the bowl was scrapped using a metal scraper, meanwhile the PCM and VA powder was added; After that, the mixture continued for 2 minutes. The total mixing time is 8 minutes. A total volume of 1.2L mixture was prepared for printing the specimen.

Afterwards, the mixture was manually filled into the ram extruder firmly to expel the entrapped air in the cement paste. Then the filled mixture was extruded into the hose using the plunger in the ram extruder to reduce the entrapped air in the printing filament and ensure the printability of the cement paste. Prior to printing, a plastic thin film was covered on the surface of metal build plate for the convenience of specimen detachment after the printing procedure has finished.

The printing path was designed by writing the G-code file. (The printing path is depicted in Figure 8-2). Since the 3D printing is a feasibility test for printing the architected LCCCs, the printing routine was designed as a honeycomb Voronoi shape with 280 mm width, 215 mm length and 40 mm height consisting of 10 layers of printing cementitious filaments. Each layer of cementitious filament is 4 mm high and 8 mm wide. The printing process and the printed specimen is shown in Figure 8-3. The cure of printed specimen takes place for 28 days after the printing. The full text of G-code of the printing specimen can be found in Appendix C.

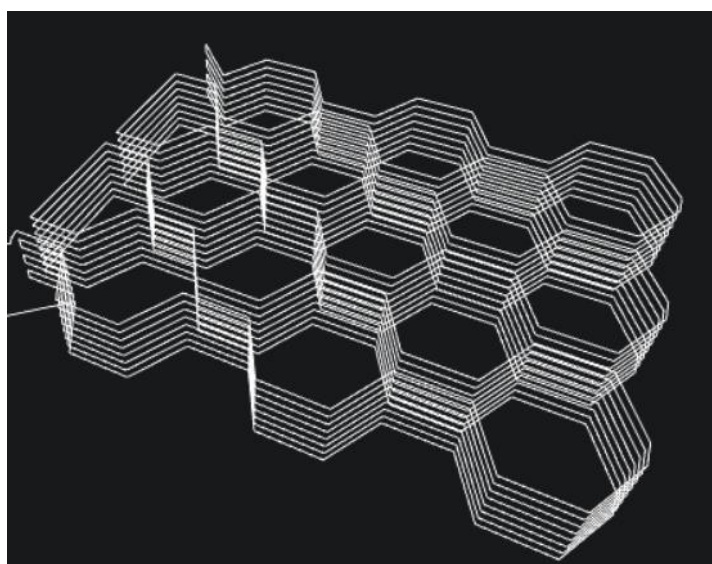


Figure 8-2 the printing path generated by G-code

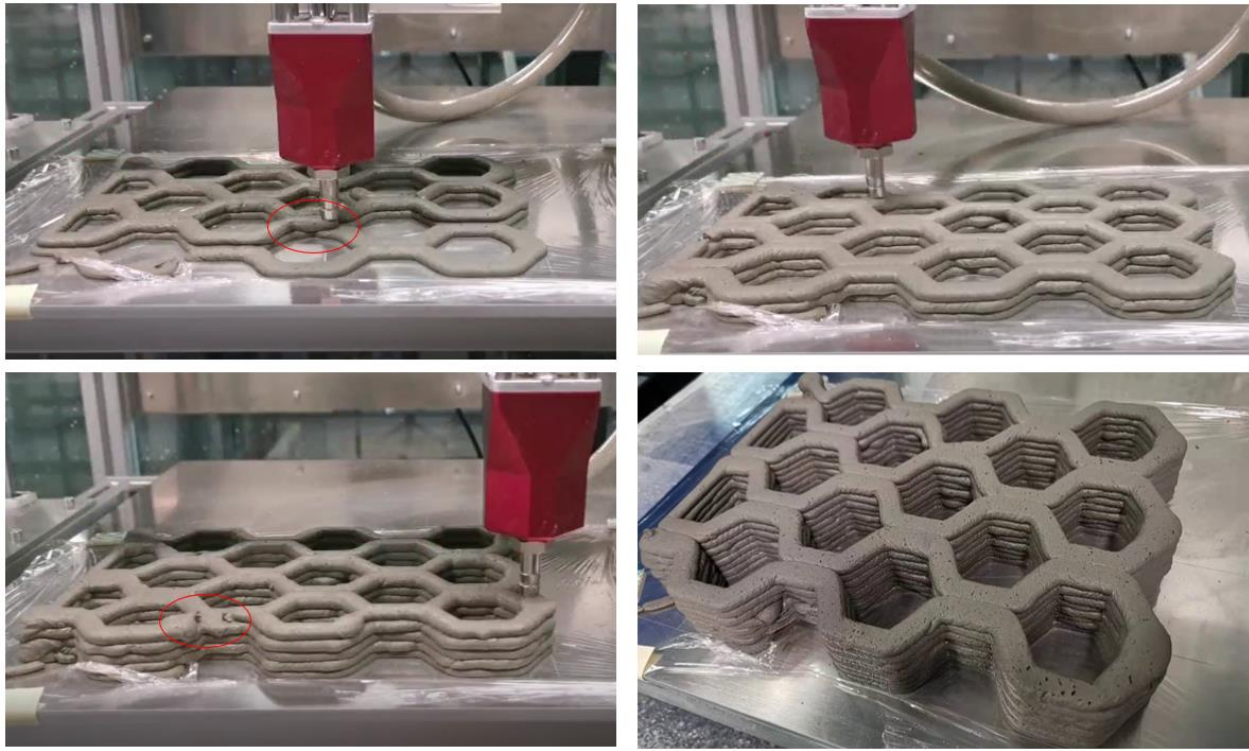


Figure 8-3 The printing process and the printed specimen

During the printing process, the deformation and the discontinuity of the printing filaments have been observed as highlighted in the red circle area of Figure 8-3, resulting from the obstruction of the nozzle by the solids in the mixture or the mixture was jammed in the hose during the extrusion due to the friction between the cement material and the inner surface of hose, which indicates that the extrudability of this designed mixture was not optimized. The extrudability of the printable mixture can be qualitatively evaluated by the Vane test [105]. In the Vane test, the extrudability is characterized by Bingham parameter and other flow properties among different mixtures. The very high yield stress of the printable material makes the extrusion difficult. However, the sufficient yield stress of the printing filament is important for achieving the shape retention which is another factor for measuring the buildability of the printable material. It is shown in the Figure 8-3 that there was a slight deformation of layers under the self-weight. Therefore, the extrudability, flowability and the buildability of the printable cementitious material should be characterized in the further study.

9

Conclusion and recommendations

The main goal of the research is developing architected lightweight cementitious cellular composites (LCCCs) with good mechanical properties for the potential thermal insulation purpose. With the aid of 3D printing technique, LCCCs with Voronoi structures are prepared using a reference mortar and mPCMs incorporated mortar as constituent materials. In this research, compressive behaviour of the LCCCs is investigated by experiments and numerical simulations. On the other hand, the thermal properties of reference mortar and mPCMs incorporated mortar are tested by conducting the TPS method and they are utilized as the input parameters of the numerical simulation for studying the thermal performance of LCCCs.

In this chapter, the conclusion of the compressive behaviour investigation will be present, followed by that of thermal performance study. After finishing that, a general conclusion will be provided. To the end, discussion in terms of this research and recommendations for future investigation will be given in the final part of this chapter.

9.1 The conclusion of compressive behaviour of LCCCs

According to the obtained results, several conclusions can be drawn as follows:

- Incorporating 14.4% of the total volume by mPCMs, the mixture (PCM14) is able to achieve the same slump flow as the reference mortar (REF) however, in exchange of a higher water-to-binder ratio which substantially decreases the material compressive strength and E-modulus.
- Anisotropic compressive behaviours are found in two different directions of the LCCCs. The out-of-plane compressive strength and stiffness of the LCCCs are significantly better than that of the in-plane values.
- Although due to the high porosity the LCCCs have obviously reduced compressive strength and stiffness with respect to the constituent materials, the out-of-plane compressive strength of the LCCCs is comparable to conventional lightweight cementitious materials, for example foam concrete with the same density.
- In contrast to the reference mortar (REF), preparing the LCCCs with the mPCMs incorporated mortar (PCM14) leads to significantly less reduction in compressive strength and stiffness. Surprisingly, in the out-of-plane direction, the relative stiffness of the LCCCs made of PCM14 are even higher than the material E-modulus.
- Air void content is found to be a determinative factor on the out-of-plane compressive strength of the LCCCs. According to the numerical simulations, stress intensity caused by the air voids leads to potential crack initiation which substantially decreases the compressive strength of the LCCCs. While the negative effect of air voids on the in-plane strength is much less notable.

9.2 The conclusion of thermal performance of LCCCs

According to the obtained results, several conclusions can be drawn as follows:

- The thermal conductivity of LCCCs is comparable to foam concrete with the same density. The effect of geometry randomness between R0, R3 and R7 specimen on the thermal conductivity is minor.
- Although the geometry randomness has negligible effect on the overall thermal conductivity of LCCCs, in the middle cross section of specimen, the change of geometry randomness results in the change of thermal bridges of the heat transfer in the interior structure of specimen, leading to the significant influence on the y-direction heat flux.
- Compared with geometry randomness, the increasing of porosity of the LCCCs has more effect on the decrease of thermal conductivity of the specimen. Moreover, keeping a constant porosity, breaking the thermal bridge on the heat transfer direction can effectively and dramatically reduce the thermal conductivity of the specimen, therefore improving the thermal insulation performance of the LCCCs.
- In this research, the natural convection and radiation has a minor influence on determining the thermal conductivity of the LCCCs. Possible reason is assumed to be the small temperature gradient within each pore. Therefore, the simulated thermal conductivity of the LCCCs using steady state heat transfer model without considering natural convection is still accurate enough.

- According to the simulation results, the incorporation of mPCMs in the modified cementitious mortar has positive effect on reducing the thermal conductivity of the LCCCs.

9.3 The general conclusion of research

The LCCCs developed in this work have high porosity as well as good compressive strength as lightweight materials which makes them a promising insulation construction material. With the aid of 3D printing technology and the combination with traditional casting method, the LCCCs specimen can be easily manufactured, therewith the experimental test can be conducted on the LCCCs for acquiring its mechanical properties in the laboratory. Overall, the novel LCCCs is a promising alternative for traditional foam concrete with respect of both mechanical and thermal properties. The air voids existing on the cell walls of specimen are decisive on the compressive strength of LCCCs. From the thermal performance point of view, the increasing of porosity plays a key role on enhancing the thermal insulation properties, more importantly, eliminating the thermal bridges can effectively reduce the thermal conductivity of the LCCCs.

9.4 Discussion

9.4.1 The compressive properties

- It has been shown that the compressive strength of the specimen depends on its size. By comparing the results depicted in Figure 6-1 and Figure 6-3, higher compressive strength was obtained on smaller specimen. As expected, the compression failure of quasi-brittle material such as concrete always exhibits the size effect and the possible explanation related to this phenomenon is that the compressive failure of the specimen is not fully controlled by the material strength criterion. However, in this research, the intrinsic cause for the size effect and the relationship between it with the geometry heterogeneity and anisotropic compressive behaviour are not studied and a further exploration is needed in the future research.
- Depending on the nodal connectivity, cellular structure can be classified as stretch dominant structure and bending dominant structure, the former one is suitable for lightweight, load bearing applications. In this research, the structure specification of architected Voronoi-shaped LCCCs belongs to stretch dominant structure, additionally, the tested mechanical properties such anisotropic behaviour, the high relative strength can represent the general trend of stretch dominant structure's behaviour when it is combined with cementitious material.
- In this research, the digital image correlation (DIC) was used for strain measurement on the x direction which is perpendicular to the loading direction. However, the DIC results is not ideal for clearly demonstrate the crack propagation pattern between R0, R3 and R7 specimen because the frame rate of picture capturing was not high enough comparing to the crack propagating speed. In case a high frame rate camera is available, clarifying crack development would be possible.

9.4.2 The thermal properties

- In this research, the method of calculating the thermal conductivity is based on applying constant temperature difference on the inner and outer surface on the y direction of specimen. The advantage of this method is easy and time saving, on the contrast the limitation of this method is obvious: it is an ideal and unrealistic assumed boundary condition. More practical solution can be realized by collecting the weather information and average temperature data according to different season and area in Netherlands as the applied boundary conditions for analysing the thermal performance.
- In this study, only the sensible heat was considered when calculating the thermal conductivity of the LCCCs specimen manufactured by mPCM incorporated cementitious mortar. When considering the latent heat, due to the liquid-solid phase change occur, explicitly including mPCMs spheres in the numerical model by a multiscale simulation approach would be feasible.

9.4.3 Printing procedure

- The constituent of LCCCs printable mix design is based on a trial- and- error method, the rheological test has not been considered in the research. Therefore, the fresh properties of the mix design are not experimentally quantified. More possible mix design should be proposed and compared for the optimizing the fresh and hardened properties of printed filaments and specimen.
- During the deposition process, it is shown in Figure 8-3 the deformation of printed filaments due to the self-weight was observed. Some air bobbles are entrapped in the printed filament may lead to the mechanical loss. The extrudability , flowability , buildability of printable cementitious material as well as the quality of interlayer bond of the printed filaments were not tested in the research.

9.5 Recommendations

This research provides a groundwork for developing a novel lightweight cellular cementitious composite (LCCCs) and exploring its mechanical and thermal properties on the lab specimen-scale level, several conclusions are drawn based on our research. This research should be regarded as the starting point and we will give some recommendations for the future research:

- More research can be carried out on different mixture designs including different content of PCMs as the base material for manufacturing the LCCCs
- Regarding the mechanical properties, the larger (even real-scale) elements and constructions should be tested. Due to the existence of size effect, the practical mechanical performance might be slightly different with what we tested in the research.
- The potential use of the LCCCs could be as partition wall with the function of thermal insulation. In addition to the compressive test, the shear strength of interface between layers on different printing direction (vertical and horizontal direction) could be evaluated by the shear bond test. On the other hand, when subjected to horizontal load, the vertical wall can undergo the bending in the vertical plane, therefore the flexural strength of the printing wall should be tested.

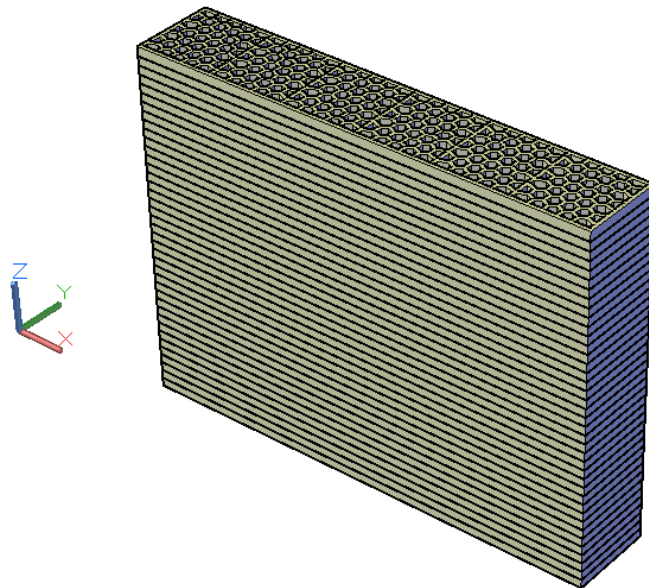


Figure 9-1 The graphic demonstration of printing wall

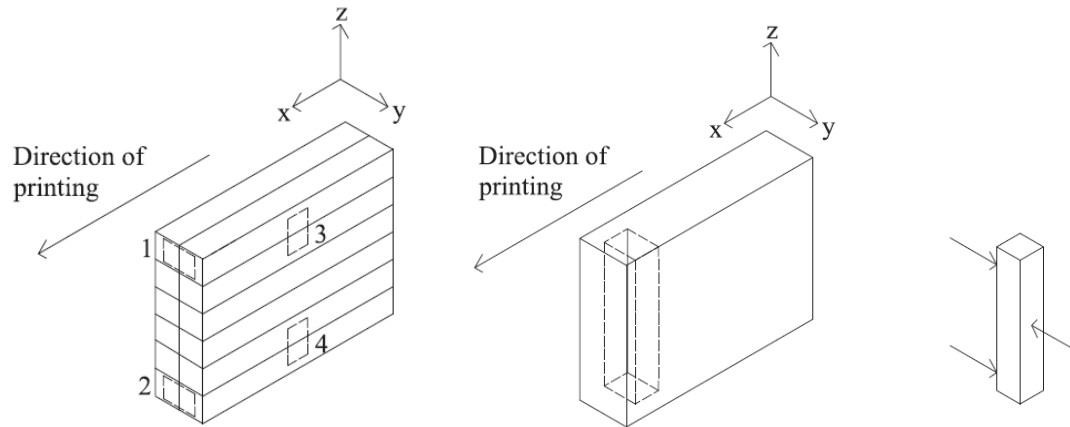


Figure 9-2 The schematic demonstration of shear bond of the interface (left) and the bending load on the vertical plane (right), adopted from [106].

- Since the air void is a determinative factor on the out-of-plane compressive strength of the LCCCs, the optimized specimen preparation method can be design for eliminating the entrapped air in the mixing and casting process.
- The new design direction could be put upon minimizing the effect of thermal bridges, by optimizing the complex geometry of the cellular composite on certain amount of porosity. From the conclusion, we clearly realized the porosity is the most important factor on determining the thermal conductivity of LCCCs, however, the reduction of porosity is in the cost of the mechanical strength loss. Therefore, the under the premise of keeping sufficient mechanical strength, the thermal property modification is meaningful.
- Although natural convection has minor effect on influencing the calculation of thermal conductivity, however when the next step is exploring the application of LCCCs in the real scaled construction level, the effect of air flow on the height could be an interesting topic.
- The latent heat as well as the thermal storage capacity during the phase change process should be explored further when considering the incorporation of PCM in the cementitious material.
- The fresh and hardened properties of the 3D printing LCCCs can be deeply explored after this attempt of printing in this research. On the other hand, the orientation of printing routine, the interlayer bond quality and the deformation of printing filaments and other 3D printing related issues can be regarded as a series of new topic for developing. Once the 3D printing LCCCs is designed as the structural element, on the structure safety point of view, both analytical and numerical calculation can be carried out for both checking the satisfaction design criteria and optimizing the element size.

Bibliography

1. Pérez-Lombard, L., J. Ortiz, and C. Pout, *A review on buildings energy consumption information*. Energy and Buildings, 2008. **40**(3): p. 394-398.
2. Abu-Jdayil, B., et al., *Traditional, state-of-the-art and renewable thermal building insulation materials: An overview*. Construction and Building Materials, 2019. **214**: p. 709-735.
3. Takht Ravanchi, M. and S. Sahebdehfar, *Catalytic conversions of CO₂ to help mitigate climate change: Recent process developments*. Process Safety and Environmental Protection, 2021. **145**: p. 172-194.
4. Nederland, R.v.O. *monitor-energiebesparing-gebouwde-omgeving-2019*. 2019 February 16,2021]; Available from: <https://www.rvo.nl/sites/default/files/2021/01/monitor-energiebesparing-gebouwde-omgeving-2019.pdf>.
5. Netherlands, M.o.E.A.o.t. *Energy Report:Transition to sustainable energy*. 2016 February 16,2021]; Available from: <https://www.government.nl/binaries/government/documents/reports/2016/01/01/energy-report-transition-to-sustainable-energy/Energy+Report+Transition+to+sustainable+energy.pdf>.
6. Karamanos, A., S. Hadjarakou, and A.M. Papadopoulos, *The impact of temperature and moisture on the thermal performance of stone wool*. Energy and Buildings, 2008. **40**(8): p. 1402-1411.
7. Sariisik, A. and G. Sariisik, *New production process for insulation blocks composed of EPS and lightweight concrete containing pumice aggregate*. Materials and Structures, 2012. **45**(9): p. 1345-1357.
8. Demirel, B., *Optimization of the composite brick composed of expanded polystyrene and pumice blocks*. Construction and Building Materials, 2013. **40**: p. 306-313.
9. Schiavoni, S., et al., *Insulation materials for the building sector: A review and comparative analysis*. Renewable and Sustainable Energy Reviews, 2016. **62**: p. 988-1011.
10. Simmler, H., et al., *Vacuum Insulation Panels-Study on VIP-components and panels for service life prediction of VIP in building applications (Subtask A)*. 2005.
11. Zwerger, M. and H. Klein. *Integration of VIP's into external wall insulation systems*. in *Proceedings of the 7th International Vacuum Insulation Symposium*. 2005.
12. Chica, L., A.J.C. Alzate, and B. Materials, *Cellular concrete review: New trends for application in construction*. 2019. **200**: p. 637-647.
13. Ramamurthy, K., et al., *A classification of studies on properties of foam concrete*. 2009. **31**(6): p. 388-396.
14. Amran, Y.H.M., N. Farzadnia, and A.A. Abang Ali, *Properties and applications of foamed concrete; a review*. Construction and Building Materials, 2015. **101**: p. 990-1005.
15. Ruiz-Herrero, J.L., et al., *Mechanical and thermal performance of concrete and mortar cellular materials containing plastic waste*. Construction and Building Materials, 2016. **104**: p. 298-310.
16. Bouguerra, A., et al., *Effect of microstructure on the mechanical and thermal properties of lightweight concrete prepared from clay, cement, and wood aggregates*. 1998. **28**(8): p. 1179-1190.
17. Safi, B., et al., *The use of plastic waste as fine aggregate in the self-compacting mortars: Effect on physical and mechanical properties*. Construction and Building Materials, 2013. **43**: p. 436-442.
18. Siddique, R., J. Khatib, and I. Kaur, *Use of recycled plastic in concrete: a review*. Waste Manag, 2008. **28**(10): p. 1835-52.

19. Engelbrecht, S., et al. *Cellular structures for optimal performance*. in *Proc. SFF Symposium. Austin*. 2009.
20. Li, K., et al., *Dynamic crushing behavior of honeycomb structures with irregular cell shapes and non-uniform cell wall thickness*. 2007. **44**(14-15): p. 5003-5026.
21. Barbier, C., et al., *New laws for the tension/compression properties of Voronoi closed-cell polymer foams in relation to their microstructure*. 2014. **45**: p. 110-122.
22. Wang, H., et al., *Analysing effective thermal conductivity of 2D closed-cell foam based on shrunk Voronoi tessellations*. 2017. **69**(6): p. 451-470.
23. Li, Z., et al., *Study on the Thermal Properties of Closed-Cell Metal Foams Based on Voronoi Random Models*. Numerical Heat Transfer, Part A: Applications, 2013. **64**(12): p. 1038-1049.
24. Sotomayor, O., *Numerical Modeling of Random 2D and 3D Structural Foams Using Voronoi Diagrams: A Study of Cell Regularity and Compression Response*. 2013.
25. Ben Romdhane, S., et al., *A review on thermal energy storage using phase change materials in passive building applications*. Journal of Building Engineering, 2020. **32**.
26. Drissi, S., et al., *A review of microencapsulated and composite phase change materials: Alteration of strength and thermal properties of cement-based materials*. Renewable and Sustainable Energy Reviews, 2019. **110**: p. 467-484.
27. Cabeza, L.F., et al., *Use of microencapsulated PCM in concrete walls for energy savings*. Energy and Buildings, 2007. **39**(2): p. 113-119.
28. Ling, T.-C. and C.-S. Poon, *Use of phase change materials for thermal energy storage in concrete: An overview*. Construction and Building Materials, 2013. **46**: p. 55-62.
29. Navarro, L., et al., *Thermal energy storage in building integrated thermal systems: A review. Part 2. Integration as passive system*. Renewable Energy, 2016. **85**: p. 1334-1356.
30. Tyagi, V.V. and D. Buddhi, *PCM thermal storage in buildings: A state of art*. Renewable and Sustainable Energy Reviews, 2007. **11**(6): p. 1146-1166.
31. Kuznik, F., J. Virgone, and J. Noel, *Optimization of a phase change material wallboard for building use*. Applied Thermal Engineering, 2008. **28**(11-12): p. 1291-1298.
32. Hunger, M., et al., *The behavior of self-compacting concrete containing micro-encapsulated Phase Change Materials*. Cement and Concrete Composites, 2009. **31**(10): p. 731-743.
33. Jayalath, A., et al., *Properties of cementitious mortar and concrete containing micro-encapsulated phase change materials*. Construction and Building Materials, 2016. **120**: p. 408-417.
34. Cunha, S., M. Lima, and J.B. Aguiar, *Influence of adding phase change materials on the physical and mechanical properties of cement mortars*. Construction and Building Materials, 2016. **127**: p. 1-10.
35. Berman, B., *3-D printing: The new industrial revolution*. Business Horizons, 2012. **55**(2): p. 155-162.
36. Moini, M., et al., *Additive Manufacturing and Performance of Architected Cement-Based Materials*. Adv Mater, 2018. **30**(43): p. e1802123.
37. Lim, S., et al., *Developments in construction-scale additive manufacturing processes*. Automation in Construction, 2012. **21**: p. 262-268.
38. Hossain, M.A., et al., *A Review of 3D Printing in Construction and its Impact on the Labor Market Sustainability*, 2020. **12**(20).
39. Irving, M. *3D printed reinforced concrete bridge opens in the Netherlands*. 2017 [cited 2021 22 February]; Available from: <https://newatlas.com/3d-printed-concrete-bridge/51796/>.
40. *Project Milestone*. 2018 [cited 2021 22 February]; Available from: <https://3dprintedhouse.nl/en/project-info/project-milestone/>.
41. Buitrago, B.L., et al., *Modelling of composite sandwich structures with honeycomb core subjected to high-velocity impact*. Composite Structures, 2010. **92**(9): p. 2090-2096.

42. Savija, B., *Use of 3D printing to create multifunctional cementitious composites: review, challenges and opportunities*. RILEM Technical Letters, 2020. **5**: p. 17-25.
43. Schaedler, T.A. and W.B. Carter, *Architected Cellular Materials*. Annual Review of Materials Research, 2016. **46**(1): p. 187-210.
44. Ashby, M.F., et al., *Metal foams: a design guide*-Butterworth-Heinemann, Oxford, UK, ISBN 0-7506-7219-6, Published 2000, Hardback, 251 pp., \$75.00. 2002. **1**(23): p. 119.
45. Ashby, M.F. and L.J.J.P.S.o.t.U.o.C. Gibson, Cambridge, UK, *Cellular solids: structure and properties*. 1997: p. 175-231.
46. Bhate, D., et al., *Classification and selection of cellular materials in mechanical design: Engineering and biomimetic approaches*. 2019. **3**(1): p. 19.
47. Zhang, Q., et al., *Bioinspired engineering of honeycomb structure – Using nature to inspire human innovation*. Progress in Materials Science, 2015. **74**: p. 332-400.
48. Gu, S., et al., *On the design of two-dimensional cellular metals for combined heat dissipation and structural load capacity*. 2001. **44**(11): p. 2163-2175.
49. Abdullahi, H.S. and S.J.T.-W.S. Gao, *A novel multi-cell square tubal structure based on Voronoi tessellation for enhanced crashworthiness*. 2020. **150**: p. 106690.
50. Snoeck, D. and P. Criel, *Voronoi diagrams and self-healing cementitious materials: a perfect match*. Advances in Cement Research, 2019. **31**(6): p. 261-269.
51. Tao, Y., et al., *A case study: Mechanical modeling optimization of cellular structure fabricated using wood flour-filled polylactic acid composites with fused deposition modeling*. 2019. **216**: p. 360-365.
52. Mechtcherine, V., et al., *Extrusion-based additive manufacturing with cement-based materials – Production steps, processes, and their underlying physics: A review*. Cement and Concrete Research, 2020. **132**.
53. du Plessis, A., et al., *Biomimicry for 3D concrete printing: A review and perspective*. Additive Manufacturing, 2021. **38**.
54. Wang, L., et al., *Mechanical behaviors of 3D printed lightweight concrete structure with hollow section*. Archives of Civil and Mechanical Engineering, 2020. **20**(1).
55. Sajadi, S.M., et al., *Direct Ink Writing of Cement Structures Modified with Nanoscale Additive*. Advanced Engineering Materials, 2019. **21**(8).
56. Xu, Y., et al., *Cementitious cellular composites with auxetic behavior*. Cement and Concrete Composites, 2020. **111**.
57. Nguyen-Van, V., et al., *Bioinspired cellular cementitious structures for prefabricated construction: Hybrid design & performance evaluations*. Automation in Construction, 2020. **119**.
58. Khudhair, A.M. and M.M. Farid, *A review on energy conservation in building applications with thermal storage by latent heat using phase change materials*. Energy Conversion and Management, 2004. **45**(2): p. 263-275.
59. Kazemi, Z. and S.M. Mortazavi, *A new method of application of hydrated salts on textiles to achieve thermoregulating properties*. Thermochimica Acta, 2014. **589**: p. 56-62.
60. Zhang, D., et al., *Development of thermal energy storage concrete*. Cement and Concrete Research, 2004. **34**(6): p. 927-934.
61. Sakulich, A.R. and D.P. Bentz, *Incorporation of phase change materials in cementitious systems via fine lightweight aggregate*. Construction and Building Materials, 2012. **35**: p. 483-490.
62. Zhao, C.Y. and G.H. Zhang, *Review on microencapsulated phase change materials (MEPCMs): Fabrication, characterization and applications*. Renewable and Sustainable Energy Reviews, 2011. **15**(8): p. 3813-3832.
63. Cao, V.D., et al., *Microencapsulated phase change materials for enhancing the thermal performance of Portland cement concrete and geopolymers concrete for passive building applications*. Energy Conversion and Management, 2017. **133**: p. 56-66.

64. Lecompte, T., et al., *Mechanical and thermo-physical behaviour of concretes and mortars containing phase change material*. Energy and Buildings, 2015. **94**: p. 52-60.
65. Savija, B., H. Zhang, and E. Schlangen, *Influence of Microencapsulated Phase Change Material (PCM) Addition on (Micro) Mechanical Properties of Cement Paste*. Materials (Basel), 2017. **10**(8).
66. Snoeck, D., et al., *Encapsulated Phase-Change Materials as additives in cementitious materials to promote thermal comfort in concrete constructions*. Materials and Structures, 2014. **49**(1-2): p. 225-239.
67. Yang, H.-B., et al., *Mechanical properties of concrete containing phase-change material*. Journal of the Chinese Institute of Engineers, 2016. **39**(5): p. 521-530.
68. Lucas, S., et al., *Fresh state characterization of lime mortars with PCM additions*. 2010. **20**(6).
69. Cunha, S., et al., *Mortars based in different binders with incorporation of phase-change materials: Physical and mechanical properties*. 2015. **19**(10): p. 1216-1233.
70. Park, S.-Y., et al., *Modeling and observation of compressive behaviors of closed cellular structures using central Voronoi tessellation concepts*. International Journal of Precision Engineering and Manufacturing, 2015. **16**(12): p. 2459-2465.
71. Rege, A., M. Hillgärtner, and M. Itskov, *Mechanics of biopolymer aerogels based on microstructures generated from 2-d Voronoi tessellations*. The Journal of Supercritical Fluids, 2019. **151**: p. 24-29.
72. Romero Rodríguez, C., et al., *Fundamental investigation on the frost resistance of mortar with microencapsulated phase change materials*. Cement and Concrete Composites, 2020. **113**.
73. Xu, Y., et al., *Cementitious cellular composites with auxetic behavior*. Cement and Concrete Composites, 2020. **111**: p. 103624.
74. Xu, Y., et al., *Tunable mechanical behavior of auxetic cementitious cellular composites (CCCs): Experiments and simulations*. Construction and Building Materials, 2021. **266**: p. 121388.
75. Xu, Y. and B. Šavija, *Development of strain hardening cementitious composite (SHCC) reinforced with 3D printed polymeric reinforcement: Mechanical properties*. Composites Part B: Engineering, 2019. **174**.
76. Xu, Y., et al., *Cementitious composites reinforced with 3D printed functionally graded polymeric lattice structures: experiments and modelling*. Additive Manufacturing, 2021: p. 101887.
77. Kantro, D.L.J.C., Concrete and Aggregates, *Influence of water-reducing admixtures on properties of cement paste—a miniature slump test*. 1980. **2**(2): p. 95-102.
78. Gao, J. and A. Fourie, *Spread is better: An investigation of the mini-slump test*. Minerals Engineering, 2015. **71**: p. 120-132.
79. Panda, B., S. Chandra Paul, and M. Jen Tan, *Anisotropic mechanical performance of 3D printed fiber reinforced sustainable construction material*. Materials Letters, 2017. **209**: p. 146-149.
80. Liu, D., et al., *Towards understanding the influence of porosity on mechanical and fracture behaviour of quasi-brittle materials: experiments and modelling*. International Journal of Fracture, 2017. **205**(1): p. 57-72.
81. Cunha-Reis, C., et al., *Influence of porosity and fibre diameter on the degradation of chitosan fibre-mesh scaffolds and cell adhesion*. J Mater Sci Mater Med, 2007. **18**(2): p. 195-200.
82. Van Mier, J.G., *Fracture processes of concrete*. Vol. 12. 2017: CRC press.
83. Kerschbaumer, R.C., et al., *Comparison of steady-state and transient thermal conductivity testing methods using different industrial rubber compounds*. Polymer Testing, 2019. **80**.
84. Gustafsson, S.E., *Transient plane source techniques for thermal conductivity and thermal diffusivity measurements of solid materials*. Review of Scientific Instruments, 1991. **62**(3): p. 797-804.
85. 22007-2, I., *Plastics—Determination of Thermal Conductivity and Thermal Diffusivity—Part 2: Transient Plane Heat Source (Hot Disc) Method*. 2008, ISO Geneva, Switzerland.

86. Elkholy, A., H. Sadek, and R. Kempers, *An improved transient plane source technique and methodology for measuring the thermal properties of anisotropic materials*. International Journal of Thermal Sciences, 2019. **135**: p. 362-374.
87. Meng, D., et al., *Mechanical behaviour of a polyvinyl alcohol fibre reinforced engineered cementitious composite (PVA-ECC) using local ingredients*. Construction and Building Materials, 2017. **141**: p. 259-270.
88. Jankowiak, T. and T. Lodygowski, *Identification of parameters of concrete damage plasticity constitutive model*. Foundations of civil and environmental engineering, 2005.
89. Fonseca, P.C. and G.W. Scherer, *An image analysis procedure to quantify the air void system of mortar and concrete*. Materials and Structures, 2014. **48**(10): p. 3087-3098.
90. Liu, Z., W. Hansen, and B. Meng, *Characterisation of air-void systems in concrete*. Magazine of Concrete Research, 2016. **68**(4): p. 178-186.
91. Fantous, T. and A. Yahia, *Air-void characteristics in highly flowable cement-based materials*. Construction and Building Materials, 2020. **235**: p. 117454.
92. Guo, S., et al., *Ultrasonic scattering measurement of air void size distribution in hardened concrete samples*. Construction and Building Materials, 2016. **113**: p. 415-422.
93. Al-Tamimi, A.S., et al., *Effect of Geometry of Holes on Heat Transfer of Concrete Masonry Bricks Using Numerical Analysis*. Arabian Journal for Science and Engineering, 2017. **42**(9): p. 3733-3749.
94. Al-Tamimi, A.S., et al., *Effect of insulation materials and cavity layout on heat transfer of concrete masonry hollow blocks*. Construction and Building Materials, 2020. **254**.
95. Steven, C.K. *Materials thermal properties database*. 2001; Available from: <https://www.thermtest.com/materials-database>.
96. Bergman, T.L., et al., *Introduction to heat transfer*. 2011: John Wiley & Sons.
97. Hyun, S., H.J.M.S. Nakajima, and E. A, *Anisotropic compressive properties of porous copper produced by unidirectional solidification*. 2003. **340**(1-2): p. 258-264.
98. Li, F., et al., *Fabrication, pore structure and compressive behavior of anisotropic porous titanium for human trabecular bone implant applications*. J Mech Behav Biomed Mater, 2015. **46**: p. 104-14.
99. Espadas-Escalante, J.J. and F. Avilés, *Anisotropic compressive properties of multiwall carbon nanotube/polyurethane foams*. Mechanics of Materials, 2015. **91**: p. 167-176.
100. Zhang, H., et al., *Size effect on splitting strength of hardened cement paste: Experimental and numerical study*. Cement and Concrete Composites, 2018. **94**: p. 264-276.
101. Hayen, R., et al., *Triaxial interaction of natural stone, brick and mortar in masonry constructions*. 2009: p. 333-352.
102. Shah, H.A., Q. Yuan, and S. Zuo, *Air entrainment in fresh concrete and its effects on hardened concrete-a review*. Construction and Building Materials, 2021. **274**: p. 121835.
103. Mao, S., A. Kan, and N. Wang, *Numerical analysis and experimental investigation on thermal bridge effect of vacuum insulation panel*. Applied Thermal Engineering, 2020. **169**.
104. Ouali, S.J.G.T.R.C.D.R.E.A., *Thermal conductivity in relation to porosity and geological stratigraphy*. 2009. **4**: p. 23-29.
105. Panda, B. and M.J. Tan, *Experimental study on mix proportion and fresh properties of fly ash based geopolymer for 3D concrete printing*. Ceramics International, 2018. **44**(9): p. 10258-10265.
106. Rahul, A.V., et al., *Mechanical characterization of 3D printable concrete*. Construction and Building Materials, 2019. **227**.

Appendix A

The simulation setup in ANSYS

Geometry Modeling

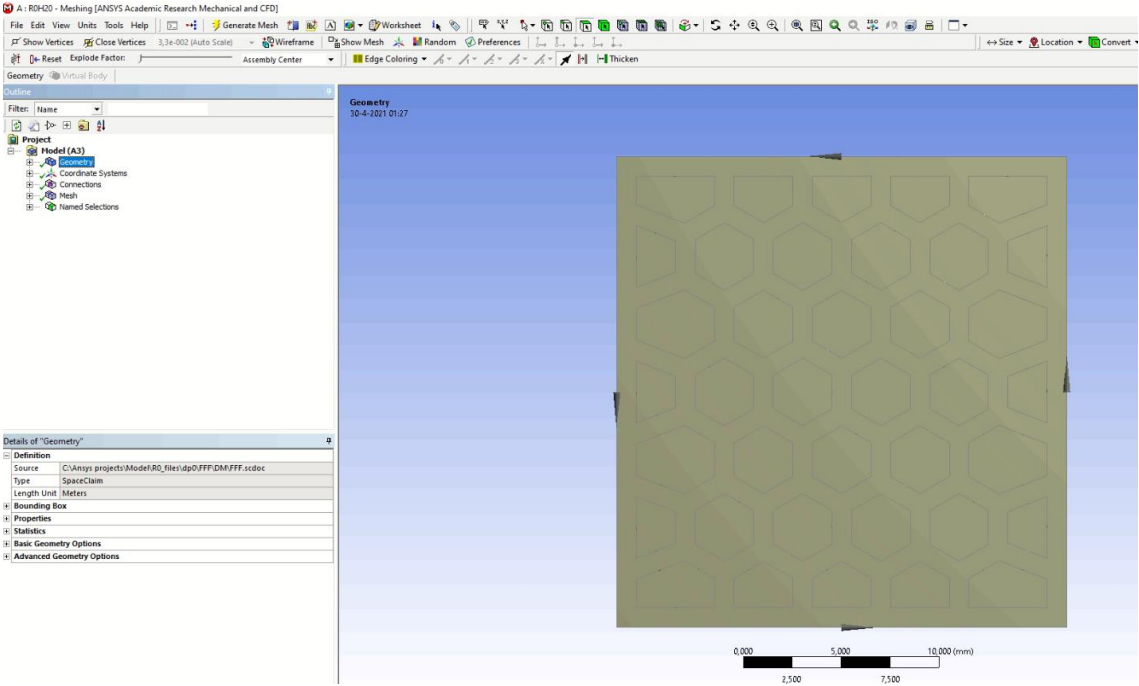
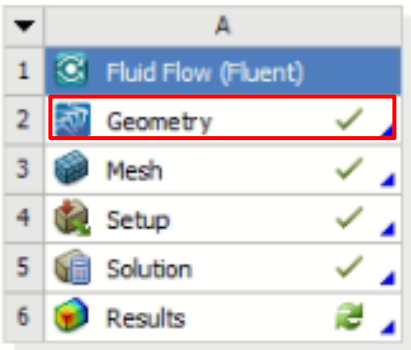


Figure A-1 Geometry Modelling Using Design Modeler

Meshing

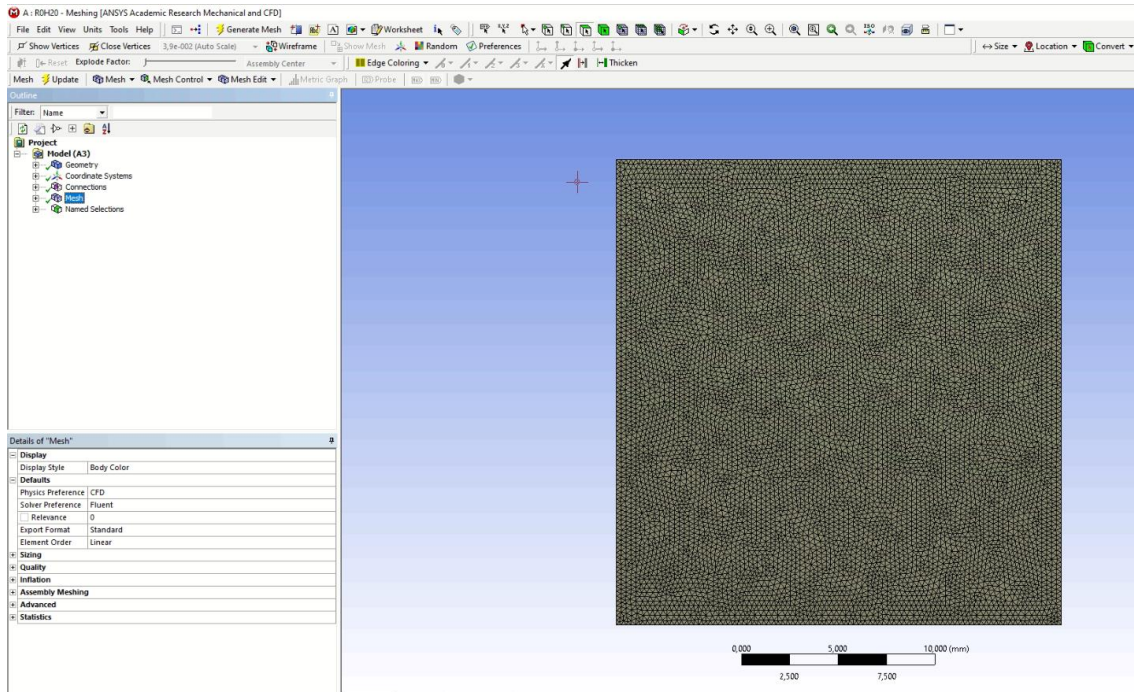
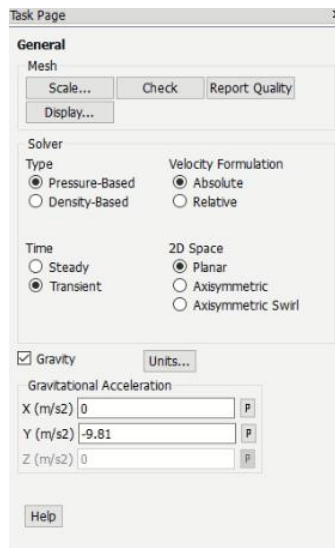


Figure A-2 Generating meshing

General setup

In general setup, the item for the solver must be in pressure based, absolute velocity formulation, transient, 2D planar and with gravitational force acting downward $y=-9.81 \text{ m/s}^2$



Model

In this study ,the model steps are laminar flow model and energy equation

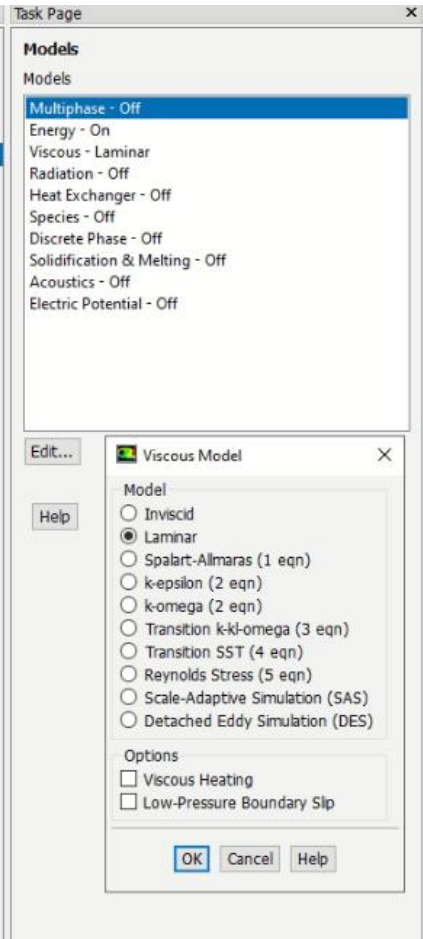


Figure A-3 Model set up

Materials

Define the properties of air as the fluid inside the cavity, define the properties of mortar including density ,specific heat and thermal capacity.

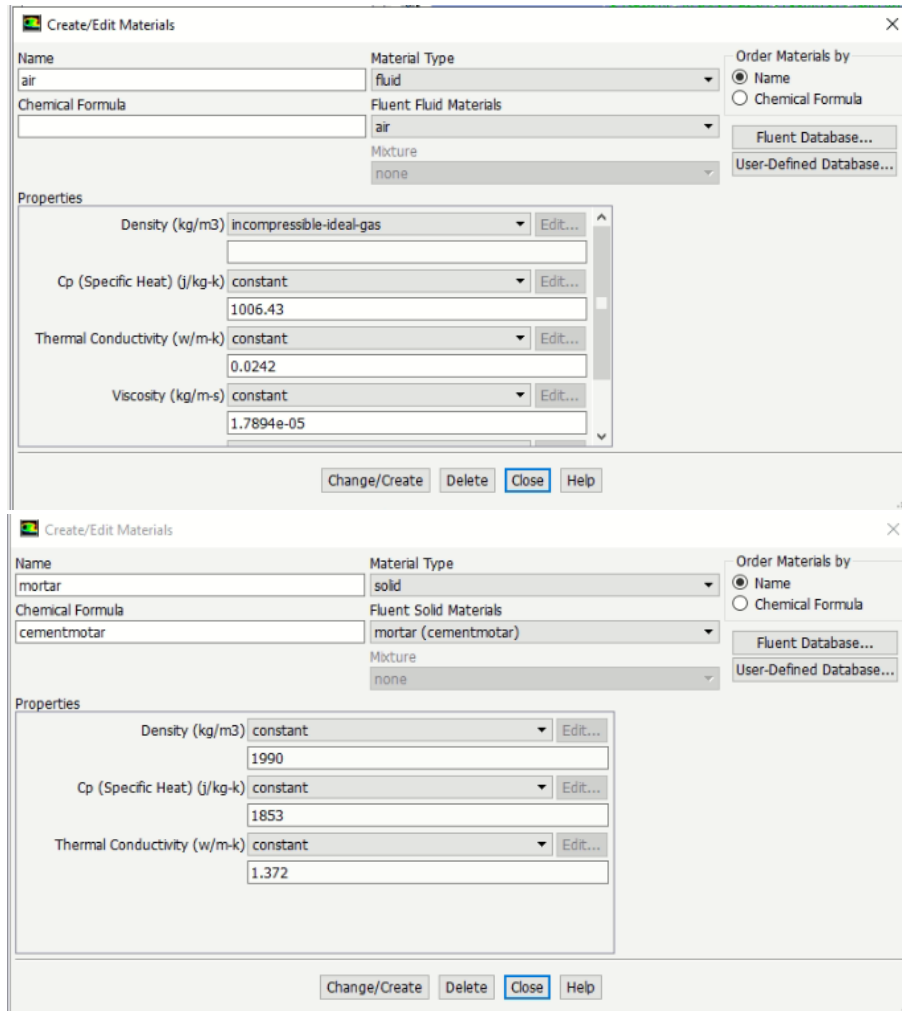


Figure A-4 Material setups

Boundary Condition

After completing general setup and model setup, boundary condition needs to be specified for each of the wall. The cool wall boundary condition is set up on the bottom line of the model and the corresponding temperature is 293.15 K. The hot wall boundary condition is set up on the upper line of the model and the corresponding temperature is 373.15 K. The left and right line of the model are set up as insulated wall.

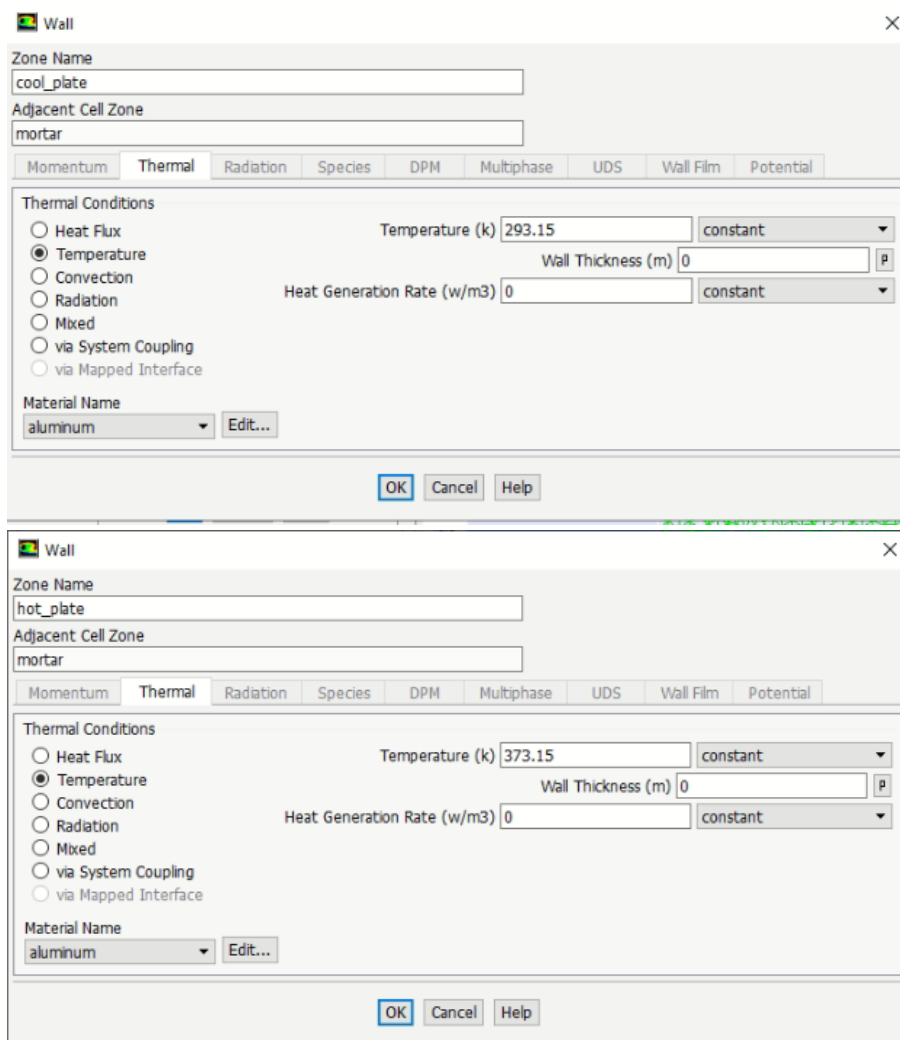


Figure A-5 Boundary conditions

Solution

In order to obtain more accurate results, the number of absolute convergence of each residual equations is set at 1e-06. Solution initialization is retain to be Hybrid Initialization.

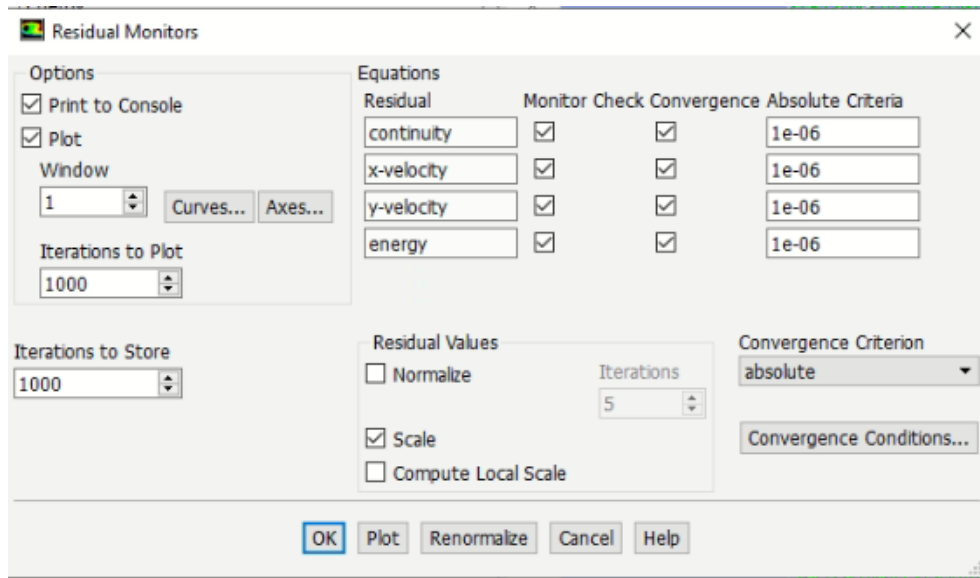


Figure A-6 Residual Convergence

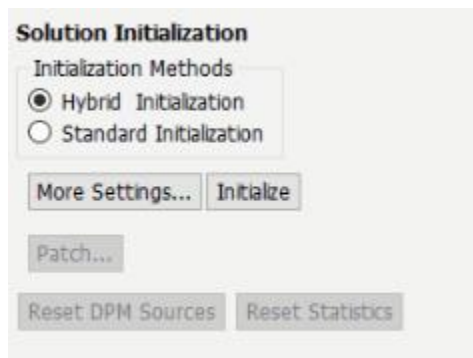


Figure A-7 Solution Initialization

Results

In result, CFD post processor is launched to verify the results calculated in form of graphical result such as temperature profile ,density profile ,velocity profile.

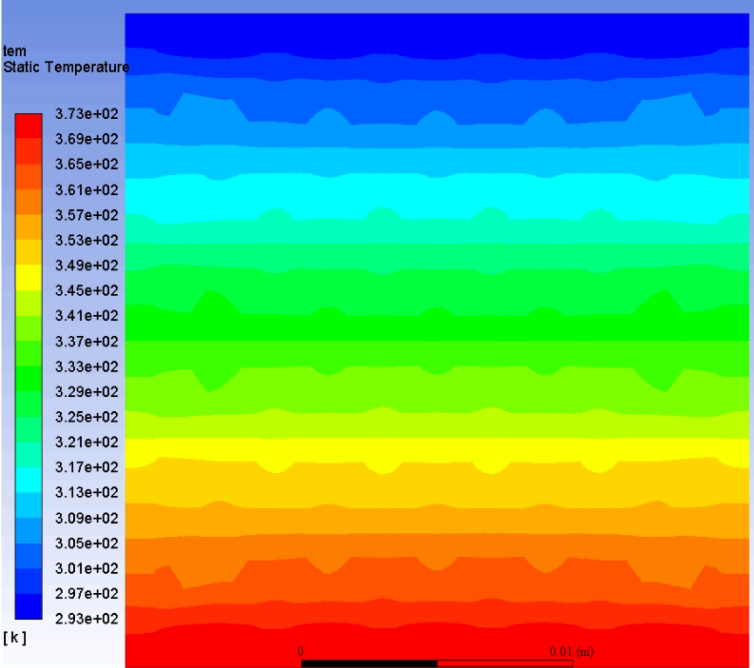


Figure A-8 temperature profile

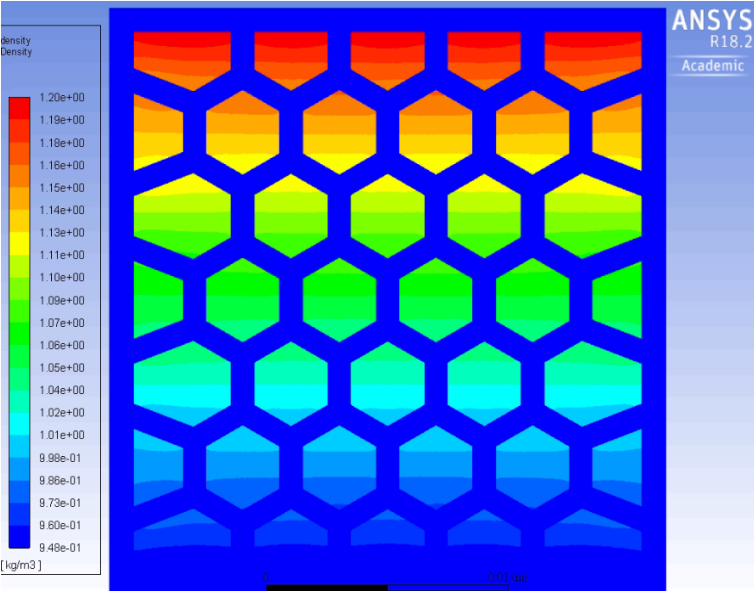
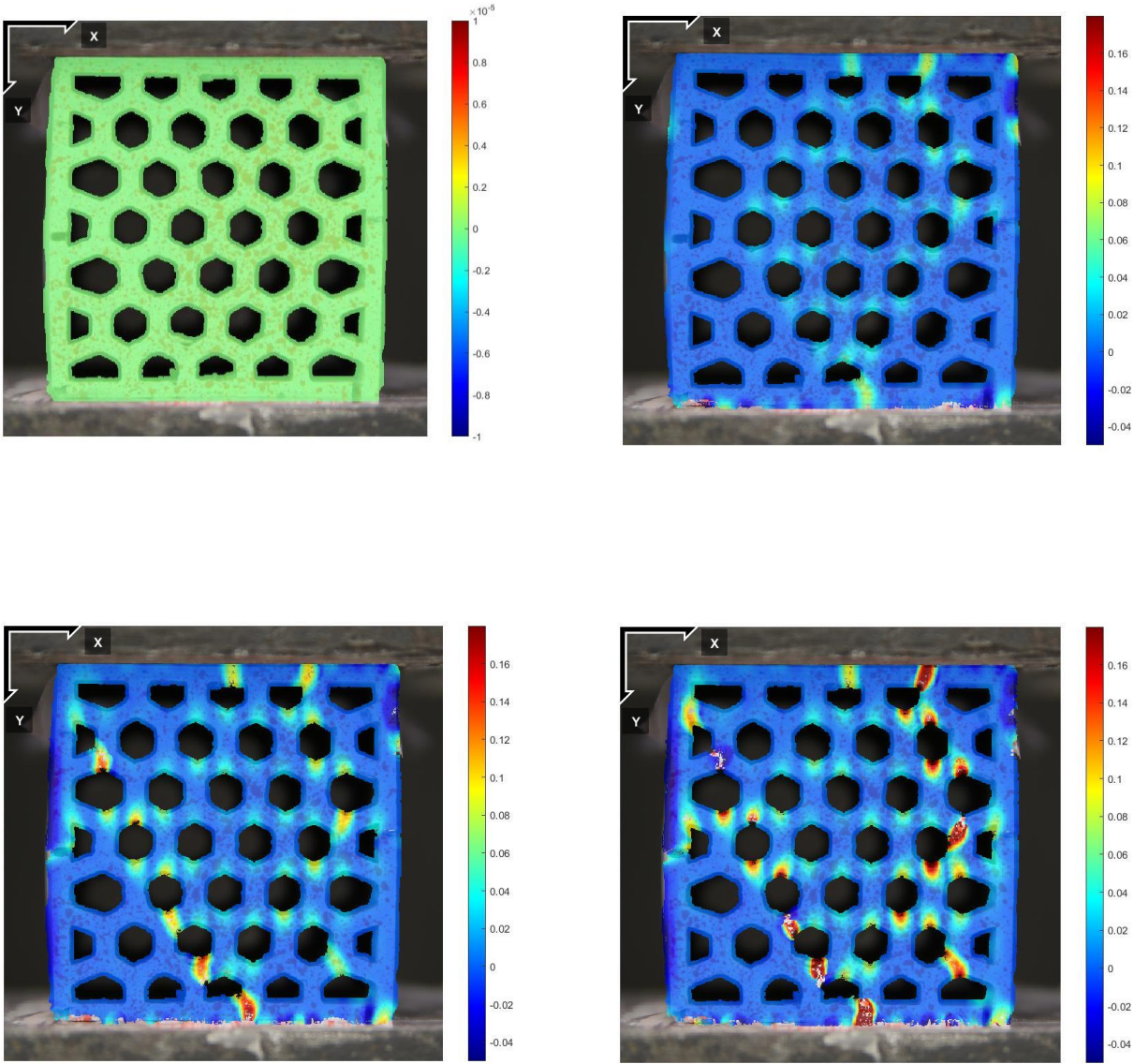


Figure A-9 density profile

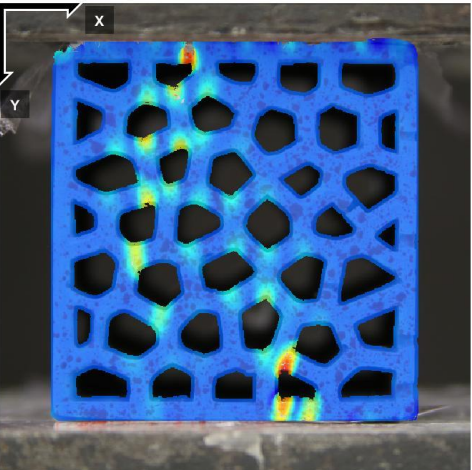
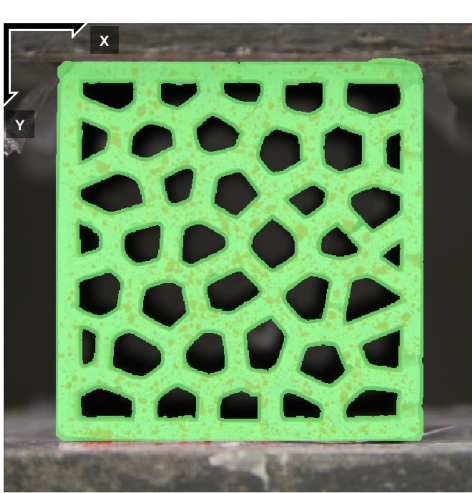
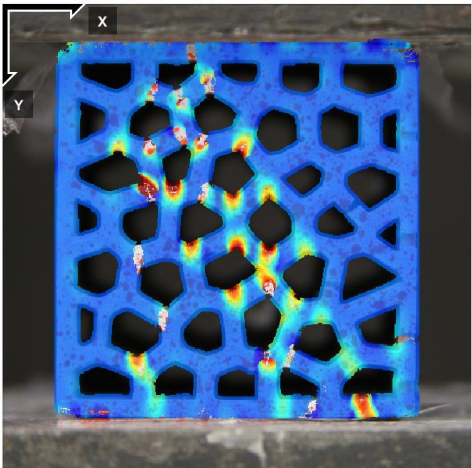
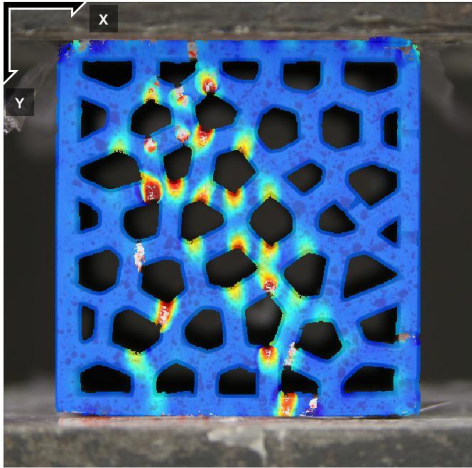
Appendix B

The DIC results of in-plane compression test

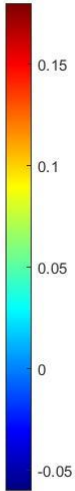
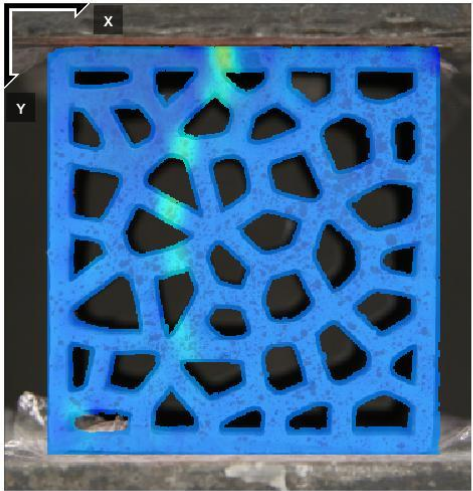
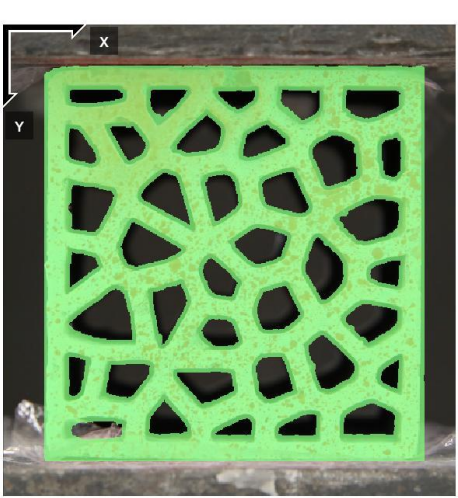
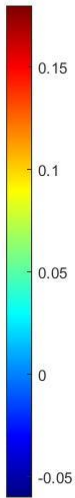
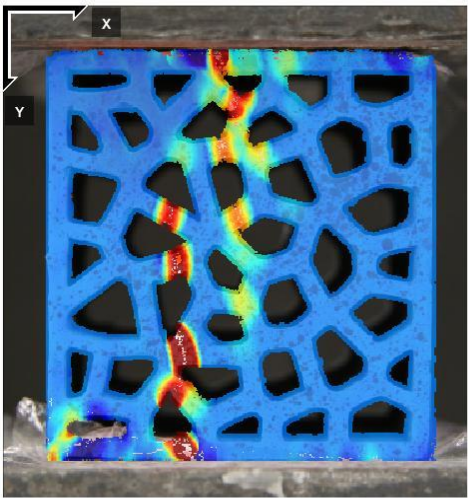
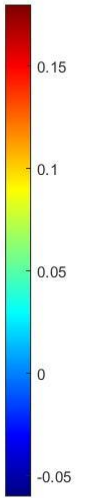
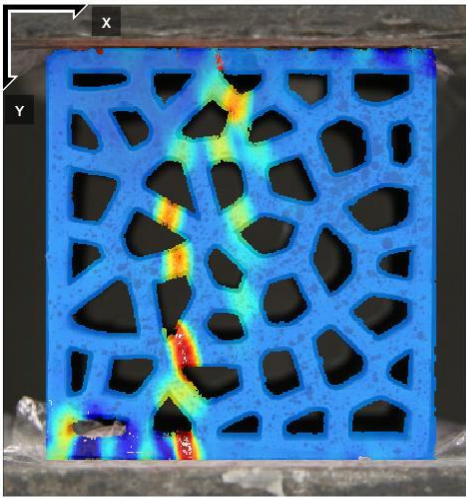
R0



R3



R7



Appendix C

G-code of printing path

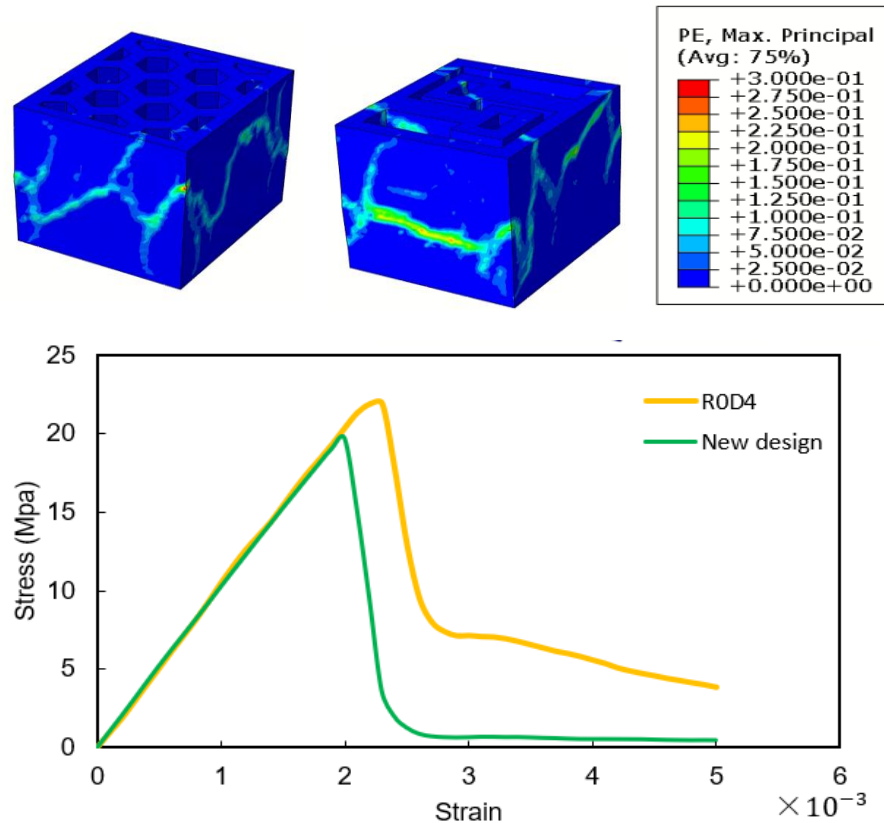
G1 X	88	Y	70.78	z	0
G1X	100	Y	50	z	0
G1X	124	Y	50	z	0
G1X	136	Y	70.78	z	0
G1X	160	Y	70.78	z	0
G1X	172	Y	50	z	0
G1X	196	Y	50	z	0
G1X	208	Y	70.78	z	0
G1X	232	Y	70.78	z	0
G1X	244	Y	50	z	0
G1X	268	Y	50	z	0
G1X	280	Y	70.78	z	0
G1X	280	Y	78.78	z	0
G1X	268	Y	99.57	z	0
G1X	244	Y	99.57	z	0
G1X	232	Y	78.78	z	0
G1X	208	Y	78.78	z	0
G1X	196	Y	99.57	z	0
G1X	172	Y	99.57	z	0
G1X	160	Y	78.78	z	0
G1X	136	Y	78.78	z	0
G1X	124	Y	99.57	z	0
G1X	100	Y	99.57	z	0

G1X	88	Y	78.78 z	0
G1X	68	Y	78.78 z	0
G1X	68	Y	128.36 z	0
G1X	88	Y	128.36 z	0
G1X	100	Y	107.57 z	0
G1X	124	Y	107.57 z	0
G1X	136	Y	128.36 z	0
G1X	160	Y	128.36 z	0
G1X	172	Y	107.57 z	0
G1X	196	Y	107.57 z	0
G1X	208	Y	128.36 z	0
G1X	232	Y	128.36 z	0
G1X	244	Y	107.57 z	0
G1X	268	Y	107.57 z	0
G1X	280	Y	128.36 z	0
G1X	280	Y	136.35 z	0
G1X	268	Y	157.14 z	0
G1X	244	Y	157.14 z	0
G1X	232	Y	136.35 z	0
G1X	208	Y	136.35 z	0
G1X	196	Y	157.14 z	0
G1X	172	Y	157.14 z	0
G1X	160	Y	136.35 z	0
G1X	136	Y	136.35 z	0
G1X	124	Y	157.14 z	0
G1X	100	Y	157.14 z	0
G1X	88	Y	136.35 z	0
G1X	68	Y	136.35 z	0
G1X	68	Y	185.92 z	0
G1X	88	Y	185.92 z	0
G1X	100	Y	165.14 z	0

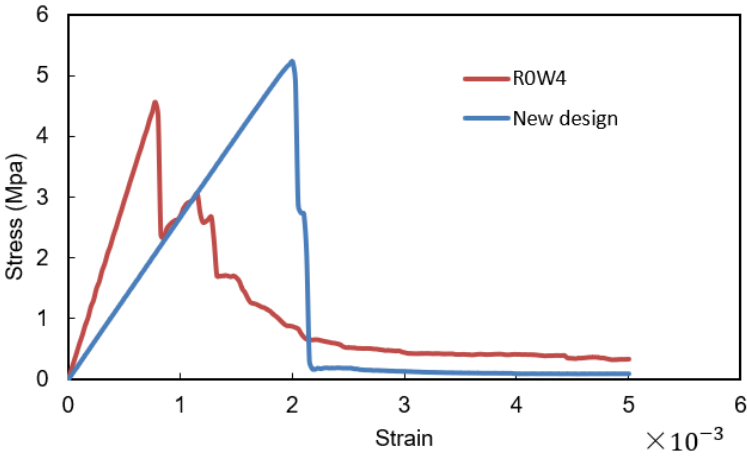
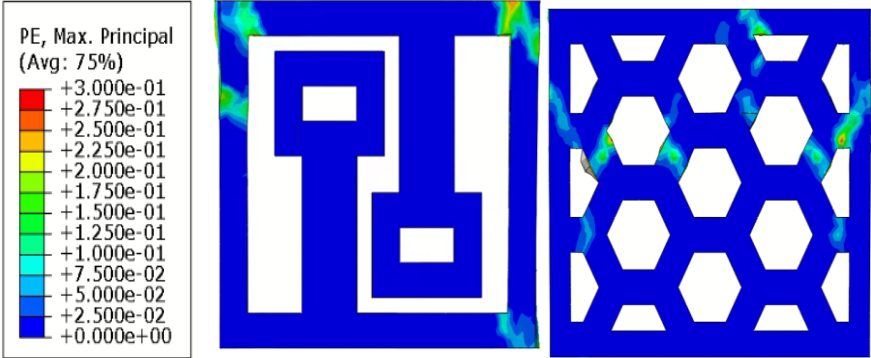
G1X	124	Y	165.14 z	0
G1X	136	Y	185.92 z	0
G1X	160	Y	185.92 z	0
G1X	172	Y	165.14 z	0
G1X	196	Y	165.14 z	0
G1X	208	Y	185.92 z	0
G1X	232	Y	185.92 z	0
G1X	244	Y	165.14 z	0
G1X	268	Y	165.14 z	0
G1X	280	Y	185.92 z	0
G1X	280	Y	193.92 z	0
G1X	268	Y	214.71 z	0
G1X	244	Y	214.71 z	0
G1X	232	Y	193.92 z	0
G1X	208	Y	193.92 z	0
G1X	196	Y	214.71 z	0
G1X	172	Y	214.71 z	0
G1X	160	Y	193.92 z	0
G1X	136	Y	193.92 z	0
G1X	124	Y	214.71 z	0
G1X	100	Y	214.71 z	0
G1X	88	Y	193.92 z	0
G1X	68	Y	214.71 z	0
G1 X	68	Y	214.71 Z	4
G1X	88	Y	193.92 Z	4

Appendix D

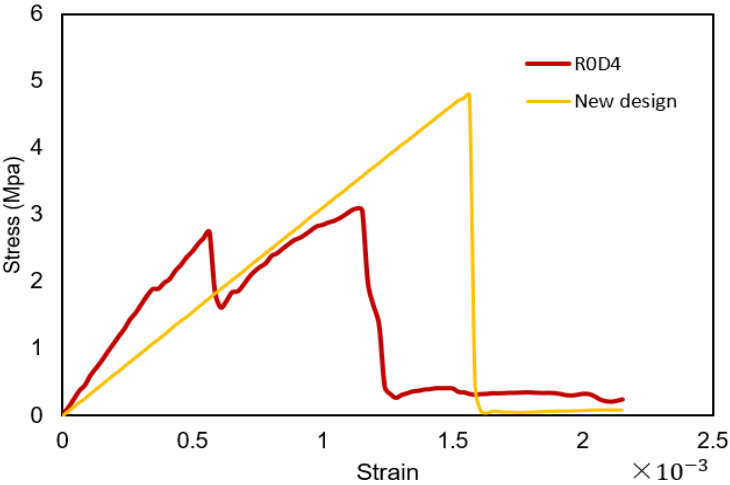
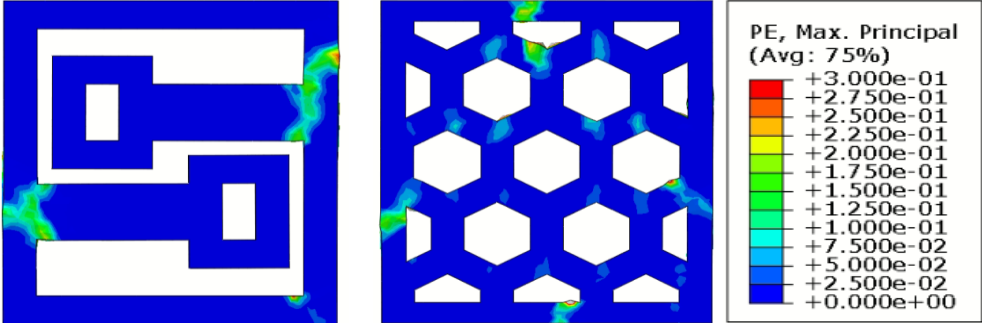
The comparison of mechanical strength between ROD4 with thermal bridge and the design eliminating the thermal bridge(new design)



On out of plane direction, the stiffness of ROD4 and the new design is same, the peak stress of ROD4 is slightly higher than that of new design



In the in-plane direction 1 , the stiffness of R0D4 is higher than new design, however the peak stress of new design is higher than that of R0D4



In the in-plane direction 2 , the stiffness of ROW4 is slightly higher than new design, however the peak stress of new design is higher than that of ROW4